NASA/TM—2000-209290

Cooperative Research Projects in the Microgravity Combustion Science Programs Sponsored by NASA and NEDO

Howard Ross, compiler
Glenn Research Center, Cleveland, Ohio

January 2000

The NASA STI Program Office . . . in Profile

Since its founding, NASA has been dedicated to the advancement of aeronautics and space science. The NASA Scientific and Technical Information (STI) Program Office plays a key part in helping NASA maintain this important role.

The NASA STI Program Office is operated by Langley Research Center, the Lead Center for NASA's scientific and technical information. The NASA STI Program Office provides access to the NASA STI Database, the largest collection of aeronautical and space science STI in the world. The Program Office is also NASA's institutional mechanism for disseminating the results of its research and development activities. These results are published by NASA in the NASA STI Report Series, which includes the following report types:

- TECHNICAL PUBLICATION. Reports of completed research or a major significant phase of research that present the results of NASA programs and include extensive data or theoretical analysis. Includes compilations of significant scientific and technical data and information deemed to be of continuing reference value. NASA's counterpart of peer-reviewed formal professional papers but has less stringent limitations on manuscript length and extent of graphic presentations.
- TECHNICAL MEMORANDUM. Scientific and technical findings that are preliminary or of specialized interest, e.g., quick release reports, working papers, and bibliographies that contain minimal annotation. Does not contain extensive analysis.
- CONTRACTOR REPORT. Scientific and technical findings by NASA-sponsored contractors and grantees.
- CONFERENCE PUBLICATION. Collected papers from scientific and technical conferences, symposia, seminars, or other meetings sponsored or cosponsored by NASA.
- SPECIAL PUBLICATION. Scientific, technical, or historical information from NASA programs, projects, and missions, often concerned with subjects having substantial public interest.
- TECHNICAL TRANSLATION. English-language translations of foreign scientific and technical material pertinent to NASA's mission.

Specialized services that complement the STI Program Office's diverse offerings include creating custom thesauri, building customized data bases, organizing and publishing research results . . . even providing videos.

For more information about the NASA STI Program Office, see the following:

- Access the NASA STI Program Home Page at *http://www.sti.nasa.gov*
- E-mail your question via the Internet to help@sti.nasa.gov
- Fax your question to the NASA Access Help Desk at (301) 621-0134
- Telephone the NASA Access Help Desk at (301) 621-0390
- Write to:
  NASA Access Help Desk
  NASA Center for AeroSpace Information
  7121 Standard Drive
  Hanover, MD 21076

NASA/TM—2000-209290

Cooperative Research Projects in the Microgravity Combustion Science Programs Sponsored by NASA and NEDO

Howard Ross, compiler
Glenn Research Center, Cleveland, Ohio

National Aeronautics and
Space Administration

Glenn Research Center

January 2000

Available from

NASA Center for Aerospace Information
7121 Standard Drive
Hanover, MD 21076
Price Code: A10

National Technical Information Service
5285 Port Royal Road
Springfield, VA 22100
Price Code: A10

Combustion of Interacting Droplet Arrays in a Microgravity Environment

Masiki Ikegami, Senji Honma, Kouji Ikeda,
Shouhei Takeda, Hiroshi Nagaishi

Hokkaido National Industrial Research Institute
(HNIRI Japan)

Daniel L. Dietrich and Peter M. Struk

NASA Lewis Research Center
(LeRC of NASA, U.S.A)

National Center for Microgravity Research

1 Interacting Droplet Combustion under Conditions of Extinction

1.1 Introduction

Investigations into droplet interactions date back to Rex et al.[1]. Recently, Annamalai and Ryan[2] and Annamalai[3] published extensive reviews of droplet array and cloud combustion studies. The goal of the studies the authors reviewed is to determine the change in the burning rate constant, k, (relative to that of the single droplet) that results from interactions. This change occurs as a result of two competing mechanisms. The burning droplets compete for the available oxidizer, but there is also a reduction in the heat loss from the flame. Under certain conditions, there exists a separation distance where the droplet lifetime reaches a minimum, or average burning rate constant is a maximum[1,4-8]. Additionally, since inter-droplet separation distance, L, increases relative to the droplet size, D, as the burning proceeds, the burning rate is not constant throughout the burn, but changes continuously with[7-10]. All of the aforementioned experimental results were in normal gravity environments, and except for the results of Law and co-workers, the buoyant flow strongly influenced the results. Theoretical treatments of the problem, however, typically neglect buoyancy[9-14].

In their studies, Law and co-workers reduced buoyant forces by reducing the system pressure. The oxidizer concentration in the ambient had to be high (> 40%), however, to avoid extinction or ignition limits due to the reduced pressure. They studied binary[8] and linear[7] arrays of droplets. They determined that the change in k could be interpreted on the basis of flame size and oxygen competition between the droplets. Comparing their results with existing theory, the theory over predicted the persistency and intensity of droplet interactions. The droplet interactions also depended on the initial array configuration as well as the instantaneous array configuration. They also concluded that droplet heating was retarded due to interactions and that the burning process did not follow the "D-squared" law. More recently, Mikami et al.[15] studied the combustion of a two-droplet array of heptane burning in air at one atm. pressure in microgravity. They showed that the instantaneous burning rate constant increases throughout the droplet lifetime, even for a single droplet. Also, the burn time of the array reached a minimum at a critical inter-droplet spacing. They assert that this is due to competing effects of radiative enhanced heating of the droplets and competition for the available oxygen.

Close examination of the experimental results shows that although the instantaneous k can be considerably different, the droplet lifetime, or burning rate constant averaged over the droplet lifetime is not significantly affected by interactions. The reason is that interactions primarily affect the burning during the droplet heat-up period and not during most of the combustion history. This is in contrast with the analytical studies that show significant changes to the burning rate constant due to interactions. Also, the experimental results show that interactions are quite weak at $L/D \geq 7$.

In this article, we examine droplet interactions under conditions that yield finite extinction diameters, and determine how droplet interactions affect the extinction process. Droplet burning was in normal and micro-gravity environments, and reduced pressure, air and sub-atmospheric oxygen ambients.

1.2 Experimental Hardware and Data Analysis

The experiments utilized the classical fiber-supported droplet combustion technique. A 125 or 230 μm (depending on the initial droplet size) fiber with a small bead (approximately 2 times the fiber diameter) supported the droplets. The fuel was n-decane for all of the tests. A small coiled hot-wire, withdrawn immediately after ignition, ignited the droplets. The microgravity experiments were in the NASA Lewis Research Center (LeRC) 2.2 second drop tower and the Japan Microgravity Center (JAMIC) 10-second drop tower. The typical droplet size for the normal gravity experiments was D_o = 1.2 mm ± 0.1 mm. The typical droplet size for the LeRC microgravity experiments was D_o = 1.0 mm ± 0.1 mm and for the JAMIC experiments was D_o = 1.7 mm ± 0.1 mm. For the microgravity experiment, a computer control system placed the fuel droplet on the fiber in normal gravity a short time before entry into microgravity. The computer initiated ignition of the droplet immediately after the experiment entered microgravity. The ambient environment was reduced pressure air for the normal gravity experiments, and reduced pressure, reduced oxygen ambients for the microgravity tests. Nitrogen was the diluent for all testing.

The data for both the normal and micro-gravity experiments was from two orthogonally located video cameras. The first camera provided a magnified, backlit view of the droplet to obtain the droplet regression history. The second was an orthogonal view of the flame. Some experiments utilized a small 15 μm diameter SiC fiber to visualize the flame, primarily in ambient conditions when the flame was invisible to the CCD camera. A microcomputer equipped with a black and white frame-grabbing board analyzed the video data from the experiments. The droplet diameter reported herein is an equivalent size obtained by equating the measured volume or the projected area of the droplet to that of the equivalent sphere or circle, respectively. A more detailed explanation of the data analysis is available in Struk et al.[16]. For the data herein, we report both an average and an instantaneous k. The average k comes from a linear fit of the data between $t = 0.1^*t_b$ and 0.9^*t_b, where t_b is the total burn time. We use this in cases where the deviation from linear behavior is small. The instantaneous k comes from a modified cubic spline fit to the experimental data. In this method, the data is divided into discrete intervals ($\Delta[t/D_o^2]$). A best-fit third order polynomial is found for each interval subject to the constraint that at each node point, there is continuity in $(D/D_o)^2$, the first derivative (k), and the second derivative. We found that this provides an excellent fit to the experimental data, and yields accurate values of the instantaneous burning rate constant.

1.3 Experimental Results

Figure 1 shows the average burning rate constant as a function of separation distance normalized by the initial diameter, L/D_o, for three different pressures. This figure clearly shows that the average burning rate constant is not significantly affected by interactions. This, at first review, may seem in conflict with existing studies. We note that, however, in the work of Mikami et al. (1996), even though the instantaneous burning rate for an array may differ from the single droplet burning rate by as much as 70%, the droplet lifetime, or average burning rate constant varies less than 10% for L/D_o greater than or equal to 6. The greatest change occurs early in the droplet lifetime, during the droplet heating period. After this period is over, interaction effects are small. This initial period is not represented in Figure 1. Thus, these results are not all that inconsistent with existing studies.

At pressures below 90 torrs in normal gravity, the flame surrounding the droplet(s) extinguished at a finite droplet diameter. Figure 2 shows the extinction droplet diameter as a function of pressure for single droplets and two droplet arrays at two different inter-droplet spacings. The single droplet results compare favorably with the work of Chung and Law[17], with the extinction droplet diameter increasing with decreasing pressure. At pressures below 54 torr, ignition was extremely difficult, if not impossible. More importantly, Figure 2 shows that interaction effects have a significant influence on the extinction droplet diameter. At an inter-droplet spacing of 12 mm and low pressures the extinction droplet size is approximately 60% that of a single droplet. And while these experimental results and previous work shows small influences on the burning rate constant at L/D greater than 10, these results show that interaction effects at extinction are still strong at L/D ~ 20. Figure 2 shows that at L = 24 mm, the two-droplet array data is indistinguishable from the single droplet data.

There are three other important points that are not represented in Figure 2. First, at inter-droplet spacings below 12 mm (8 mm was the next smallest size), the flame did not extinguish at a finite droplet diameter. Or, more specifically, the extinction droplet diameter was smaller than the supporting fiber and bead and thus was not measurable. Second, the interaction effect on flame extinction was present whether there was an envelope flame surrounding both droplets or individual flames around each droplet. Finally, the array results in Figure 2 are for identically sized droplets. There were a large number of tests (not shown here) where there was a significant difference in the initial droplet size, at pressures that yielded finite extinction droplet diameters. In these cases, the flame around the larger droplet extinguished immediately (within 0.033 second or 1 video frame) after the smaller droplet disappeared. This again occurred for cases where a single envelope flame surrounded both droplets and where individual flames surrounded each droplet.

Qualitatively, the results of the microgravity testing were very similar to the normal gravity tests described above. The tests in microgravity were in a reduced oxygen ambient. While the use of reduced pressure reduces the effect of buoyancy, it does not altogether eliminate it. Easton[18] showed that the reduced pressure conditions that yield a finite extinction droplet diameter in normal gravity do not produce a finite extinction droplet diameter in microgravity. This shows that there is still a small sub-buoyant flow present in reduced pressure, normal gravity. And although the flames are nearly spherical and concentric, this buoyant flow effects the region outside the flame where the Stefan flow is weak. This in turn significantly effects the extinction process.

The first series of microgravity tests were of two binary-droplet arrays and a single droplet in a 0.17 oxygen mole fraction, 380 torr ambient in the JAMIC facility. Figure 3 shows the results for a single droplet and two, two-droplet arrays. The behavior was as expected, with burn time and instantaneous k increasing slightly with decreasing separation distance. There were, however, several noteworthy features. First, the burning behavior was very non-linear, much more so than that observed for higher oxygen concentrations. Second, the droplets burned to completion, whereas in normal gravity (at the same conditions), the droplets would not have ignited.

Figure 4 shows similar tests except that this time the oxygen mole fraction is 0.15. In this case the single droplet flame extinguished at a finite droplet diameter. This is evident from the instantaneous burning rate constant also shown in Figure 4. For the droplet arrays, however, the flames did not extinguish, or at least the extinction droplet diameter was smaller than the fiber diameter (0.23 mm in this case).

1.4 Discussion

The effect of interactions during droplet burning occurs as a result of two competing mechanisms. The droplets compete for oxidizer, and this effect tends to weaken the burning of each individual droplet. The heat loss between the droplets is reduced, however, and this tends to strengthen the flame. At large separation distances, neither effect is significant, and there is no interaction effect. The results in this work show that for burning in the diffusion dominated regime (negligible chemical kinetic effects), the net effect of these two competing mechanisms averaged over the lifetime of the droplet is quite small. Thus, the average burning rate constant varies only slightly with inter-droplet separation distance.

Near extinction, however, the effects of interaction are significant. In this case, the diffusive and chemical kinetic time-scales are comparable. Extinction occurs when the characteristic residence time is smaller than the characteristic chemical reaction time. The residence time is not significantly affected by interactions since both the burning rate constant and flame standoff ratio (for individual flames) are nearly the same. Thus, interactions primarily affect the characteristic chemical reaction time. Diminished oxygen transport to the flame tends to weaken the flame, but the reduced heat loss tends to strengthen the flame. The characteristic chemical time is exponentially dependent on temperature, and linearly dependent on the local oxygen concentration (assuming first order dependence in oxidizer concentration). The reduced heat loss thus dominates near extinction.

2 Combustion of Interacting Droplet Arrays in a Microgravity Environment

2.1 Introduction

The objective of this research is to determine the effect that droplet interactions have on the burning behavior of droplets. The work extends work involving single droplets to the regime where droplet interactions are important. In this way, some of the physics relevant to practical combustion devices are incorporated into a problem amenable to numerical and theoretical studies.

2.2 Present Studies

The previous studies at JAMIC (November 1997) showed unusual behavior of a decane droplet at extinction (reported in Struk et al., Joint Technical Meeting of the Combustion Institute, 1999). A single droplet burning in a 15% oxygen (mole fraction), 1/2 atm ambient showed extinction at a finite droplet diameter. In contrast, a two droplet array at the same ambient conditions did not exhibit extinction. This behavior had not been observed in previous studies of droplet array combustion. These results were confirmed in normal gravity tests at low pressure at the NASA Glenn (Lewis) Research Center.

The goal of this series of drops at the Japan Microgravity Center (JAMIC) was to investigate single droplet and binary droplet array combustion of both pure fuels and practical fuels under conditions where the flame extinguishes at a finite droplet diameter. This is to both confirm the previous studies with additional data and acquire new data on a practical fuel, namely diesel fuel.

2.3 Justification for use of JAMIC.

This project has required the use of the 2.2 and 5.2 second drop towers at the NASA Glenn Research Center and also the JAMIC facility. It is possible to get good information regarding the burning rate of single droplets and droplet arrays in shorter duration microgravity facilities. It is more difficult to observe extinction, however, because of the test time required. We therefore use the JAMIC facility to study single droplet combustion and droplet array combustion under conditions of extinction.

2.4 Experimental Apparatus

The tests used the existing experimental apparatus. This is the same apparatus as was used for the last series of experiments, with the exception that some of the electronics were re-designed to optimize performance. This is also the same apparatus used in both the NASA Glenn Research Center 2.2 and 5.2 second drop tower.

Figure 5 shows the entire drop apparatus, which consists of the pressure chamber (capable of 0-2 atm pressure), batteries, electronic control system and the video cameras. Figure 6 shows a close up view of the pressure chamber. The insert to the combustion chamber is shown in Figures 7 and 8, along with a schematic in Figure 9. The insert to the combustion chamber consists of the support fiber, Si-C fiber (present, but not visible due to it's small size), hot-wire igniter, deployment needles, fuel syringe and pump, and the backlight (3 LEDs).

230 micrometer optical fibers with a small bead on the end support the droplets which typically had 1.5 mm initial diameters (estimated). The droplets are dispensed on the fiber in normal gravity approximately 2 minutes before the drop. The ignition source is a hot-wire heated activated

immediately after entry into microgravity. The wire rapidly withdraws from the droplet at a preset time, usually with 100 msec of ignition.

The datais from two orthogonally located video cameras. One view is backlit by a bank of red LEDs, to provide the droplet size as a function of time. The other camera is a direct image of the flame. In many of the tests, the flame is quite dim and nearly invisible to the CCD camera. As such a small 15 micron Si-C fiber is placed through the droplet normal to the support fiber. The glow from the fiber provides an excellent marker of the flame position and also clearly indicates when extinction occurs.

2.4 Test Conditions

The test conditions were selected based on testing at JAMIC in November 1997 and more recent normal gravity and microgravity tests at the NASA Glenn Research Center. The goal was to observe flame extinction at a finite droplet size during the available test time. This is difficult to observe in test times less than approximately 5 sec, making JAMIC ideal for these tests.

The initial droplet size was typically about 1.5 mm, the exact size to be determined by detailed analysis of the video tapes. The ambient oxygen concentration was 0.145 to 0.15 mole fraction for all of the tests. The ambient pressure was 0.25 atm for all of the tests. The fuels were n-decane, for which we have extensive experience, 1-methylnapthalene and mixtures of the two fuels, and a reference diesel fuel (Chevron).

2.5 Data Analysis

The primary data is from the backlit view of the droplet. The CCD camera records the droplet size as a function of time. The video data is digitized and transferred to an Apple Macintosh microcomputer with a black and white frame grabber card installed. A simplified schematic of the digitized droplet is shown in Figure 10. The droplet is not spherical, as the support fiber distorts the shape. We report an equivalent droplet size as the size of a sphere with the same projected (1) area or (2) volume as that measured with the computer. The details of the computation and the relevant equations are also shown in Figure 10. The details of the analysis method and the rationale for the use of the two diameters is reported in Struk et al. (1999).

The droplet size data is supplemented by data from the flame view camera. This view records the flame as a function of time. The primary data is the size of the flame, shape of the flame (single droplets are spherical, and the array can have either a merged or seperate flame), and intensity of the flame. In many instances, the flame was dim enough such that size measurements are either difficult or impossible. In these cases, the flame size comes from the Si-C fiber. Figure 11 shows the intensity profile from the Si-C fiber for a single decane droplet in a 0.15 oxygen mole fraction (balance nitrogen), 0.5 atm ambient. This test was in the NASA Glenn Research Center 5.2 second drop tower. The profile clearly shows two peaks, the distance between which is the flame diameter and one peak, droplet itself. We note that the intensity profile from these fibers has been used to measure the flame temperature during droplet combustion. This work was done as part of this joint effort.

The glow from the fibers can also be used to determine when extinction occurs. Figure 12 shows the peak intensity as a function of time for a droplet whose flame extinguished at a finite droplet diameter. The occurence of extinction is clearly visible from this figure.

2.6 Experimental Results

The testing reported herein was completed on 25 February 1999. As such, the results below are preliminary, and the conclusions should be viewed as such. Each test will be described seperately along with a brief qualitative description of the results.

Test #1: P = 1/3 atm, YO2 = 0.15, single droplet, diesel fuel. Succesful igniton and burning to completion. The flame was bright after ignition and became dim blue by the end of the tes.

Test #2: P = 1/4 atm, YO2 = 0.15, single droplet, diesel fuel. Succesful igniton and burning to extinction. The flame was dim blue throughout the test.

Test #3: P = 1/4 atm, YO2 = 0.145, single droplet, diesel fuel. Succesful igniton and burning to extinction with a larger extinction diameter than #02. The flame was dim blue throughout the test.

Test #4: P = 1/4 atm, YO2 = 0.145, two-droplet array, l = 4 mm, diesel fuel. Successful ignition and burning to extinction. Extinction droplet size seems to be larger than expected. Dim blue flame throughout the drop.

Test #5: P = 1/4 atm, YO2 = 0.15, two-droplet array, l = 4 mm, diesel fuel. Successful ignition and burning to extinction. Extinction occurred early in lifetime and at a larger size than expected. Dim blue flame throughout the drop. View starts to for up after extinction.

Test #6: P = 1/4 atm, YO2 = 0.15, two-droplet array, l = 4 mm, diesel fuel. Successful ignition and burning to extinction. Extinction occurred early in lifetime and at a larger size than expected. Dim blue flame throughout the drop. View starts to for up after extinction.

Test #7: P = 1/4 atm, YO2 = 0.15, single, n-decane fuel. Successful ignition and burning to completion. Dim blue flame throughout the drop. Flame increases in size and then begins to shrink.

Test #8: P = 1/4 atm, YO2 = 0.15, single, n-decane fuel. Successful ignition and burning to completion. Dim blue flame throughout the drop. Flame decreases continuously with time. Droplet smaller than desired due to a bubble in the fuel line.

The tests with diesel fuel showed extinction at both oxygen concentrations. Suprisingly, the array extinguished at a similar or larger diameter than the single droplet. This is in contrast with the work at JAMIC on the last series of tests and testing in normal gravity. We must completely analyze the data before drawing definitive conclusions.

Test #9: P = 1/4 atm, YO2 = 0.15, two-droplet array, l = 4 mm, Decane fuel. Same size of two-droplets. Successful ignition and burning to extinction. One flame around two-droplets. Flame increases in size during burning.

Test #10: P = 1/4 atm, YO2 = 0.15, two-droplet array, l = 4 mm, Decane fuel. Same size of two-droplets (1.2mm diameter). Successful ignition and burning to extinction. One flame around two-droplets. No fuel remains at extinction.

Test #11: P = 1/4 atm, YO2 = 0.145, two-droplet array, l = 4 mm, Decane fuel. Size of left drop-let is 0.8mm diameter and right drop-let is 1.5mm diameter. Successful ignition and burning to extinction. One flame around two-droplets is observed. This flame seems to be same condition as the two same size drop-lets.

Test #12: P = 1/4 atm, YO2 = 0.145, single droplet, Decane fuel. Size of drop-let is 1.5mm diameter. Successful ignition and burning to extinction. No fuel remains at extinction.

Test #13: P = 1/2 atm, YO2 = 0.151, single droplet, Decane fuel. Size of drop-let is 1.5mm diameter. Successful ignition and burning to extinction. No fuel remains at extinction.

Test #14: P = 1/2 atm, YO2 = 0.15, single droplet, Decane fuel. Size of drop-let is 1.5mm diameter. Successful ignition and burning to extinction. Flame increase in size continuously (Figure 16). The flame was dim blue throughout the test.

Test #15: P = 1/4 atm, YO2 = 0.21, Single Porous ball burner. Burner size is 3mm diameter. Fuel is supplied to burner continuously. The boiling fuel around the burner is observed. The size of flame has oscillation (Figure 17).

Test #16: P = 1/4 atm, YO2 = 0.18, Single Porous ball burner. Burner size is 3mm diameter. Fuel is supplied at the beginning of drop. Successful ignition and burning to completion. The boiling fuel around the burner is observed. The size of flame has oscillation.

References

1. Rex, J.F., Fuhs, A.E. and Penner, S.S. Jet Propulsion 26, 179 (1956).
2. Annamalai, K. and Ryan, W. Progress in Energy and Combustion Science 18, 221-295 (1992).

3. Annamalai, K. Mechanics and Combustion of Droplets and Sprays , ed. H.H. Chiu and N. Chigier, Begell House Inc., New York, New York, 116-160 (1995).
4. Sangiovanni, J.J. and A.S. Kesten Sixteenth Symposium (International) on Combustion / The Combustion Institute, 577-592 (1976).
5. Fedoseeva, N.V. Advances in Aerosol Physics 2, 110-117 (1972).
6. Fedoseeva, N.V. Advances in Aerosol Physics 3, 27-38 (1973).
7. Miyasaka, K. and C.K. Law Eighteenth Symposium (International) on Combustion / The Combustion Institute, 283-292 (1981).
8. Xiong, T.Y., C.K. Law, C.K. and K. Miyasaka Twentieth Symposium (International) on Combustion / The Combustion Institute, 1781-1787 (1984).
9. Labowsky, M. Combustion Science and Technology 18, 145-151 (1978).
10. Labowsky, M. Combustion Science and Technology 22, 217-226 (1980).
11. Brzustowski, T.A., E.M. Twardus, S. Wojcicki and A. Sobiesiak AIAA Journal 17, No. 11, 1234-1242 (1979).
12. Marberry, M., A.K. Ray and K. Leung Combustion and Flame 57, 237-245 (1984).
13. Samson, R., D. Bedeaux and J.M. Deutch Combustion and Flame 31, 223-229 (1978).
14. Umemura, A., S. Ogawa and O. Nobunori Combustion and Flame 41, 45-55 (1981).
15. Mikami, M., Kato, H., Kono, M. and Sato, J. Twenty-Fifth Symposium (International) on Combustion / The Combustion Institute, 423-428 (1995).
16. Struk, P., Ackerman, M., Nayagam, V. and Dietrich, D. (1998) "Fiber Effects in Droplet Combustion," in preparation.
17. Chung, S. and Law, C.K. Combustion and Flame 64, 237-241 (1986).
18. Easton, J. (1978) Masters Thesis, Case Western Reserve University.

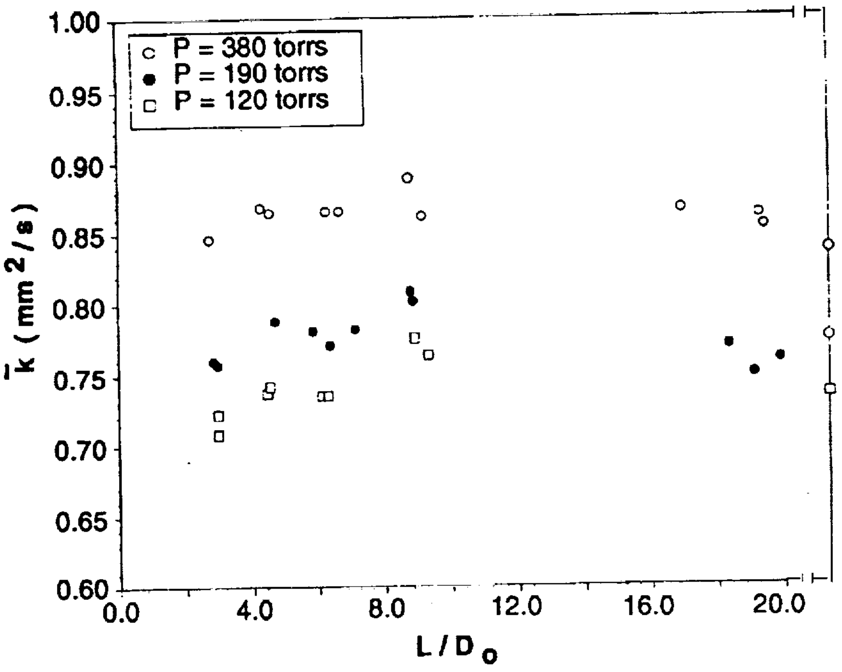

Figure 1. Average burning rate constant as a function of normalized separation distance for three different pressures in normal gravity.

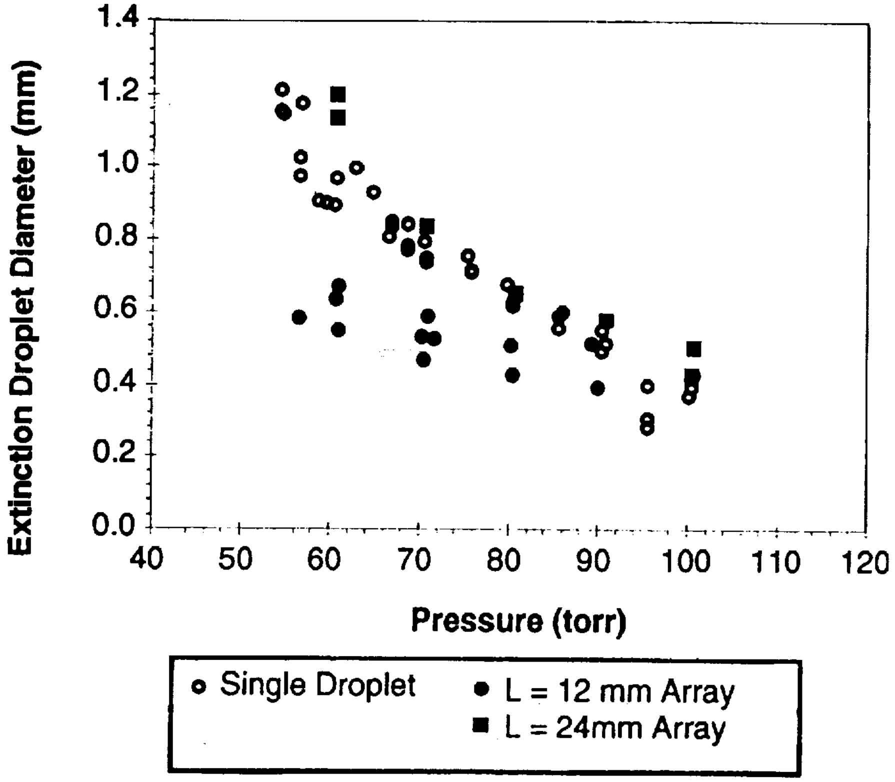

Figure 2. Extinction droplet diameter as a function of pressure for single droplets and two droplet arrays at two different inner-droplet spacings in normal gravity.e

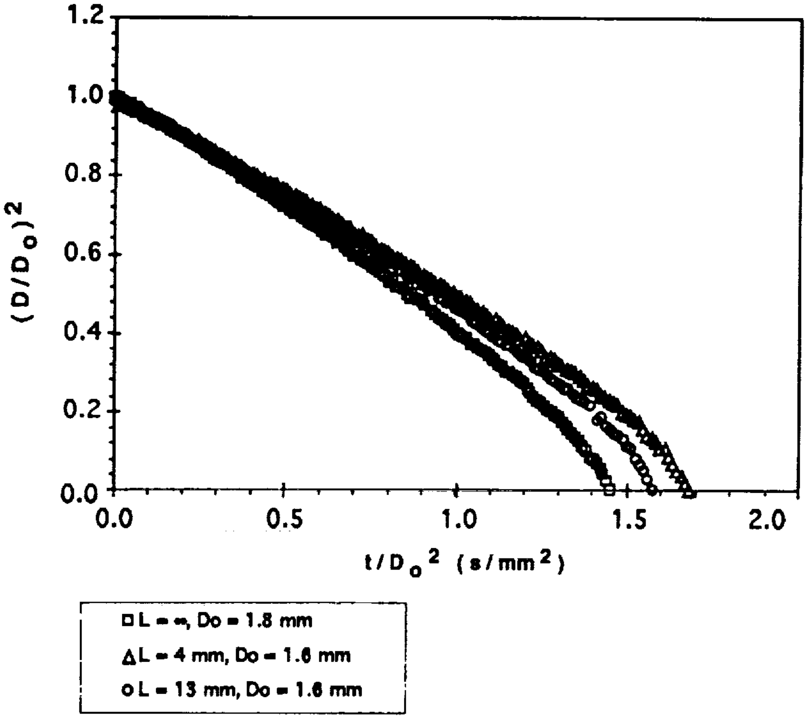

Figure 3. Droplet history for a two droplet array in a 51kPa, 0.17 oxygen mole fraction ambient in microgravity. The fuel was n-decane.

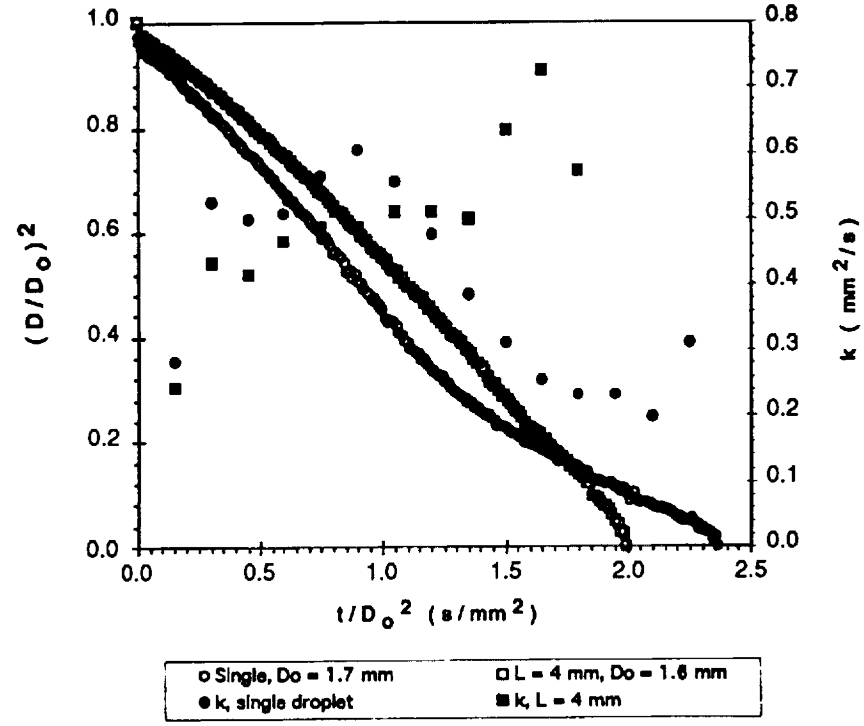

Figure 4. Droplet and burning rate history for a two droplet array in a 51kPa, 0.15 oxygen mole fraction ambient in microgravity. The fuel was n-deacon.

Figure 5　Apparatus for JAMIC

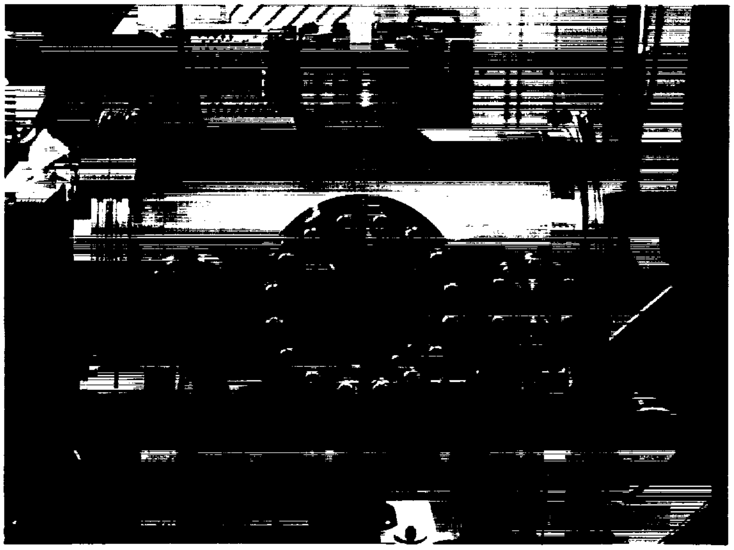

Figure 6　Chamber

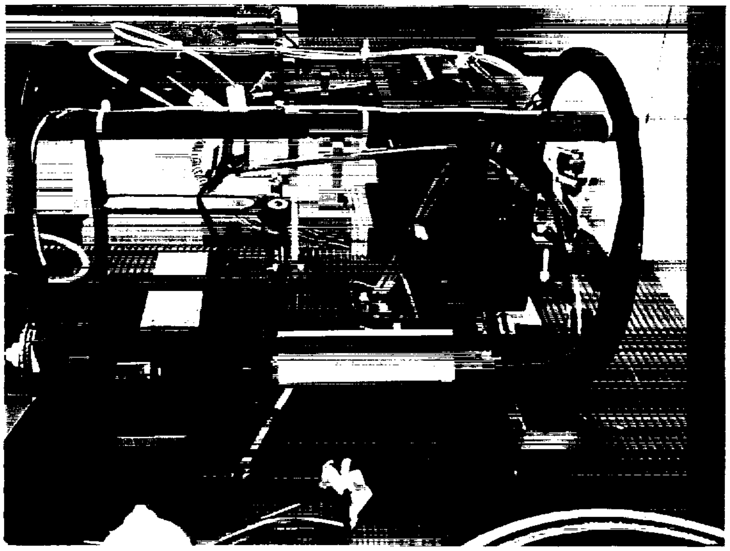

Figure 7 The Droplet arrays combustion apparatus.

Figure 8 Droplet holder and needle

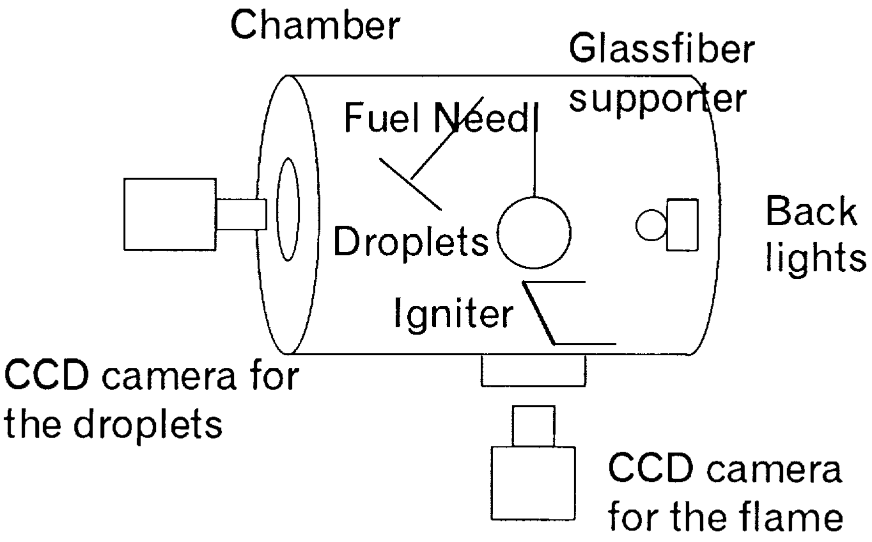

Figure 9 The Droplet arrays combustion apparatus

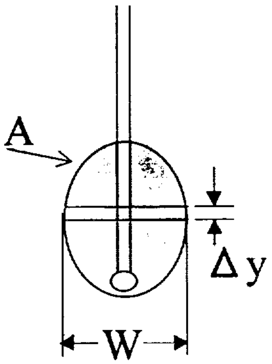

$$D = \left(\frac{4}{\pi} A\right)^{1/2} \quad (1)$$

$$D = \left(\frac{4}{\pi} V\right)^{1/3} \quad (2)$$

$$V = \sum \Delta y \left(\frac{\pi}{4} W^{2}\right)$$

Figure 10 Equivalenet Diameter of the Droplet

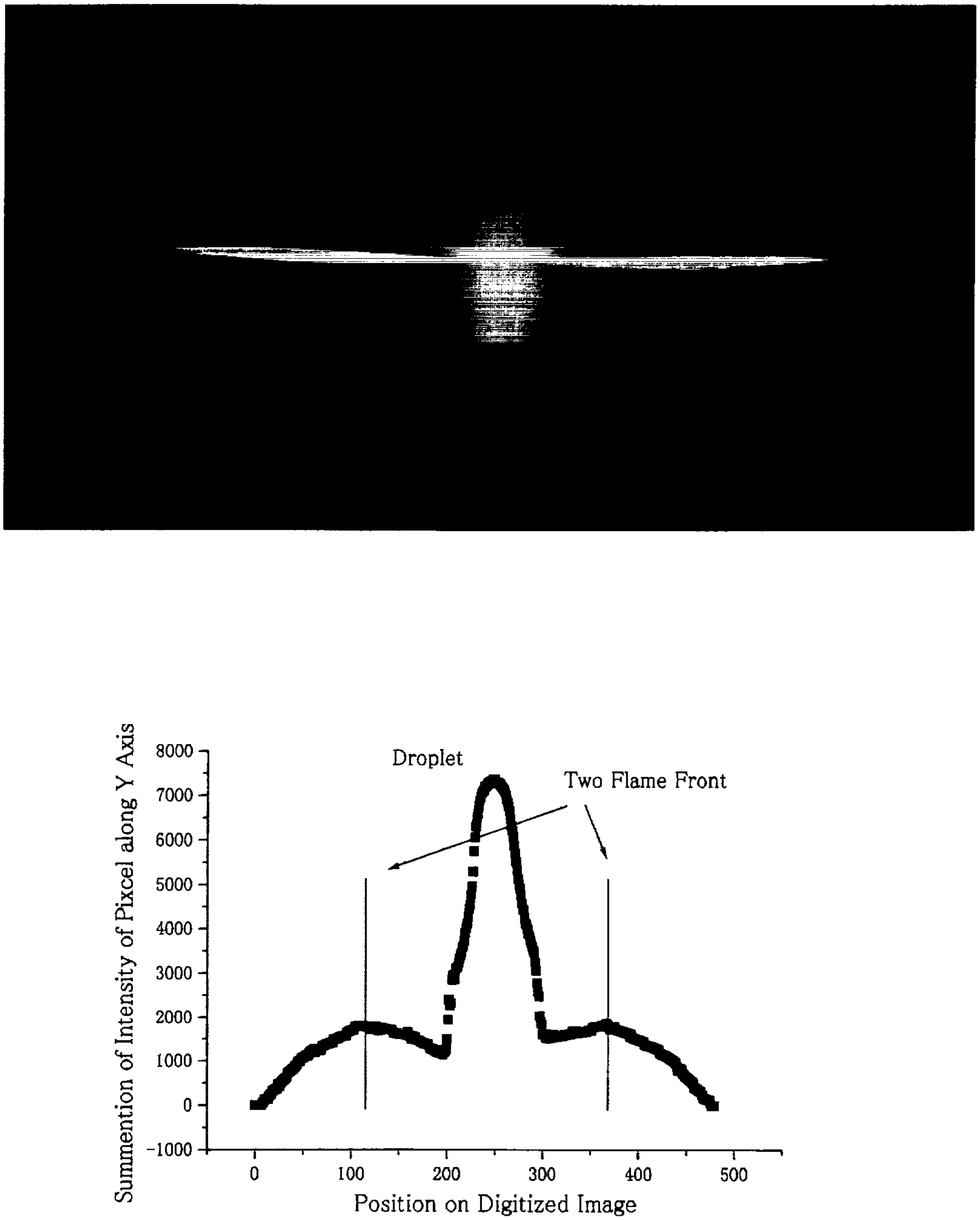

Figure11 Intensity Profile of SiC Fiber

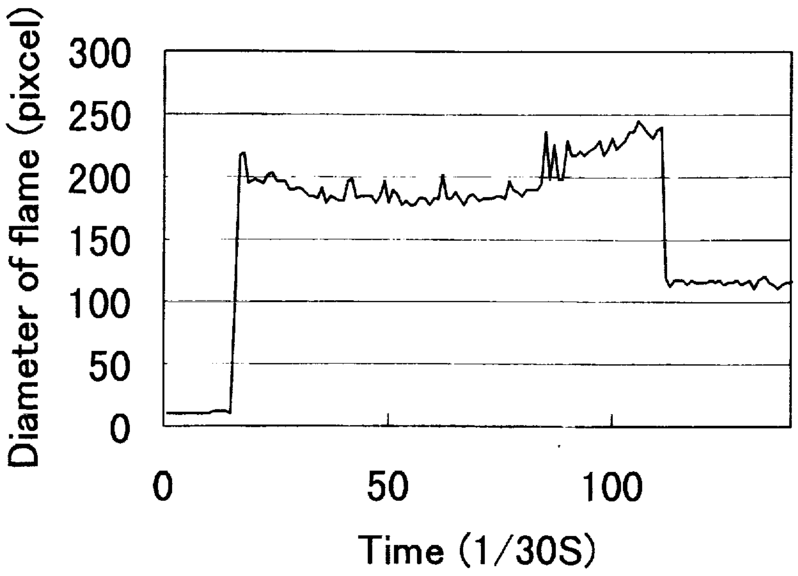

Figure 12 Diameter of Flame (shrink and expansin)

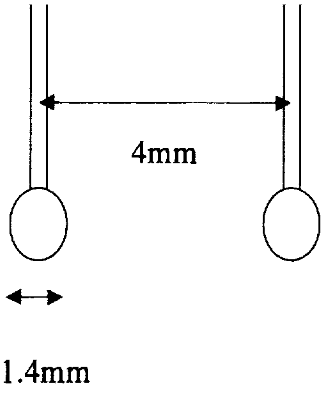

Figure 13 Configuration of the Fiber and Droplets

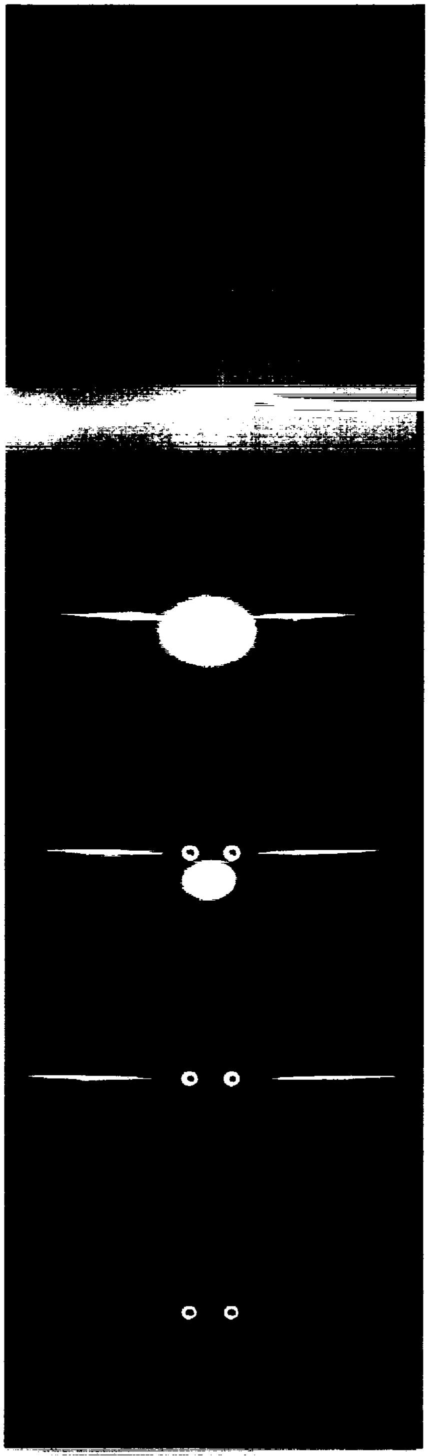

Figure 14 Flame View from Ignition to Extinction

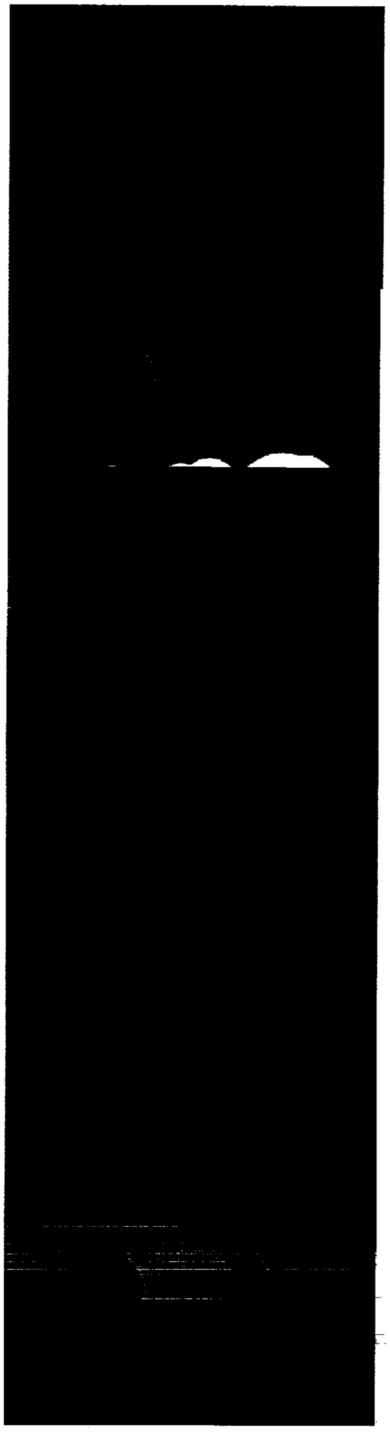

Figure 15 Droplet View from Ignition to Extinction

Size of Flame

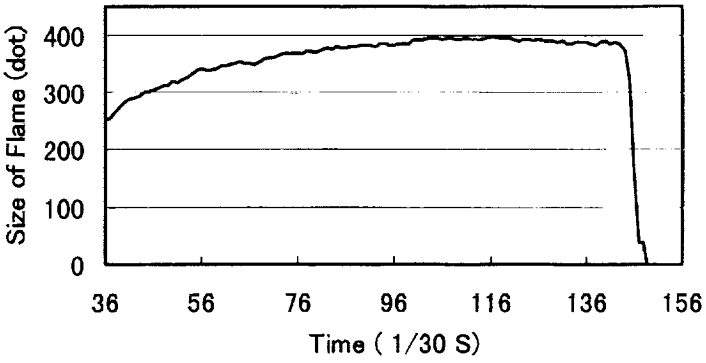

Figure 16 Diameter of Flame (expansion and extinction)

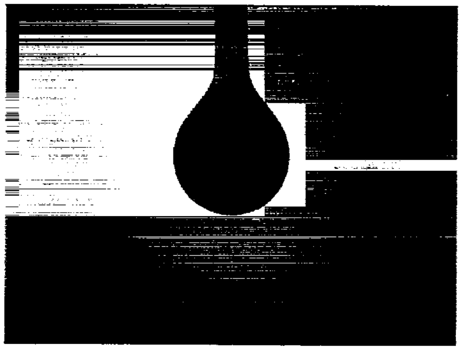

(a) Porous ball burner.

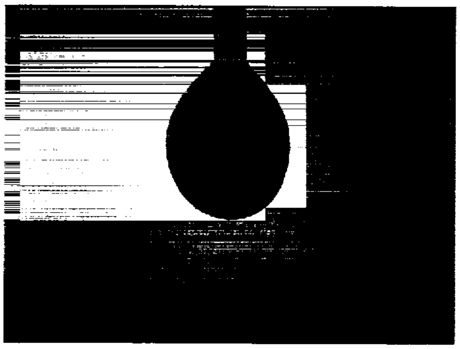

(b) Porous ball burner covered with fuel.

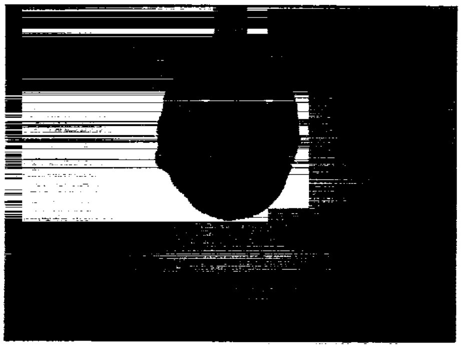

(c) Boiling fuel.

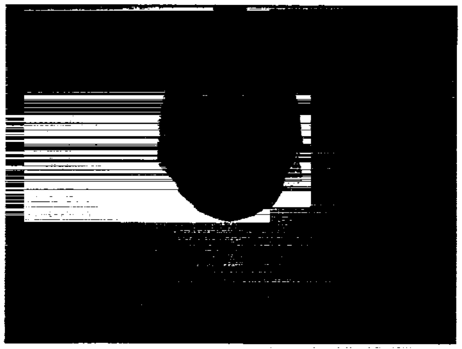

(d) Boiling fuel.

Figure 17 Pictures of porous ball burner.

High-Pressure Combustion of Binary Fuel Sprays

Michikata KONO(*The University of Tokyo*)

Jun'ichi SATO(*Ishikawajima-Hirima Heavy Industries*)

Forman A. WILLIAMS(*University of California San Diego*)

ABSTRACT

The interactive combustion of two miscible binary-fuel droplets at elevated pressures, up to the values above the critical pressure of the fuel, was investigated experimentally. Heptane and hexadecane were selected as the fuel mixture, to study the occurrence of staged combustion, and a nitrogen-oxygen atmosphere with a relatively low oxygen concentration was employed to facilitate observation of droplets during combustion at elevated pressures. The effects of fuel composition, ambient pressure and droplet spacing were investigated. Results show that staged combustion of binary fuel droplets still exists for interacting droplets at high pressure and that burning-rate constants of the first and the third stages, as well as the transition droplet volume are not strongly affected by interaction. The increase in droplet lifetime by strong interaction is demonstrated and explained. It is shown that the lifetime achieves a minimum value at a critical droplet spacing even for binary fuel droplets that undergo staged combustion at high pressure without buoyancy, a result which is explained by influences of radiant energy transfer. It is also demonstrated experimentally that flame lifetimes exceed droplet lifetimes at high pressure both for single droplets and strongly interacting droplet pairs, which is explained by vapor presence after liquid disappearance and reduced tendencies towards flame extinction at elevated pressures.

High-Pressure Combustion of Binary Fuel Sprays

Michikata KONO(*The University of Tokyo*)

Jun'ichi SATO(*Ishikawajima-Hirima Heavy Industries*)

Forman A. WILLIAMS(*University of California San Diego*)

1. INTRODUCTION

Understanding droplet vaporization and combustion processes in high-pressure combustors is of crucial importance in the study of spray combustion, since many practical spray-combustion systems (including diesel engines, gas-turbine engines and liquid rockets) often operate at or above the critical pressure of injected fuels. In such a high-pressure environment, any liquid fuel droplet injected at a temperature below its critical temperature may undergo both subcritical and supercritical processes before it burns completely.

Bicomponent and high-pressure isolated droplet combustion has been studied both experimentally[1-9] and theoretically[10-14]. Because of experimental difficulties, the results of these studies do not provide an entirely clear physical picture of high-pressure droplet combustion, and little information on high-pressure droplet combustion exists for multicomponent fuels[5-7,9], despite its practical importance.

Dense sprays of practical interest at high pressures exhibit the further complication of droplet interaction during combustion. Although there have been some experimental[15-22] and theoretical[17,23-25] studies of influence of droplet interactions at atmospheric pressure, except for some numerical work[26] almost no information exists on the combustion of arrays of interacting droplets at high pressure.

The present study examines the combustion of two close-spaced fuel droplets of binary liquid mixtures at high pressures ranging from subcritical to supercritical. The experiments, involving heptane-hexadecane mixtures in atmospheres of zero air and reduced oxygen content, are performed under microgravity. The microgravity environment minimizes the effects of buoyancy to better enable comparisons with theory and prevents the droplets from falling off the suspending fibers as the surface tension diminishes with increasing pressure[6]. The suspending fibers keep the droplet in the field of view of the camera and also allow the inter-droplet separation distance to be fixed and known for the entire test.

2. EXPERIMENTAL APPARATUS AND PROCEDURE

The combustion experiments were performed in microgravity in a droptower at the NASA John H. Glenn Research Center which provides 2.2 seconds of microgravity(less than 10^{-5} times normal gravity), as schematically shown in Fig. 1. The experimental apparatus consists of a combustion chamber, a fuel-supply system, a hot wire igniter, two CCD cameras, a lamp, a timer unit, a motor driver, etc.(Fig.2 and Fig. 3). Since it is very similar to an apparatus described previously[7,22], only essential differences will be mentioned here.

The ambient gas was a room-temperature nitrogen-oxygen mixture with an oxygen mole fraction of 0.21 and 0.12. The reduced oxygen concentration of 0.12 was employed to aid in visualizing the droplet from the backlit view at high pressure; intense light emission from combustion obscures the backlight at higher oxygen concentrations. Figure 4 shows the fuel supply system and the ignitor, schematically. Two almost identical droplets were dispensed at the end of two identical 0.125 mm quartz fibers (with small beads on the end) in normal gravity just prior to the start of the test. The droplets then were ignited by two hot wires at the same time shortly after release of the experimental package to microgravity. The igniter duration was fixed at 0.2 seconds after which the hot-wires were quickly retracted. Two orthogonal views of the combustion process were taken by two black and white CCD cameras through the windows of the chamber. One view is backlit to visualize the droplet, and the other view shows a direct photograph of the flame.

The images from the cameras were loaded onto a computer via a black and white frame grabber board for analysis. The droplet is elliptical and an equivalent diameter is computed as the diameter of the sphere that has the same projected area as that measured, as shown in Fig. 5. The initial diameter was 0.9mm (±0.1 mm), small enough such that the entire combustion history could be observed in the 2.2 second test time. The flame diameter of the droplet pair was taken as the maximum dimension of the visible flame, namely that along an axis through the center of the two droplets(Fig. 6).

3. RESULTS AND DISCUSSION OF ZERO AIR EXPERIMENTS

In the zero air tests, burning droplets could not be seen because of intense light emission from combustion. So only the burning lifetime was taken as data. Figure 7 shows sequential photographs of a coupling flame which surrounds two droplets(a ratio of separation distance, l, to initial droplet diameter, d_0, of $l/d_0=4$, $Y_0= 0.11$, $P=1\text{MPa}$). As shown in Fig. 7, one emerged flame surrounding two droplets persists for most of the lifetime in the strong interaction regime. In the current tests, emphasis is put on the strongly interacting regime, so the experimental conditions were selected as (1)$l/d_0 \doteqdot 2$, (2)$l/d_0 \doteqdot 4$ and (3)$l/d_0 = \infty$(single droplet).

Figure 8 shows the dependence of burning lifetime on pressure for pure heptane($Y_0=0$). It is seen that burning lifetime takes a minimum at near the fuel's critical pressure($P_{cr}=2.74$MPa) for single droplet. For droplet pairs, it is seen that burning lifetime exceeds that of single droplet for each pressure and spacing in the current strongly interacting regime($l/d_0 \leqq 5$). It is also seen that flame lifetime increases with decreasing spacing and the rate of increase in lifetime decreases with increasing pressure.

Figures 9(a)-(c) show the dependence of burning lifetime on pressure for fuel mixtures. The dependence of burning lifetime on pressure for $Y_0=0.11$ is shown in Fig. 9(a). It is seen in the figure that burning lifetime exceeds that of pure heptane both for single droplet and droplet pair.

Though burning lifetime of pure heptane takes a minimum on pressure each for single droplet and for droplet pair, as mentioned above, that of $Y_0=0.11$ looks decrease with pressure monotonously until about 5 MPa. As seen in Figs 9(b)-(c), burning lifetimes of $Y_0=0.33$ and $Y_0=0.63$ take minima on pressure of about 5 MPa both for single droplet and droplet pairs. But these minima are not so distinct as that of pure heptane. Thus it can be said that the dependence of burning lifetime on pressure for fuel mixtures is very different from that of pure fuels. It can be said that solution of inert gas on droplet surface in high pressure may affect these tendencies for fuel mixtures.

Also Fig. 8 and Figs 9(a)-(c) can compare burning lifetimes of droplet pair and single droplet. As seen in the figures, it is seen that interaction increase burning lifetime for each fuel composition(Y_0=0, 0.11, 0.33, 0.63). Though further discussion of effects of fuel composition on burning life time should be addressed with clarification of vaporization mechanisms(occurrence of staged combustion, temporal variation of burning rate constant) of burning droplets, burning droplets could not be seen in the current zero air test as mentioned above.

In the strongly interacting regime as the current test condition($l/d_0 \leqq 5$), one emerged flame surrounding two droplets persists for almost of the lifetime, so effects of radiative heat transfer on burning phenomena should be weak because the relative projected flame area to each droplet is small. Thus the interaction should be mainly caused by repression of droplet heating, which is introduced by decrease of temperature gradient from the extension of flame pursuing the lacking oxygen in the internal region. These results agrees to the results in atmospheric pressure by Miyasaka・Law and by Mikami *et al.*

A final important observation that can be made from Fig. 8 and Figs 9(a)-(c) is the dependence of interaction on pressure. For all Y_0s, the interaction effects, namely, the increase of burning lifetime decreases with increasing pressure. This magnitude of the decrease increases with the increase of Y_0. Thus it can be said that interaction effects are weaker as Y_0 becomes larger in the current test regime.

4. RESULTS AND DISCUSSION OF LOW OXYGEN EXPERIMENTS

In the last chapter, vaporization mechanisms could not be mentioned. Thus a series of tests on low oxygen atmosphere was performed. Here the results will be mentioned.

General Aspects and several definitions:

For the two-droplet tests, the shapes are classified roughly into two modes: individual flames surrounding each droplet and one merged flame surrounding the two droplets. In this study, emphasis is put on strongly interacting droplets, so the latter mode was studied. The selected separation for most of the two-droplet tests, a ratio of separation distance, l, to initial droplet diameter, d_0, of $l/d_0 = 1.7 \pm 0.1$, is in fact close to the limit($l/d_0 = 1$) in which the two droplets merge and behave as one. This selection was made in an effort to maximize the departure from single-droplet behavior, so that any droplet-interaction influences on high-pressure or binary-liquid single-droplet behavior would be revealed.

The selection of an oxygen mole fraction of 0.12 in these experiments facilitates comparison with single-droplet measurements by Mikami *et al.*[7], who employed the same fuel mixtures in the same atmospheres over the same pressure range. The only difference between this study and that of ref. 7 for single droplets is the ignition energy. Mikami *et al.* varied the ignition energy with the experimental condition so as to avoid overloading the ignition, whereas in the present study we used a constant ignition energy. For that reason, a number of single droplet tests were performed in the present study to determine the influence of the ignition energy. Although the critical pressures of heptane(2.74MPa) and hexadecane(1.41MPa) are below the maximum pressure of the present results, distinctive transcritical behaviors such as burning-time minima are not anticipated to occur in this atmosphere until pressures well above the maximum tested[7]. In other words, qualitatively subcritical behavior was anticipated and indeed was observed. The general character of the combustion process, involving irregularities of the liquid surface, increasing with pressure, revealed by the backlit photographs, resembled that observed and reported previously(Fig. 10 and Fig. 11)[7].

Figure 12 shows representative histories of the square of the droplet diameter for three different pressures at an initial hexadecane mass fraction Y_0 of 0.33. This figure, for the two-droplet experiments with $l/d_0 = 1.7$, reveals that the three-stage combustion of binary fuels (the first stage involving heptane vaporization, the second stage a plateau associated with increasing surface temperature and the third stage involving hexadecane vaporization as well), previously documented for single droplets, also occurs for strongly interacting droplets.

Figure 13 shows the droplet and flame history for a single droplet and droplet pair ($l/d_0 = 1.78$) at a pressure of 2 MPa and initial hexadecane mass fraction of 0.63. This figure clearly shows that the burning time of the strongly interacting droplet pair exceeds that of the single droplet. Comparison of Figs. 12 and 13 shows that the plateau occurs sooner for droplets with a higher initial hexadecane mass fraction, as expected. The ratio of the two-droplet burning time, with $l/d_0 = 1.78$, to the single-droplet burning time in Fig. 13 is roughly $2^{2/3}$, the limiting value expected[22] if the two droplets were to burn as a single droplet having the volume of the two droplets.

Also shown in Fig. 13 are the flame-diameter histories for the single droplet and the droplet pair. The single-droplet history shows a small flame contraction in the second(plateau) stage. The two-droplet flame diameter history in Fig. 13 behaves quite differently. The flame contraction in the second stage was either barely perceptible or not detectable at all. Instead, after a small and rapid initial increase, the two-droplet flame diameter remains nearly constant or decreases slowly with time. This behavior results from the influence of the droplet separation on the flame shape through the nonspherical gaseous fuel concentration field of the interacting droplets.

A final important observation that can be made from Fig. 13 is that the liquid in the droplets disappears before the flame disappears. The last droplet data points in Fig. 13 are those for which the filament supports are bare, but flame persists after that, especially in two-droplet experiments. It has long been known from theory[14,27] that the flame diameter increases initially, reaches a maximum then decrease rapidly near the end of combustion but persists after droplet disappearance as the remaining fuel vapor burns. The single-droplet results in Fig. 13 after the second stage are in good qualitative agreement with this prediction. In theory, even if the droplet burns to zero diameter the flame lasts longer than the droplet(so long as it is not extinguished by finite-rate chemistry). The presence of the fiber causes a much larger amount of fuel vapor to be present after the liquid is completely consumed, and Fig. 13 shows that this effect is substantially enhanced by strong droplet interaction through the additional volume contained between the droplets. Although finite-rate chemistry can cause the flame to extinguish prior to complete liquid-fuel consumption[28-30], the elevated pressures with these fairly reactive fuels can promote flame robustness, causing the flame to continue to burn to very small diameters, as seen at the end of the flame-diameter records in Fig. 13.

To investigate the extent of the initial heat-up periods of the first and the third stages for the binary-fuel droplets, two characterstic times are defined in this article (Fig. 14). One is transition time, which is the time at the onset of the second stage (t_C/d_0^2; corrected to d_0=1mm). The other is (t_{23}/d_0^2; corrected to d_0=1mm) is defined as the droplet lifetime minus transition time ($t_d/d_0^2 - t_c/d_0^2$;also corrected to d_0=1mm). In this article, they will be called as the first heat-up time and the second heat-up time, respectively.

Comparisons with Previous Results

From droplet-diameter histories like those in Fig. 12, it is possible to define burning-rate constants K_I and K_3 separately for the first and third stages[7]. These constants are defined here from the maximum slopes in each stage, which are achieved near the end of the stage. Figures 15-(a) and 15-(b) show the results as functions of initial fuel concentration for various pressures for single droplets and droplet pairs, respectively. The single-droplet results are in excellent agreement with those reported earlier[7], despite the difference in ignition strategy. This result is understandable in that, by the time that the maximum slopes are attained, the influence of the different initial conditions have diminished. The different ignition procedures can affect the total burning time but not the maximum slopes. Additionally, Fig. 15-(b) shows that, under most conditions and within experimental accuracy, droplet interactions have a fairly small influence on the maximum slopes. The interaction effects are greatest for the pure fuels, whose spacing ratios l/d(where d is the instantaneous droplet diameter) experience the greatest change during the (single) stage of combustion.

Figure 16 compares the critical liquid droplet volume fraction for onset of the second stage of the present study with previous results[7]. This volume fraction is the ratio of the droplet volume at the onset of the second stage to the initial droplet volume. Theoretically, for complete liquid-phase mixing, the data would lie along the straight diagonal line. Shaw[12, 13] analyzed the corrections introduced by the development of a static liquid-phase diffusion layer at the droplet surface, identifying $\varepsilon = 8D_l/K$ as the relevant parameter, where K is the burning-rate constant and D_l the liquid-phase heptane diffusion coefficient. Values of ε for these mixtures are estimated to be between about 0.05 to 0.10[7]. Liquid-phase mixing through liquid motion will increase the effective value of ε , approaching the straight line for perfect mixing.

Figure 16 shows that all data correspond to values of ε between 0.05 and 0.20, suggesting that some liquid-phase mixing occurs, but not perfect mixing. This is consistent with the somewhat irregular surface shapes seen in the backlit images. These liquid-phase motions can be promoted by a surface-tension driven flows caused by either a temperature or concentration gradient. In any given set of experiments, there seems to be very little effect of pressure on the critical volume fraction. There are, however, observable differences between the present single-droplet results and the previously reported results[7], with the present results nearer the diffusion-controlled limit at small Y_0 and farther from that limit at large Y_0. This suggests that the extent of liquid-phase motion is influenced by the method of ignition. Since the droplet is initially cold, the ignition impulse can induce significant temperature gradients leading to a surface-tension flow. It is not surprising therefore that the ignition condition can effect flow inside the liquid. Further, as the burning proceeds the heptane is depleted at the droplet surface, and as the heptane-rich fuel from the droplet interior comes to the surface, a tangential concentration gradient occurs at the surface which can cause the motion in the liquid to persist well into the droplet lifetime. The single-droplet and droplet-pair critical volume fractions are not very different, consistent with the same ignition impulse per droplet in each case.

Droplet and Flame Lifetimes

Figure 17 shows the dependence of droplet and flame lifetime on pressure for $Y_0=0$. Similar results were obtained for other values of Y_0. The droplet lifetimes decrease with increasing pressure, for reasons previously explained[7]. Flame lifetimes appreciably exceed droplet lifetimes, as discussed above. In addition, droplet-pair lifetimes exceed single-droplet lifetimes, as discussed and explained above. The dependence of the droplet lifetime on the fuel composition is shown in Fig. 18 for droplet pairs. Single-droplet results have been presented and discussed previously[7]. There is general qualitative agreement between these results, although the two-droplet burning times are, of course, longer. The reason for the maximum in these curved was explained in ref. 7.

To investigate how the combustion history depends on droplet spacing in the regime of strong interaction, measurements were made at different values of l/d_0 in this regime. Figure 19 shows droplet lifetimes as functions of l/d_0 at three different pressures, for $Y_0=0.33$ with l/d_0 between 1.7 to 6.0, the approximate extent of the strongly interacting regime. Similar results were obtained for flame lifetimes and for other values of Y_0, but are not presented. The results show that the lifetimes decrease with increasing l/d_0 in this regime. This is in accordance with theoretical predictions[23,24] and with previous low-pressure pure-fuel experimental results[19, 22]. The mutual shielding of the droplets increases as they approach each other, decreasing local gas-phase concentration and temperature gradients and thereby decreasing burning rates. The present results demonstrate that these effects persist for high pressures and for binary fuels. The decrease is just as strong when there is staged combustion as for pure fuels. The magnitude of the effect does, however, decreases with increasing pressure, as in Fig. 19. This is consistent with a decrease in characteristic gas-phase diffusion lengths with increasing pressure. Although the inverse dependence of diffusivities on pressure is counterbalanced by the increase in density, peak temperatures are generally higher at elevated pressures(for example, through reduced dissociation), so that the product of the diffusivity and the density increases and thus diffusion lengths decrease. This effect should be small, as indeed it appears to be in Fig. 7.

At separation distances beyond the strong-interaction regime, it was observed for pure heptane droplets at atmospheric pressure that the burning time increases with increasing separation, that is, there is a minimum in the burning time[22]. This is well known in normal gravity and is explained as an effect of buoyancy. In the microgravity experiments, it was explained by radiant energy transfer, with the flame of the nearby droplet enhancing the burning rate through its additional radiant heating[22]. This effect is largest during the heat-up phase of the droplet and reduces the total burning time mainly by reducing the initial heating period. The data points in Fig. 7 for single droplets($l/d_0=\infty$) show that the same phenomenon must exist at high pressures and for binary fuel droplets. The existence of this long-range interaction is quite reasonable, for example in view of the influence of radiant energy transfer on flame spread.

Estimation of unsteady-interaction effects

Following Miyasaka and Law [19], we introduce the burning rate correction parameter:

$$\eta\,(d/d_0) \equiv K\,(d/d_0)\,/\,K_S(d/d_0) \qquad (1)$$

where $K\,(d/d_0)$ is the instantaneous burning rate constant of droplet pair and $K_S\,(d/d_0)$ is instantaneous burning rate constant of the single droplet for the normalized droplet diameter (d/d_0). This type of figure can only be constructed for the pure fuel because the occurrence of the staged combustion will further complicate the vaporization phenomena. Dependence of the instantaneous burning rate correction parameter on l/d by every 0.05 (d/d_0) for three pressures is shown in Fig. 20. Figure 20 clearly shows that for interacting droplets, liquid-phase unsteadiness is very strong at high pressure. At P=1.0MPa, the value of η is relatively low during the initial heat-up period and slowly approach 1.0. At P=2.0MPa, η approaches 1.0 quickly and remains close to 1.0 thereafter. For P=3.0MPa, η approaches 1.0 quickly just as for P=2.0MPa reaches a maximum then decreases in the middle of burn and slowly increases until the end. Note, however, from Fig. 17 that the difference in the droplet lifetime between the single droplet and droplet pair is small. This fact suggests that increase of droplet lifetime by interaction is strongly dependent on the unsteadiness in the initial heat-up period. The relatively low value of η for P=3.0MPa originates in the fuel accumulation effects during the latter period of combustion. These results suggest that the slopes of the burning rate constant in the initial heat-up period strongly affects the total liquid-phase lifetime, and corresponds to the fact that interaction effects generally decrease with increasing pressure, as demonstrated in Fig. 19.

Figures 21(a) and 21(b) show the dependence of transition time (t_C) and second and third-stage time (t_{23}) on initial hexadecane mass fraction for three different pressures for both single droplet and droplet pairs, respectively. These times include both an unsteady-initial heat-up period and a quasi-steady vaporizing period for the first stage and the third stage. The transition time (t_C) is another characteristic representing the onset of the second stage and demonstrates the effects of unsteadiness unlike critical volume fraction.

Figure 21(a) shows the transition time of the droplet pair ($l/d_0=1.7\pm0.1$) exceeds that of a single droplet for each fuel composition and pressure. This indicates that the initial heat-up period is lengthened by strong interaction. For binary-fuel droplets in a high pressure ambient, we reported that the two-droplet flame diameter history is quite different from the single-droplet flame diameter history. Unlike the single droplet case, the flame contraction in the second stage was either barely perceptible or not detective. Instead, the two-droplet flame diameter (defined as the maximum dimension of the visible flame) remains nearly constant or decreases slowly with time. This behavior was explained by the influence of the droplet separation on the flame shape through the nonspherical gaseous fuel concentration field of the interacting droplets. This flame behavior should reduce the temperature gradient near the fuel surface in the droplet-pair case and thus lengthen the t_C.

Figure 21(b) shows the dependence of the second heat-up time (t_{23}) on initial hexadecane mass fraction for three different pressures. The value of t_{23} remains nearly constant or increases slightly with the increase of initial hexadecane mass fraction for each pressure condition, unlike the tendency seen in t_C (Fig.21(a)). This fact indicates that sufficient temperature and some liquid-phase mixing, demonstrated and explained above, may obscure the difference of initial composition.

The order of the second heat-up time (t_{23}) for the single droplet and the droplet pair is different for each Y_0. When $Y_0=0.11$, t_{23} of the droplet pair is smaller than that of the single droplet for each pressure. From Fig. 21(a), the first heat-up period (t_C) for $Y_0=0.11$ is large and thus the liquid droplet should be hotter and more fuel vaporized than a smaller t_C. As a result, this t_C should make t_{23} shorter. In the case of $Y_0=0.63$, the t_{23} of the droplet pair exceeds that of the single droplet. This is because the transition occurs so fast (small t_C) that fuel consumption and heat up of the liquid is reduced (compared to large t_C). For $Y_0=0.33$, such a distinction could not be made. The results from Figs. 21(a) and 21(b) demonstrate that the initial heat-up periods of the first stage and third stages are affected by strong interaction.

4. CONCLUSION

In the present study, the combustion of two close-spaced fuel droplets of binary liquid mixtures at high pressures ranging from subcritical to supercritical was examined.

At first, we performed a series of experiments using zero air as atmosphere, and the main conclusions of the zero air test are as follows:

(1) Burning lifetime of heptane droplet takes a minimum on pressure at about the critical pressure of the fuel both for single droplet and droplet pair. Burning lifetime gets smaller as droplet spacing gets smaller in the strongly interacting regime($l/d_0 \leqq 5$).

(2) Burning lifetime of fuel mixtures of heptane/hexadecane is longer than that of pure heptane, and the pressure at which the burning lifetime of mixture takes minimum is much higher than that of pure heptane.

(3) Burning lifetime of strongly interacting droplet-pairs is longer than that of

single droplet, and the pressure at which the burning lifetime of mixture takes minimum is higher than that of single droplet.

(4) The increase of burning lifetime by interaction decreases as pressure increases for each fuel composition.

Especially in high pressure, intense light emission from combustion obscures the backlight, so it is very hard to visualize burning droplet in high pressure. Thus, the reduced oxygen concentration of 0.12 was also employed to aid in visualizing the droplet from the backlit view at high pressure. From the low oxygen tests, the followings can be concluded:

First, we have demonstrated that the staged combustion seen for single droplets still exists for droplet pairs even during strong interaction.

The representative characteristics of staged combustion for droplet pairs were investigated and compared with single-droplet results. It is observed that burning rate constants of the first and the third stages, as well as the transition droplet volume are not strongly affected by interaction, while the burning time of the strongly interacting droplet pair exceeds that of the single droplet. The ratio of the two-droplet burning time with $l/d_0 = 1.7 \pm 0.1$ to the one-droplet burning time is close to the limiting value that would be attained if the two droplets were to burn as a single droplet having the volume of the two droplets.

Droplet lifetimes and flame lifetimes increase with decreasing droplet spacing within the strong-interaction regime and decrease with increasing pressure. This can be explained by the decrease of the fuel concentration and temperature

gradients, as droplets approach each other and by the decrease in the heat of vaporization with increasing pressure. Flame lifetimes exceed droplet lifetimes because of vapor accumulation and very late flame extinction.

In the latter part of this article, we investigated the interaction effects of burning droplet pair at high pressure by examining the unsteadiness in the interacting combustion.

The main conclusions of this part are as following:

1. **Liquid-phase unsteadiness in interactive combustion of two droplets is very strong even at high pressure. Increase of droplet lifetime by interaction is strongly dependent on the unsteadiness in the initial heat-up period. These results suggest that variation of the burning rate constant in initial heat-up period strongly affects the (total) droplet lifetime.**
2. **The flame behavior of the burning droplet pair reduces the temperature gradient near the fuel surface and thus lengthens the transition time compared to that of single droplet.**
3. **Both the initial heat-up period of the second heat-up time are affected by interaction.**

The results help to improve understanding of droplet interaction effects of binary-fuel combustion at high pressure.

References

[1] Faeth.G. M., Dominicis, D. P., Tulpinsly, J. F. and Olson, D. R., *Twelfth Symp. (Int.) Combust.*, The Combustion Institute, Pittsburgh, PA, 1969, pp. 9-18.

[2] Lazer, R. S., and Faeth, G. M., *Thirteenth Symp. (Int.) on Combust.*, The Combustion Institute, Pittsburgh, PA, 1971, pp 801-811.

[3] Canada, G. S. and Faeth, G. M., *Fourteenth Symp. (Int.) on Combust.*, The Combustion Institute, Pittsburgh, PA, 1973, pp 1345-1354.

[4] Kadota, T. and Hiroyasu, H., *Eighteenth Symp. (Int.) on Combust.*, The Combustion Institute, Pittsburgh, PA, 1981, pp 275-282.

[5] Niioka, T. and Sato, J., *Twenty-First Symp. (Int.) on Combust.*, The Combustion Institute, 1988, pp 625-631.

[6] Sato, J., Tsue, M., Niwa, M. and Kono, M., *Combust. Flame* 82:142-150 (1990).

[7] Mikami, M., Kono, M., Sato, J., Dietrich, D. L. and Williams, F. A., *Combust. Sci. Tech.*, Vol. 90, pp 111-123 (1993).

[8] Vieille, B., Chauveau, C., Chesneau, X., Odeïde, A. and Gökalp, I., *Twenty-Sixth Symp. (Int.) on Combust.*, The Combustion Institute, 1996, pp 1259-1265.

[9] Mikami, Habara, O., M., Kono, M., Sato, J., Dietrich, D. L. and Williams, F. A., *Combust. Sci. Tech.*, vol. 124, pp 295-309 (1997).

[10] Spalding, D. B., *ARS J*, pp 828-835 (1959).

[11] Umemura, A., *Twenty-First Symp. (Int.) on Combust.*, The Combustion Institute, Pittsburgh, PA, 1987, pp 463-471.

[12] Shaw, B. D., *Combust. Flame*, 81:277-319 (1990).

[13] Shaw, B. D. and Williams F. A., *Int. J. Heat Mass Transfer*, 33:pp 301-317 (1990).

[14] Shuen, J. S., Yang, V. and Hisiao, C. C., *Combust. Flame*, 89: pp 299-319. (1992).

[15] Rex, J. F., Fuhs, A. E. and Penner, S. S., *Jet Propul.* 26: 179-187 (1956).

[16] Kanevsky, J., *Jet Propul.* 26: 788 (1956).

[17] Brzustowski, T. A., Twardus, E. M., Wojcicki, S., and Sobiesiak, A., *AIAA J.* 17: 1234-1242 (1979).

[18] Fedoseeva, N. V., *Adv. Aerosol Phys.* 2: 110-118 (1972).

[19] Miyasaka, K. and Law, C. K., *Eighteenth Symp. (Int.) on Combust.*, The Combustion Institute, Pittsburgh, PA, 1981, pp 283-292.

[20] Xiong, T. Y., Law, C. K. and Miyasaka, K., *Twentieth Symp. (Int.) on Combust.*, The Combustion Institute, Pittsburgh, PA, 1985, pp 1781-1787.

[21] Konishi, K., Kono, M. and Iinuma, K., *Trans. Jpn. Soc. Mech. Eng.* 51: 2218-2224 (1985).

[22] Mikami, M., Kato, H., Sato, J. and Kono, M., *Twenty-Fifth Symp. (Int.) on Combust.*, The Combustion Institute, Pittsburgh, PA, 1994, pp 431-438.

[23] Labowsky, M., *Combust. Sci. Tech.*, Vol. 22: 217-226 (1980).

[24] Umemura, A., Ogawa, S. and Oshima, N., *Combust. Flame* 41:45-55 (1981).

[25] Umemura, A., *Eighteenth Symp. (Int.) on Combust.*, The Combustion Institute, Pittsburgh, PA, 1981, pp 1355-1363.

[26] Jiang, T. L. and Chiang, W., *Combust. Flame* 97:17-34 (1994).

[27] Crespo, A. and Liñán, A, *Combust. Sci. Tech.*, Vol. 11: pp 9-18 (1975).

[28] Law, C. K. and Williams, F. A., *Combust. Flame* 19:393-405 (1972).

[29] Law, C. K., Chung, S. H. and Srinivasan, N., *Combust. Flame* 38:173-198 (1980).

[30] Dietrich, D. L., Haggard JR., J. B., Dryer, F. L., Nayagam, V., Shaw, B. D. and Williams, F. A., *Twenty-Sixth Symp. (Int.) on Combust.*, The Combustion Institute, Pittsburgh, PA, 1996, pp 1201-1207.

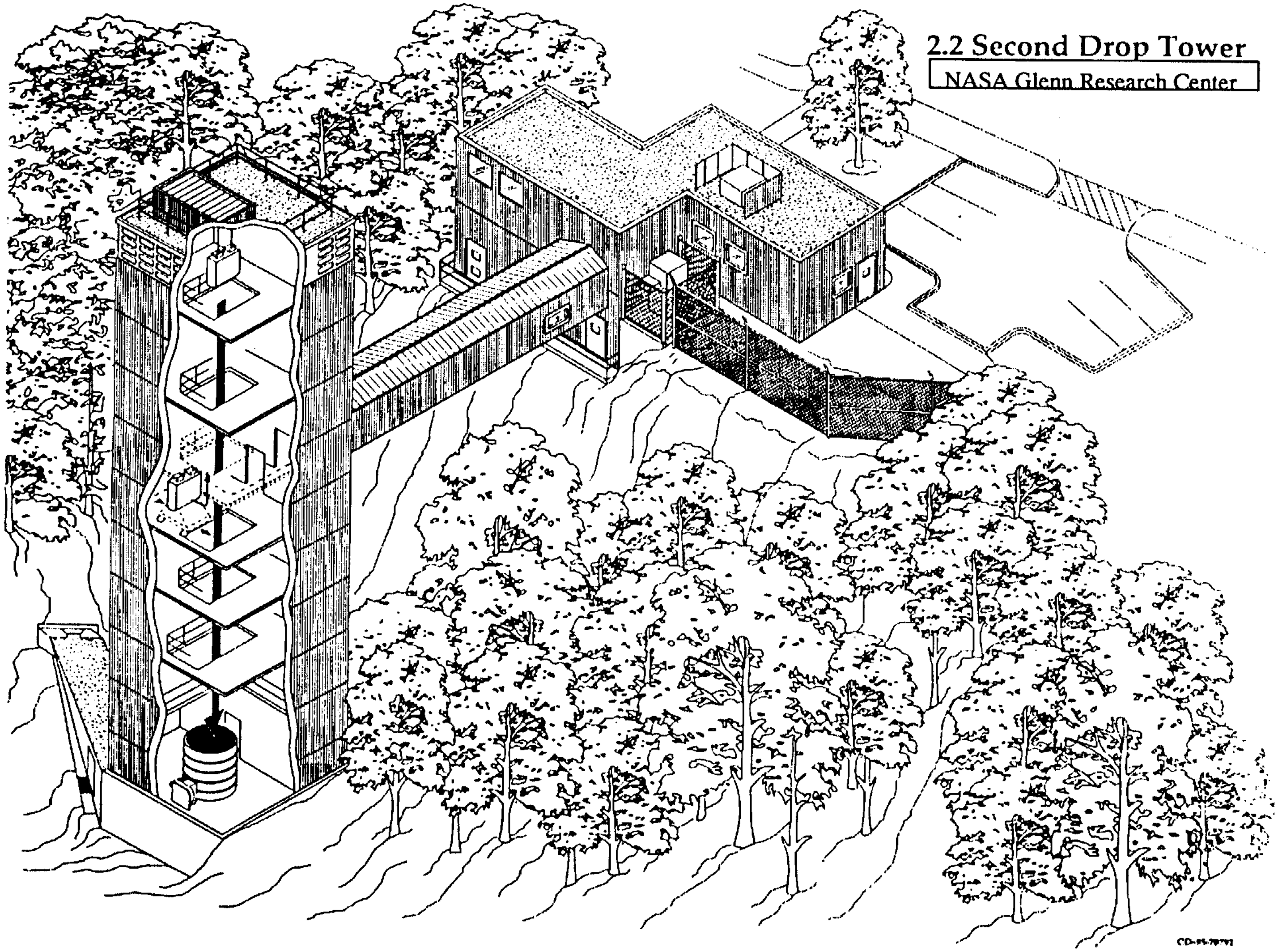

Fig.1 NASA Glenn Research Center 2.2 Second Drop Tower

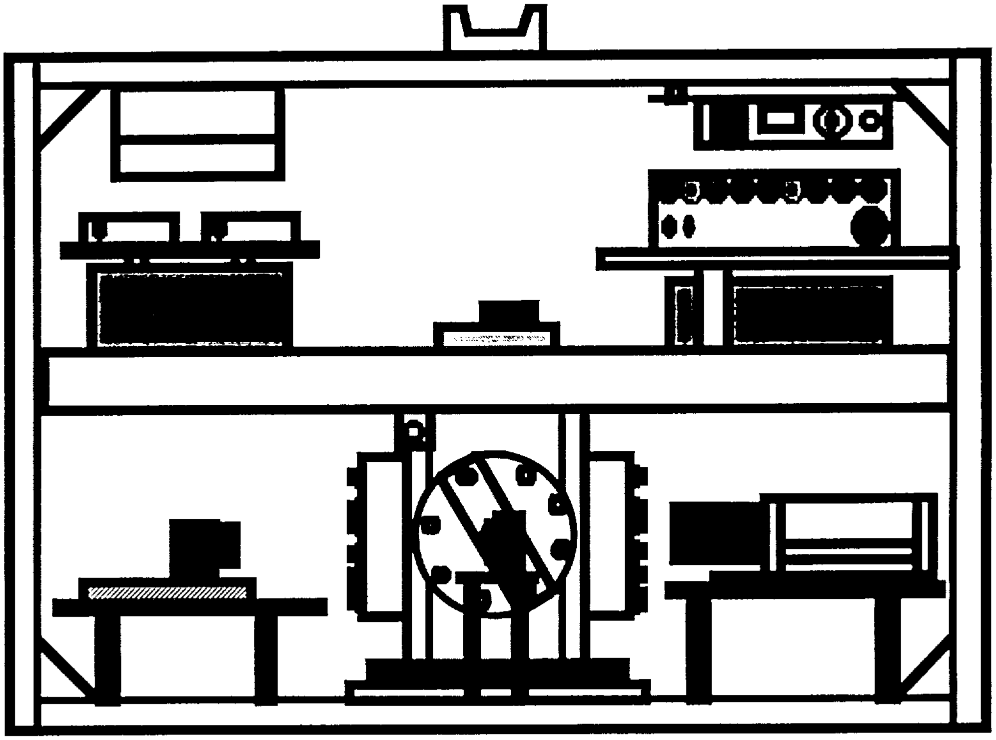

Fig. 2 A schematic of the experimental apparatus

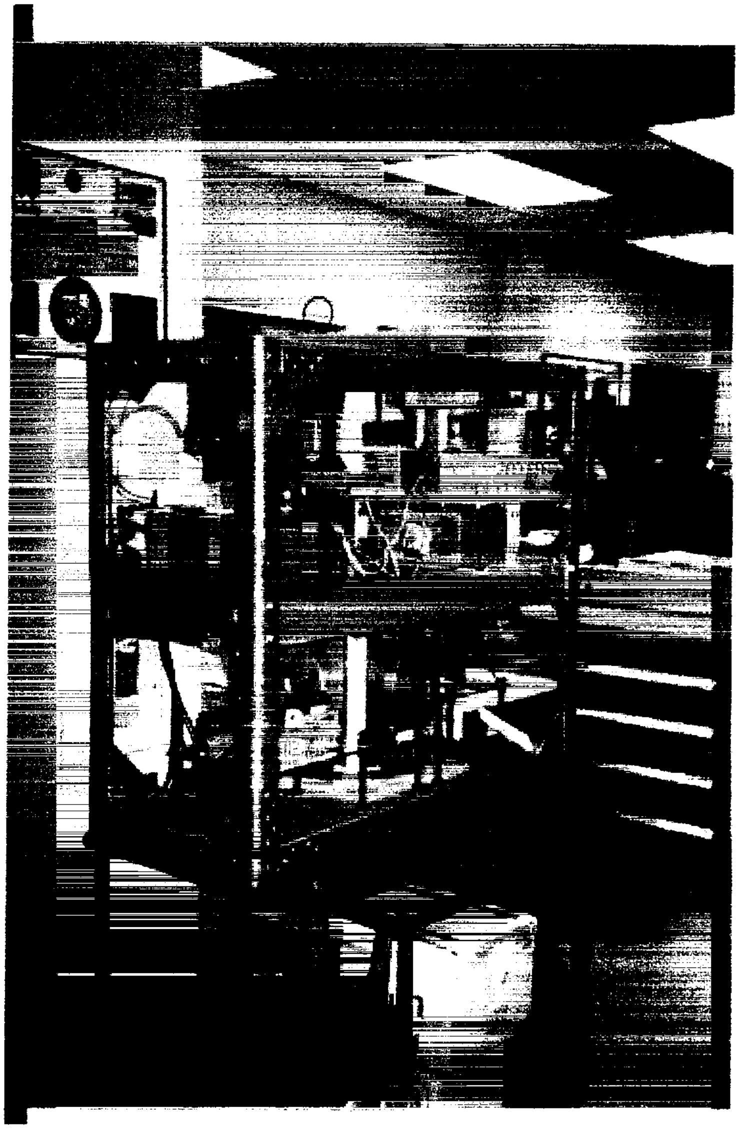

Fig. 3 A photograph of the experimental apparatus

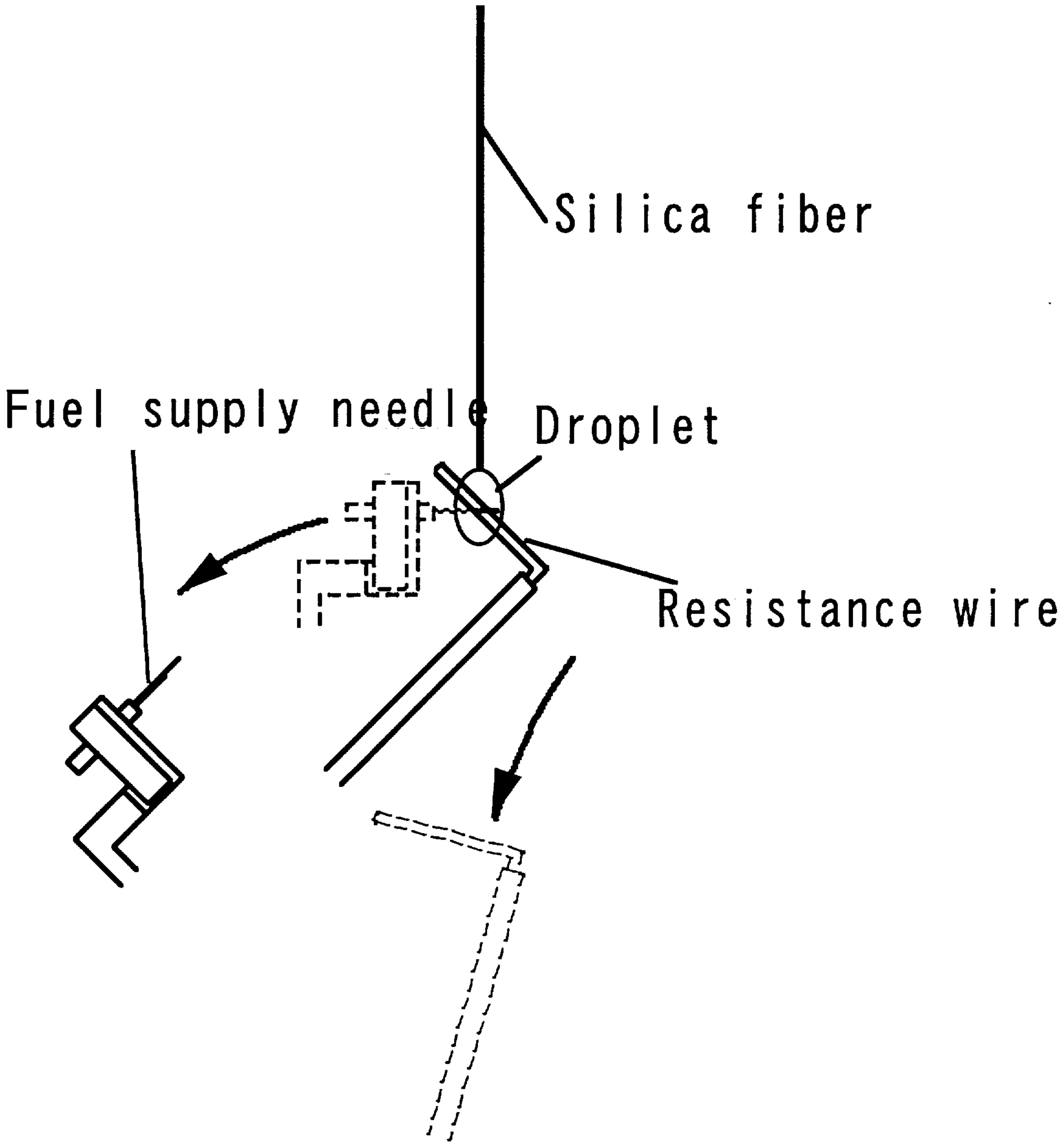

Fig. 4 Fuel supply system and ignitor

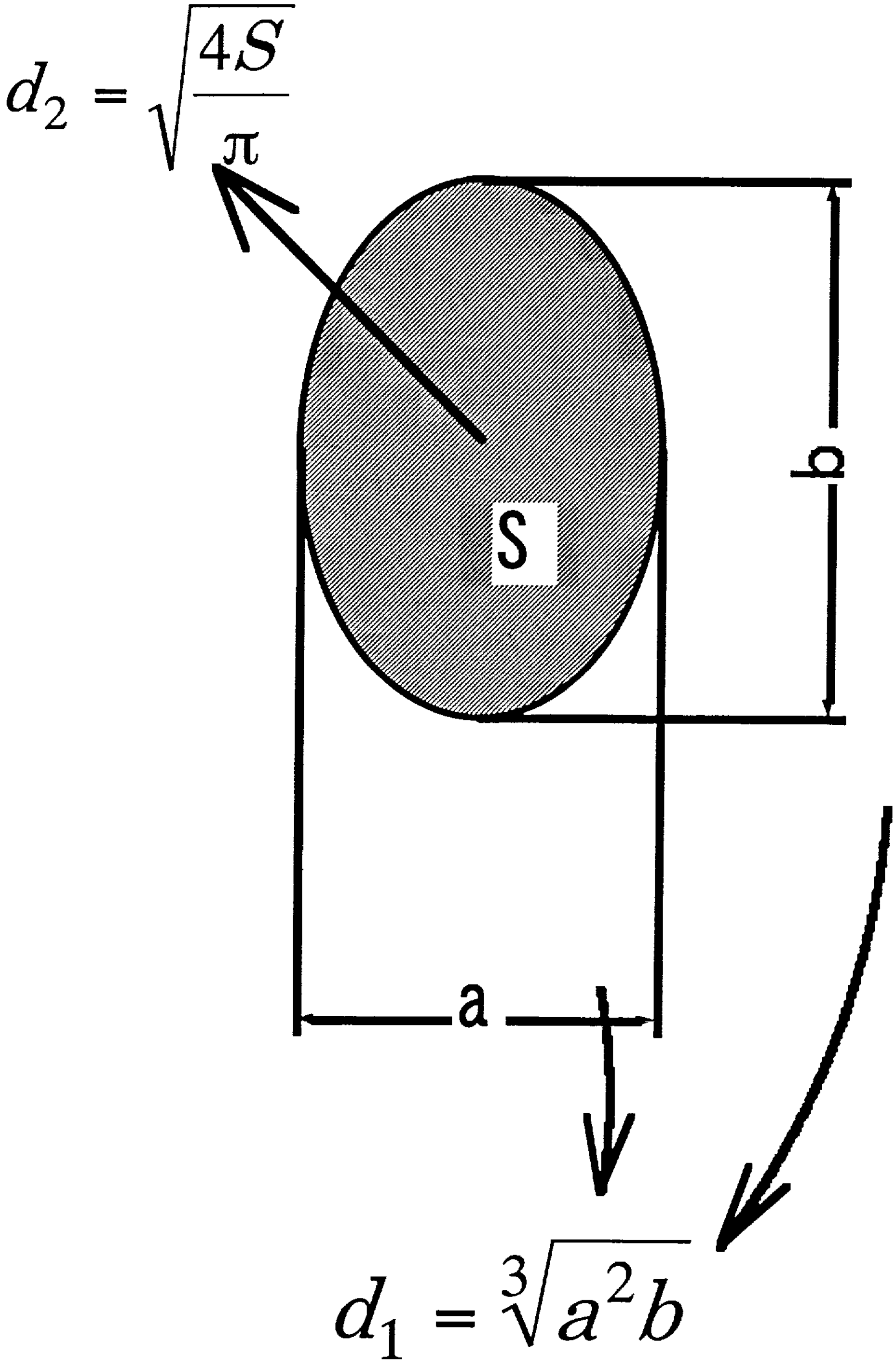

Fig. 5 Equivalent droplet diameter

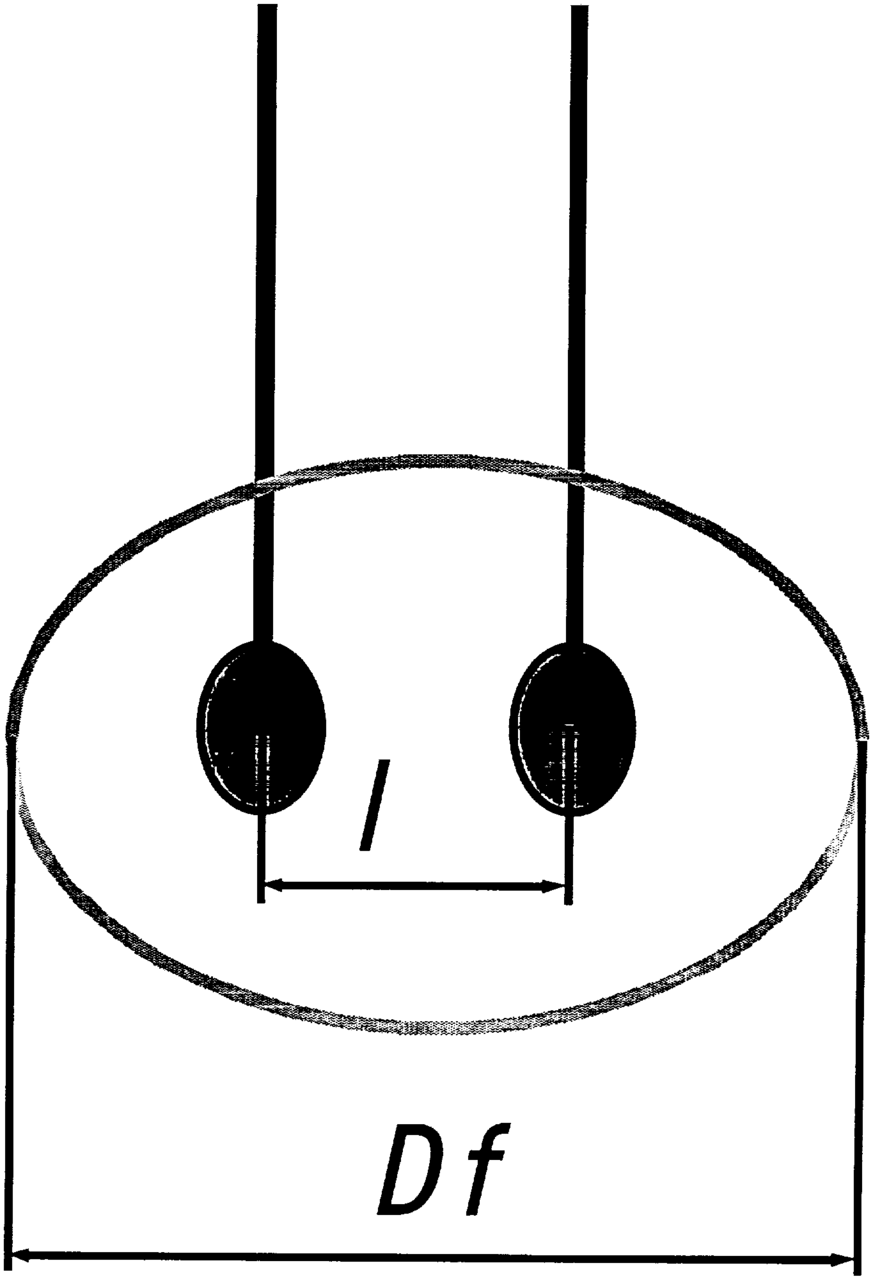

Fig. 6 Droplet separation distance, l, and flame diameter, D_f.

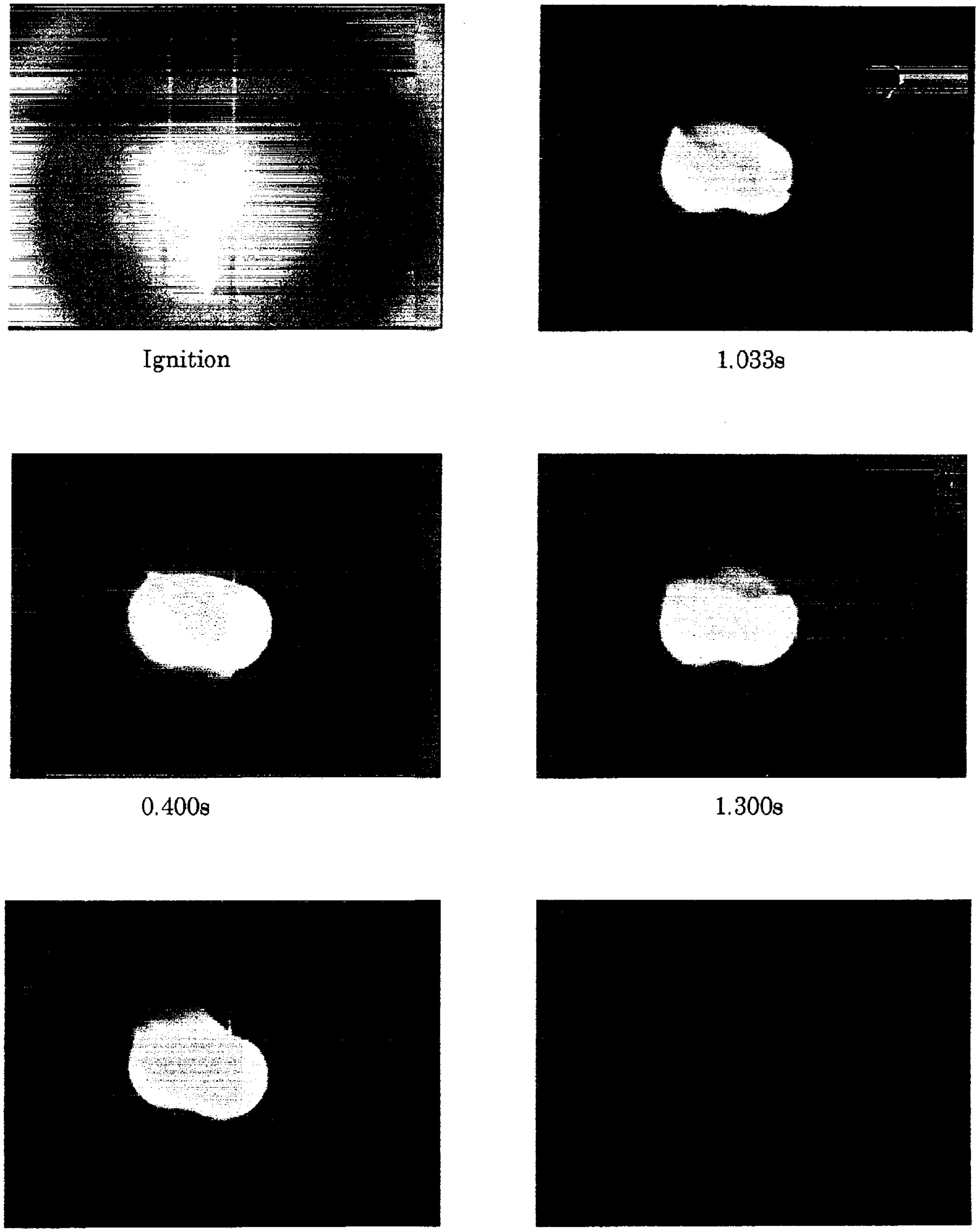

Ignition

1.033s

0.400s

1.300s

0.800s

1.700s

Fig. 7 A sequential photograph of burning phenomena of a droplet pair ($Y_0=0.11$, $l/d_0=4$, $P=1MPa$, $X_0=0.21$)

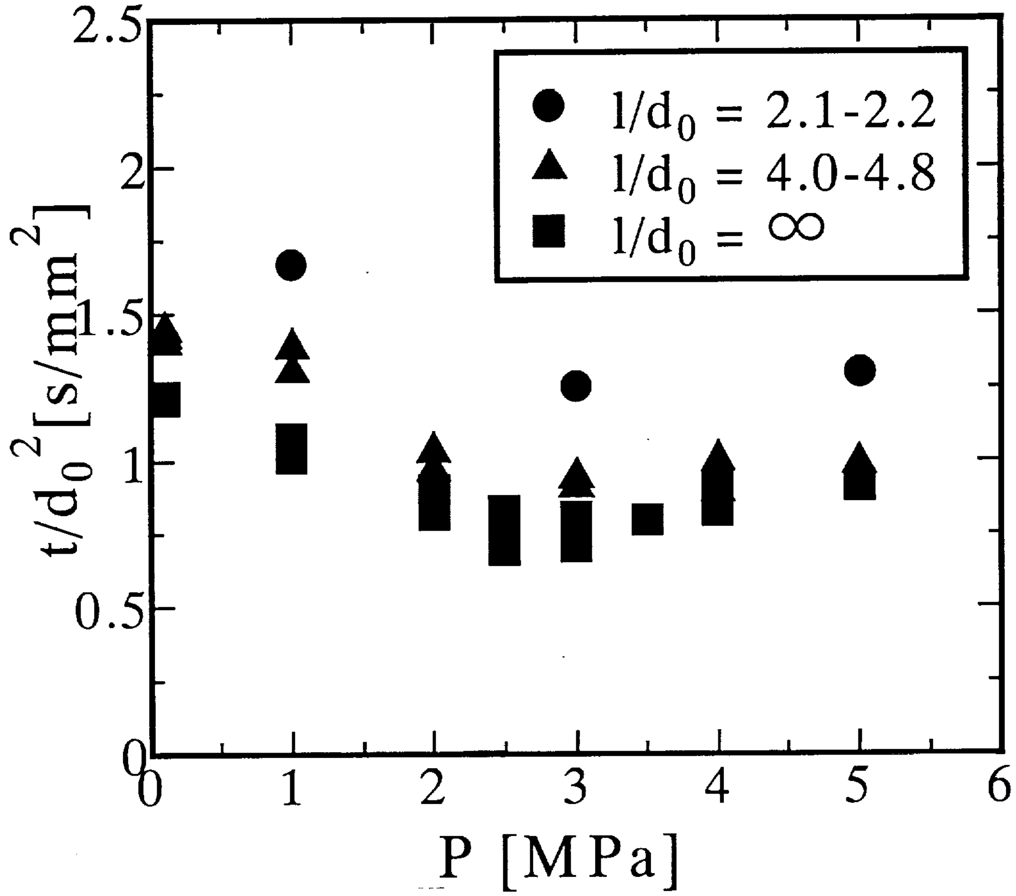

Fig. 8 The dependence of burning lifetime on pressure for pure heptane (Y_0=0), X_0=0.21

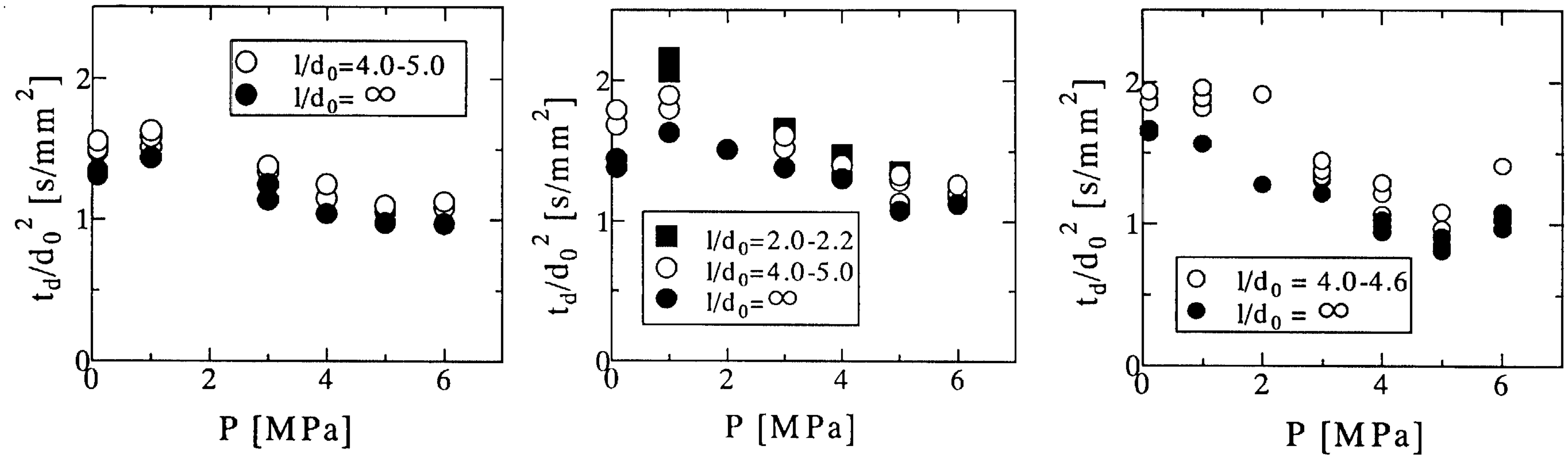

(a) $Y_0 = 0.11$ (b) $Y_0 = 0.33$ (c) $Y_0 = 0.63$

Fig. 9 Dependence of burning lifetime on pressure for fuel mixtures (X_0=0.21) (a) Y_0=0.11 (b) Y_0=0.33 (c)Y_0=0.63

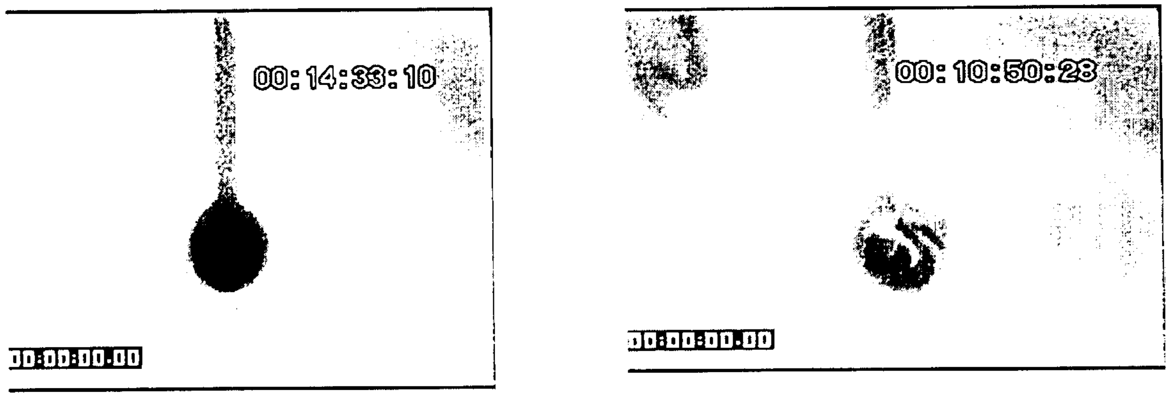

P=2.0MPa P=3.5MPa

Fig. 10 Backlit photographs of the burning droplet at subcritical and supercritical pressures, $Y_0=0$ (pure heptane), $X_0=0.12$

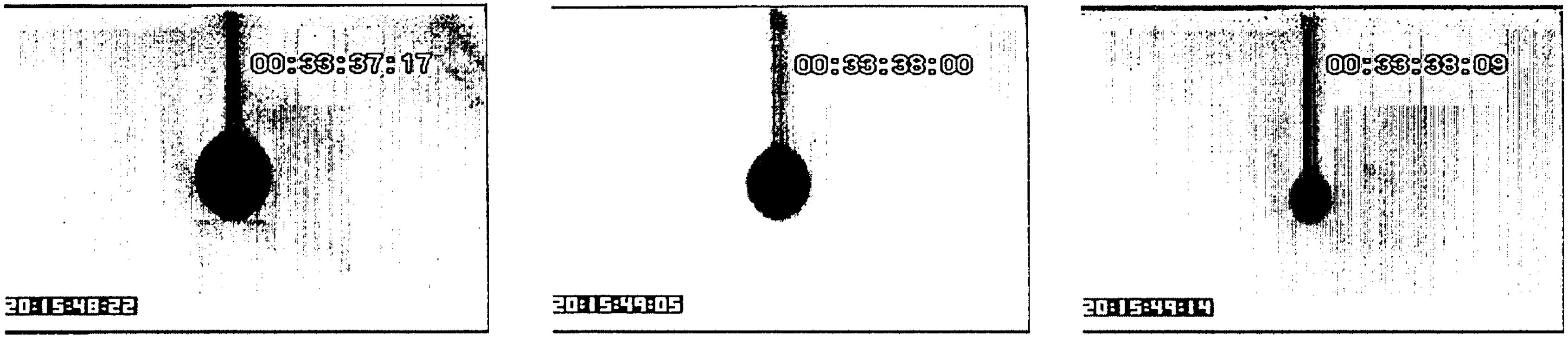

first stage   second stage(plateau)   third stage

Fig. 11 Sequential photographs of the burning droplet at different stages (Y_0=0.33, P=1.5MPa, X_0=0.12)

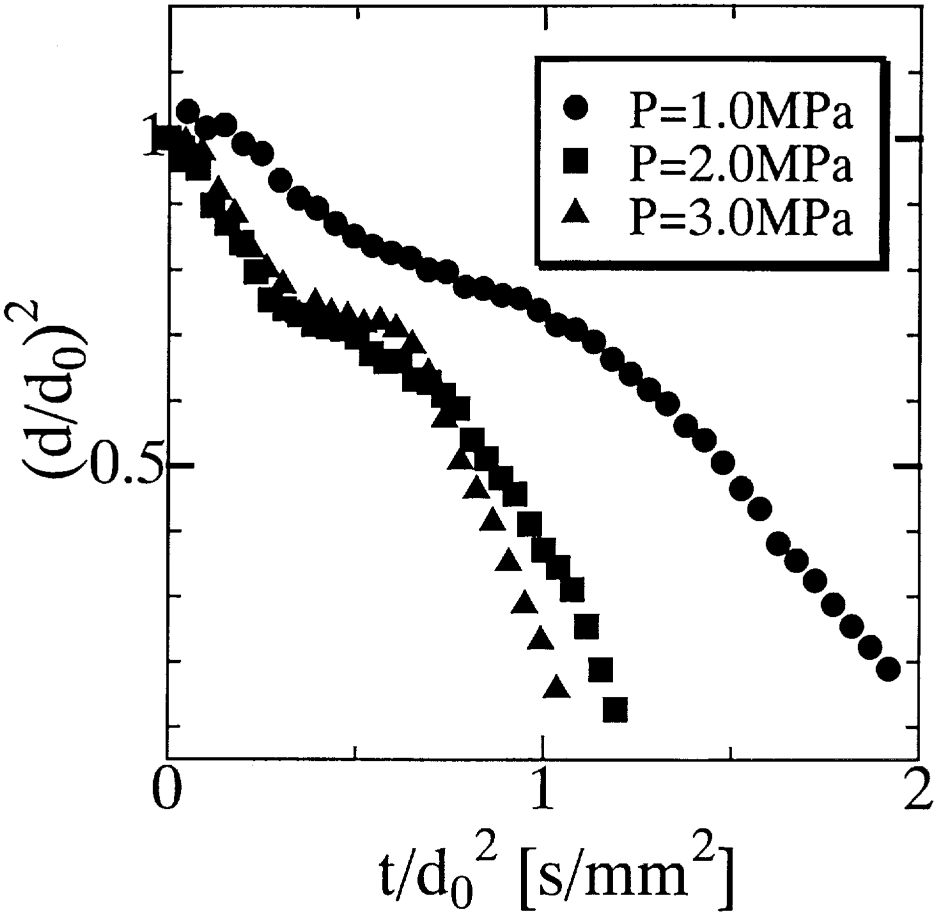

Fig. 12 Histories of droplet diameter squared at different ambient pressures (Y_0=0.33, l/d_0=1.7±0.1).

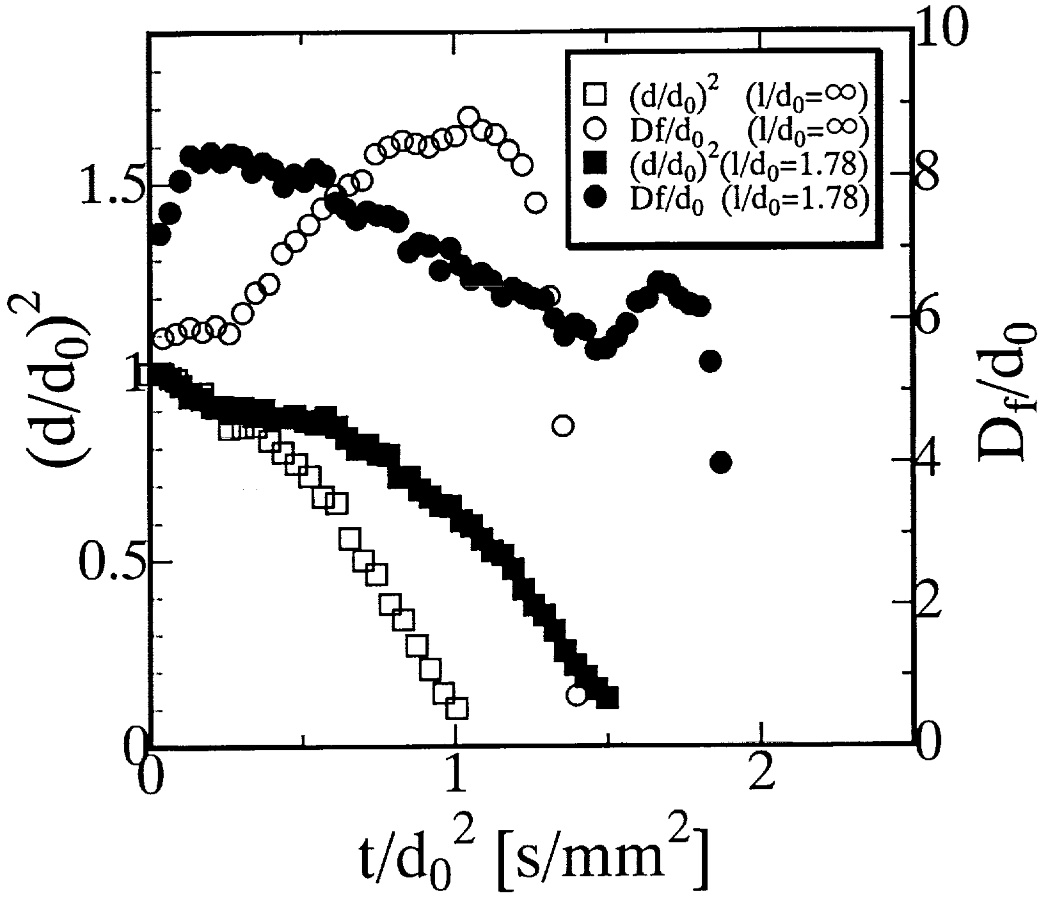

Fig. 13 Histories of droplet diameter squared $(d/d_0)^2$ and maximum flame diameter (D_f/d_0) for single droplet and droplet pairs $(Y_0=0.63, P=2MPa)$.

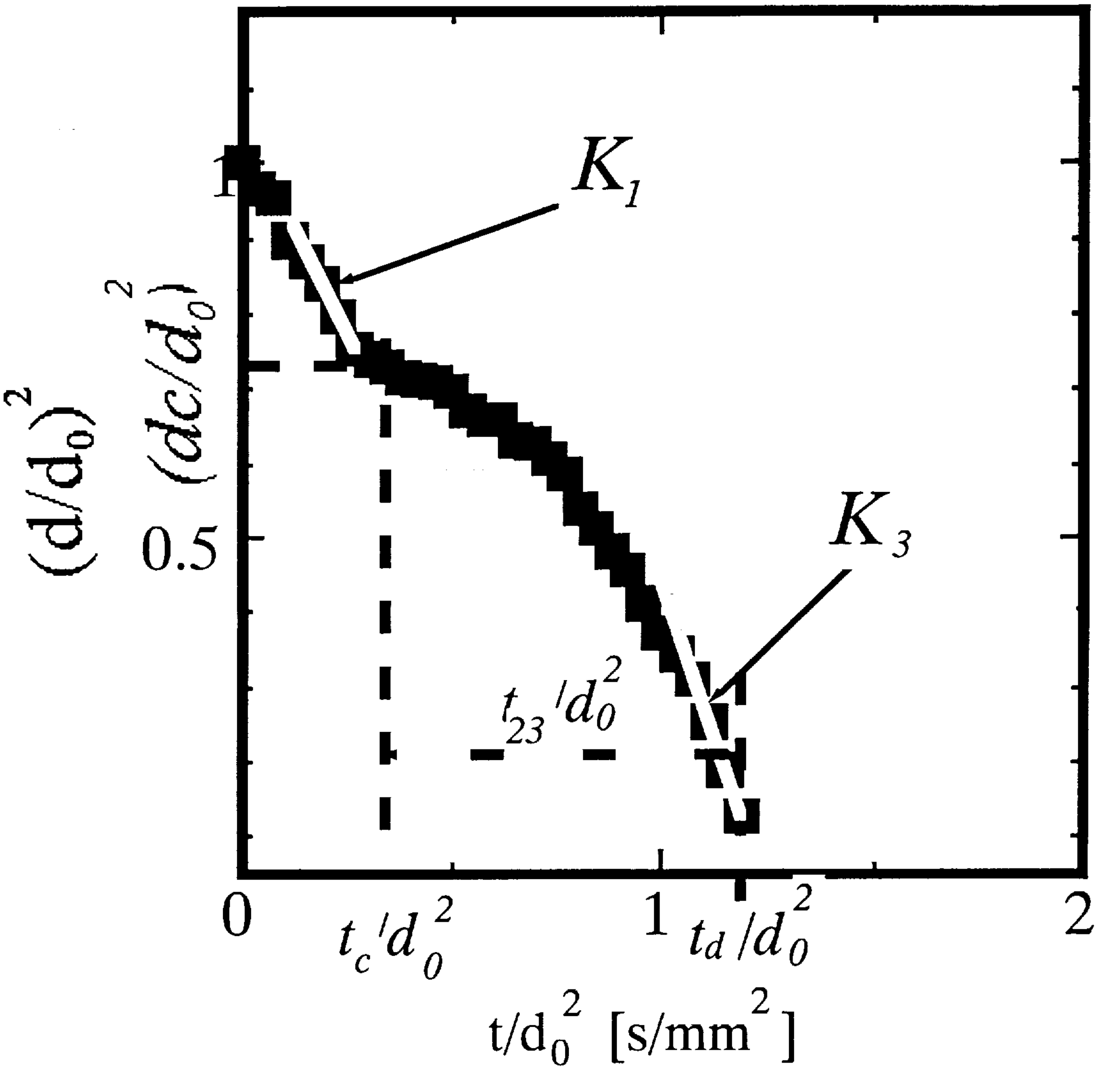

Fig. 14 A typical droplet diameter squared history for a binary-fuel droplet that undergo the three-stage combustion (droplet pair (l/d_0= 1.7±0.1), Y_0=0.33, P=2MPa). K_1, K_3, (d_c/d_0), t_d/d_0^2, t_c/d_0^2 and t_{23}/d_0^2 are schematically shown in this figure.

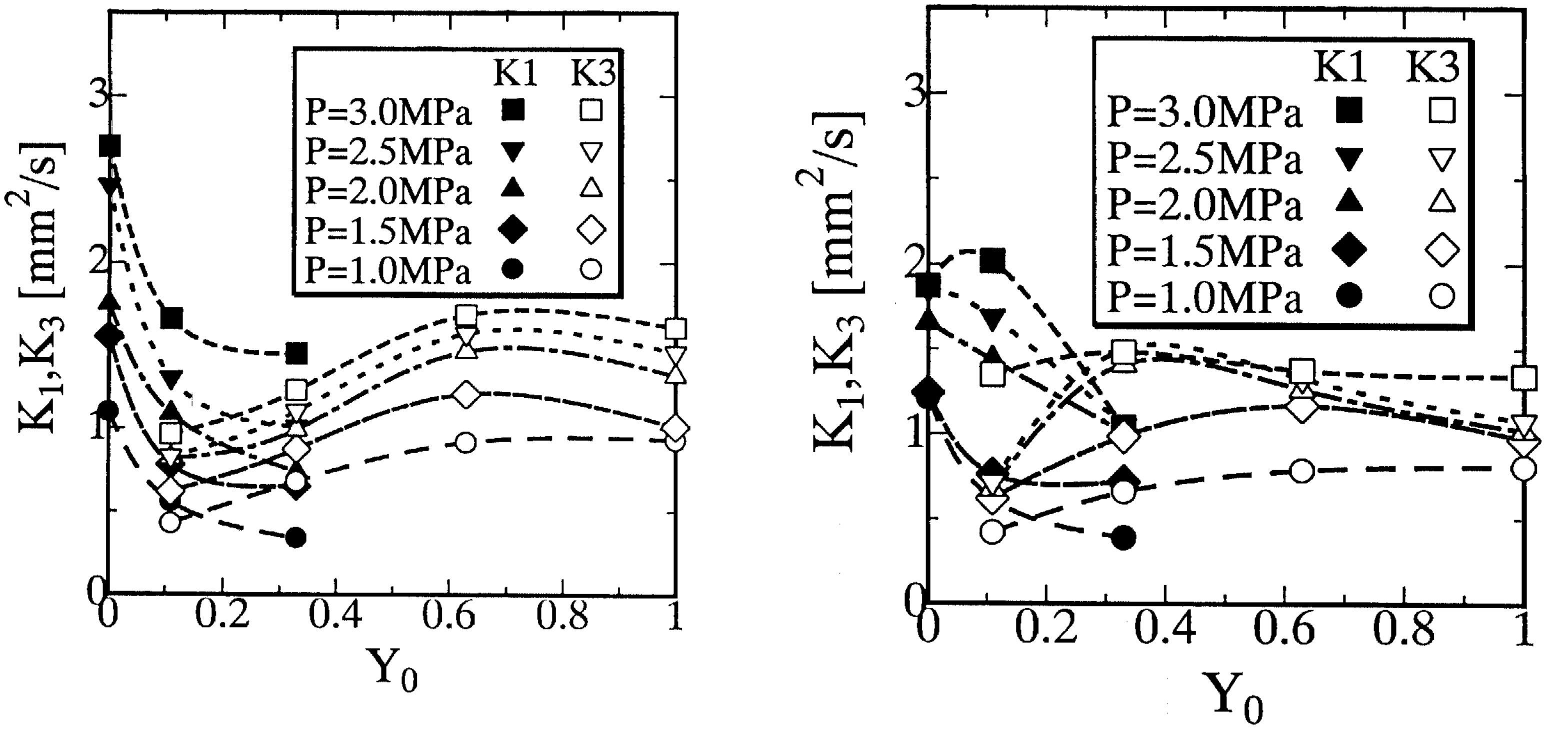

(a) single droplet

(b) droplet pairs (l/d_0=1.7±0.1))

Fig. 15 Dependence of the burning rate constant in the first stage, K_1, and in the third stage, K_3, at different ambient pressures on the initial hexadecane mass fraction, Y_0
((a) single droplet, (b) droplet pairs (l/d_0=1.7±0.1)).

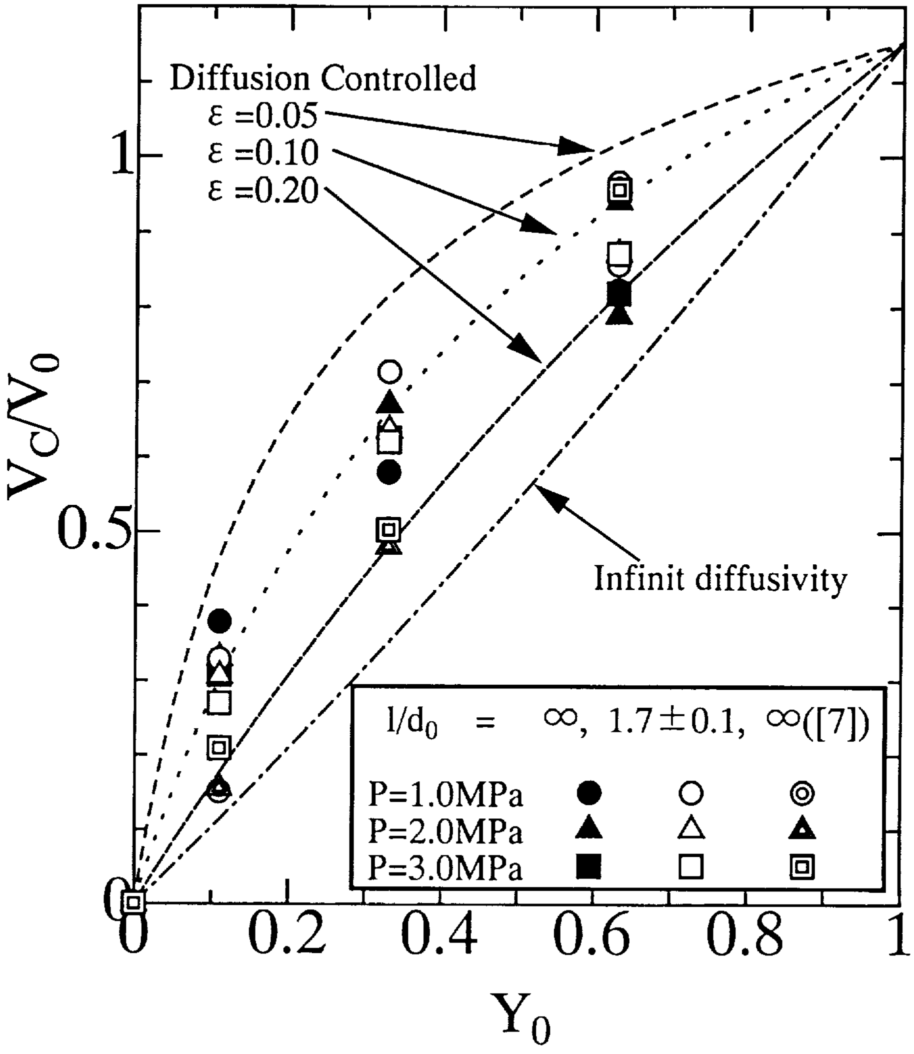

Fig. 16 Dependence of the critical droplet volume fraction, V_C/V_0, at different ambient pressures on the initial hexadecane mass fraction, Y_0.

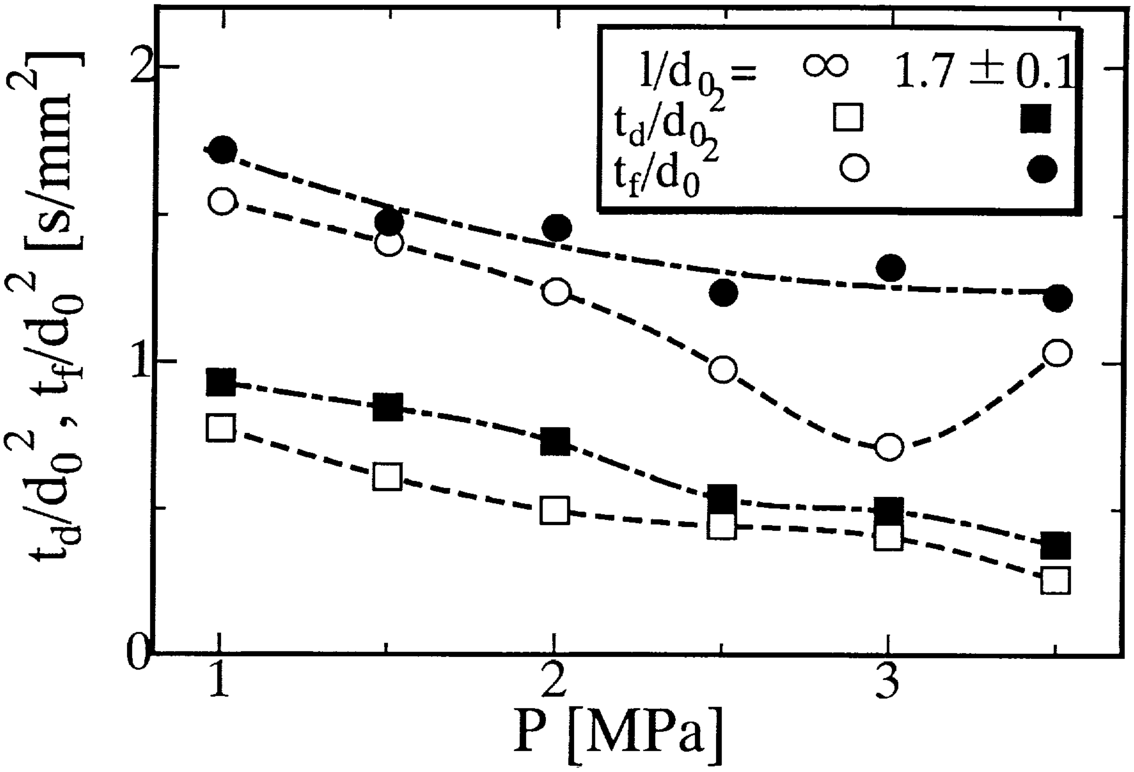

Fig. 17 Dependence of droplet lifetime and flame lifetime on ambient pressure for single droplet and droplet pairs (l/d_0=1.7±0.1).

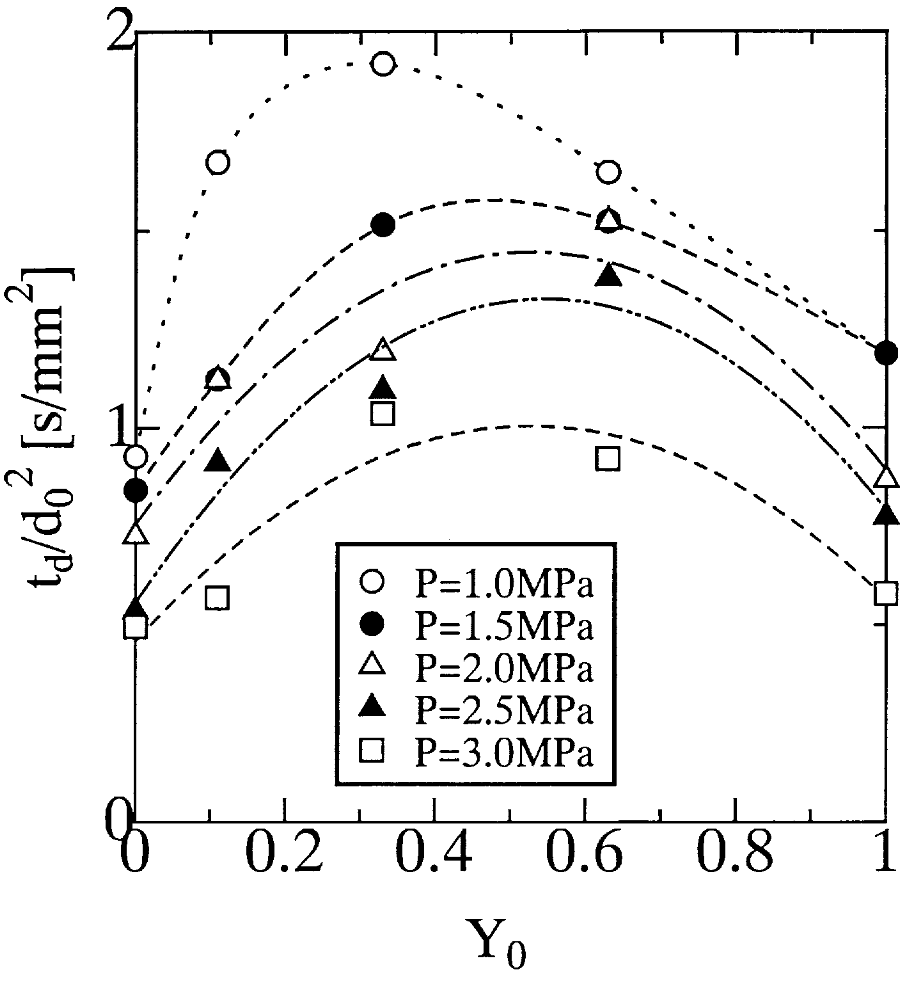

Fig. 18 Dependence of the droplet lifetime of droplet pairs (l/d_0=1.7±0.1) at different ambient pressures on the intial hexadecane mass fraction, Y_0.

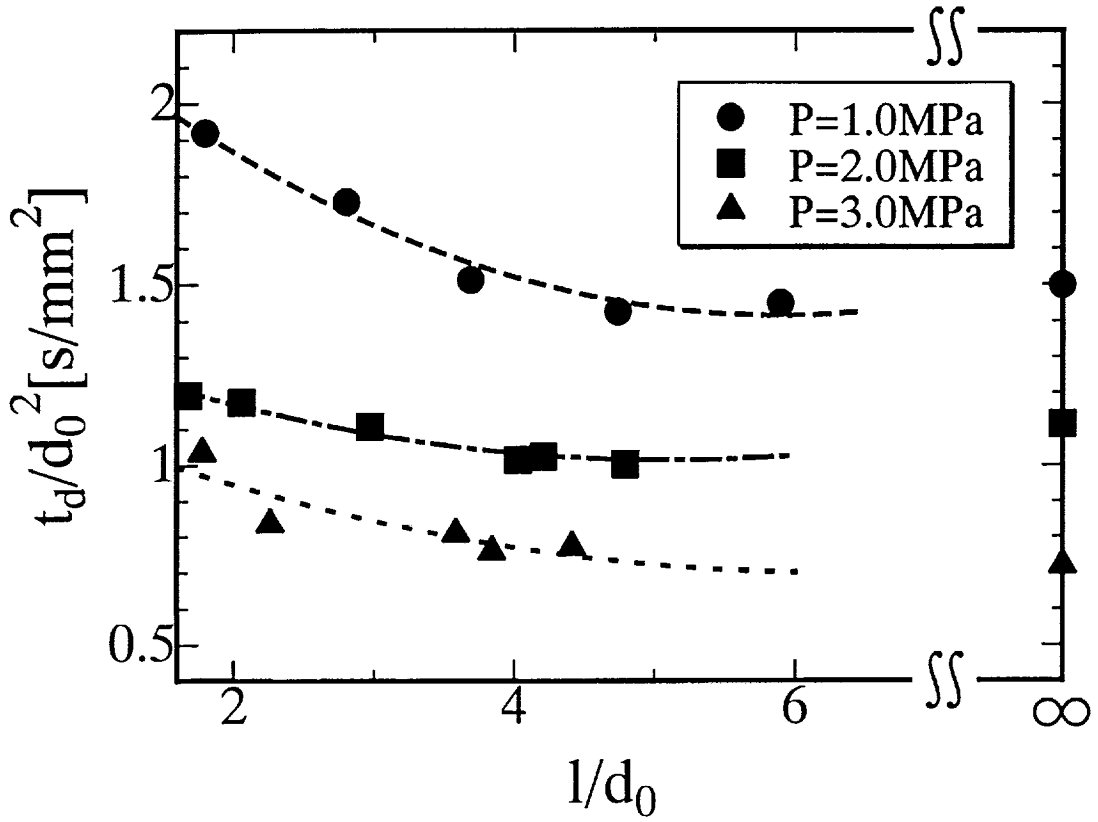

Fig. 19 Dependence of the droplet lifetime for droplet pairs (Y_0=0.33) at different pressures on the initial separation distance (l/d_0).

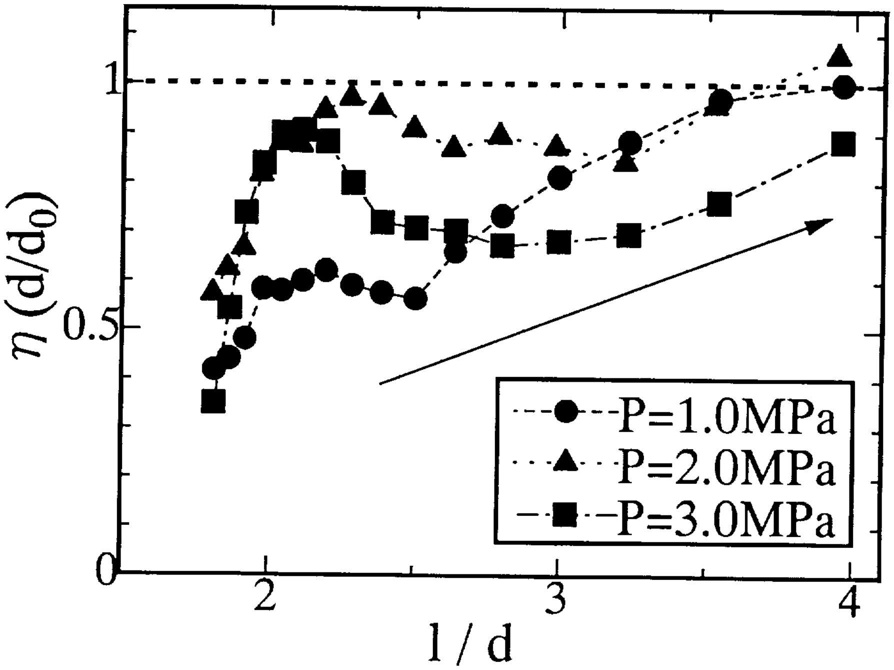

Fig. 20. Dependence of the burning rate correction parameter , $\eta(d/d_0)$, on the instantaneous separation distance, l/d, for three different pressures (Y_0=0) .

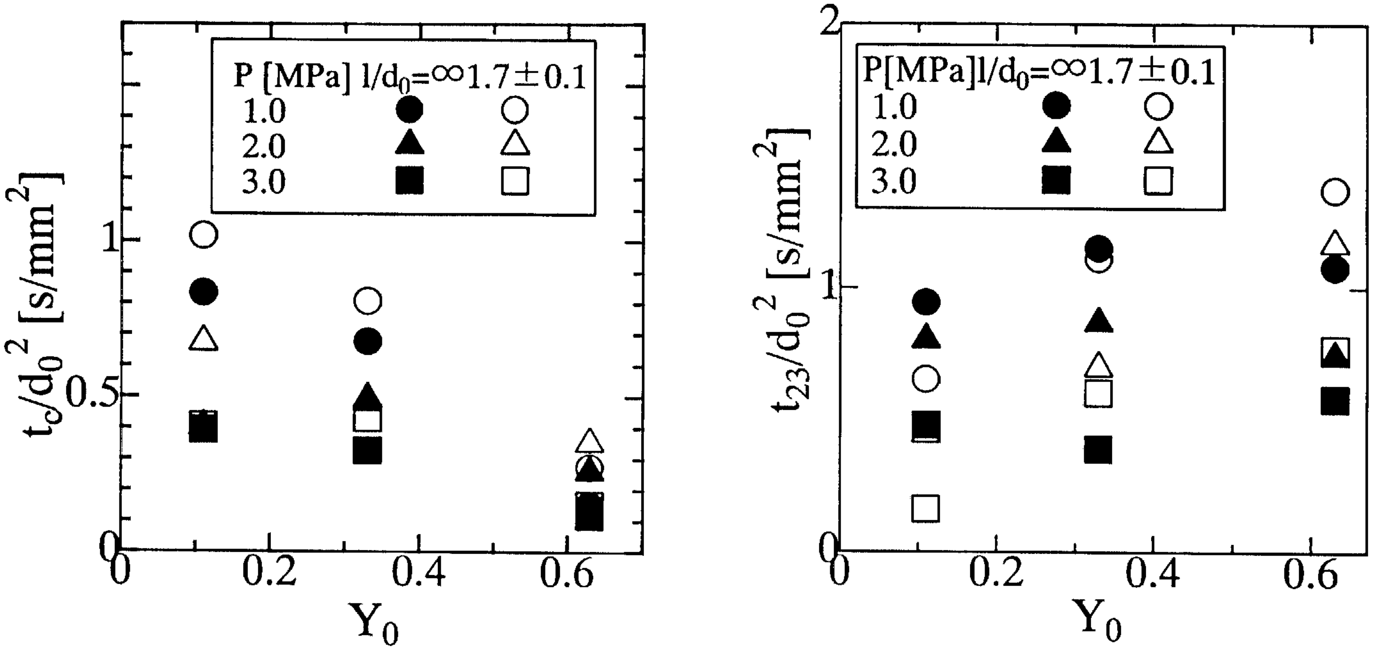

(a) the transition time (t_c/d_0^2)

(b) the second heat-up time (t_{23}/d_0^2)

Fig. 21. Dependence of the transition time, t_c/d_0^2, and the second heat-up time, t_{23}/d_0^2, on initial hexadecane mass fraction, Y_0 ((a) the transition time , (b) the second heat-up time).

Ignition and Subsequent Transition to Flame Spread in Microgravity

Kenichi Ito, Osamu Fujita and Masao Kikuchi
Hokkaido University, Sapporo, 060 Japan

Toshisuke Hirano, Tokyo University, Tokyo, 113 Japan

Takashi Kashiwagi,
National Institute for Standards and Technology, Gaithersburg, MD 20899, USA

and

Sandra L. Olson, NASA Glenn Research Center, Cleveland, OH 44135 USA

1. Introduction

The ignition of solid materials and the subsequent transition to flame spread over the solid material are very important subjects not only from the view of fire safety but also from the view of the solid fuel utilization in industry or waste combustion by incineration. Since these phenomena are strongly affected by the mass and heat transfer near the ignition point or flame front, it is fairly significant to make clear the effect of the external flow on the phenomena. However, it is difficult to know the simple effect of external flow because in normal gravity, the buoyancy effect can overwhelm the external forced flow, especially when the approaching flow rate is small. This complexity is much reduced in microgravity. Hence, the microgravity environment provides a simpler, and in some ways, better environment to conduct investigations geared towards elucidating complex combustion phenomena such as in solid combustion.

In the present research, therefore, solid material combustion has been investigated under microgravity to gain a better understanding of the fundamentals of solid material combustion.

This research has been performed by an international collaboration research between NEDO and NASA and is composed of two different parts. The first part is solid thin sheet combustion in microgravity mainly done at JAMIC (Japan Microgravity Center). This research has been already done for four years. The second part is the combustion of preheated thick solid material to be done by NASA's parabolic flight airplane. Originally, these experiments should have been performed in the early period of FY1997. However, they were postponed until the late period of FY1997 or early period of FY1998 due to a diplomatic agreement problem. The renewed schedule has again been postponed due to the same problem. Therefore, the second part of the research program is still on preparation stage except for what was achievable in normal gravity or JAMIC. For both parts of the program, the solid material is set in a uniform approaching flow to determine the effect of the flow on the ignition and flame spread.

In the following sections, the status of this collaborative research will be reported. The first half will focus mainly on the results of the solid sheet combustion experiments. The latter half will report on the preliminary experiments and preparation status of the parabolic flight experiments for the preheated thick solid material combustion, which is expected to be done in the near future.

2. Experimental Method and Apparatus (for Solid Sheet Combustion)

2.1 Experimental setup

In this section the experimental apparatus and techniques used for solid sheet combustion for JAMIC experiments are described.

Figure 2.1 shows the schematic description of the experimental setup (front view). The setup is composed of the RITSI combustion module at right hand side, an image recording system at left hand side, and the control system in the center. Figure2.2 shows the direct picture of the experimental setup taken from the combustion module side. In this picture the RITSI combustion module can be seen at nearer side and cameras at further side. Above the combustion module is a mirror through which a top parallel view of the sample can be taken by 35mm still camera.

Figure 2.3 shows (a) a schematic description of the combustion module and (b) a direct picture of the module installed with the test specimen. This combustion module, called RITSI (Radiative Ignition and Transition to Spread Investigation) module, was originally developed as an engineering model for a Glovebox Experiment to be conducted aboard the Space Shuttle flights. A suction fan is installed at the left end of the module to induce a flow through the test section. The flow channel is designed to achieve uniform flow at the test section as much as possible. The flow velocity is controlled by a supplied voltage to the fan based on the calibration curve shown in Fig.2.4. The sample sheet is set at the center of the flow channel in the module with the holder shown in Fig.2.5. At the front of the module, a clear glass is fixed to allow observation of the flame propagation. In figure 2.3(b), a circular optical filter is also seen. In the current research, however, only a plane flat clear glass is used without this filter. At the top of the module, a removable viewing window is used to install the samples and to observe the paper sheet combustion from the top. Behind this flow channel is room for a control circuit and 60 Watt tungsten-halogen lamp to radiatively ignite the paper sheet (the control block in the Fig.2.3(a)). The dimensions of this combustion module are fairly compact:: 300mm(W)× 180mm(D)× 135mm(H). This module is small enough to occupy 1/4 the total rack volume of JAMIC payload space even with an image recording system installed.

Since the oxygen concentration is a very important parameter in this experiment, the RITSI module and the other parts are put inside an large air-tight chamber, which is shown in Figure 2.6, to control surrounding oxygen concentration (about 90 L volume used as a reservoir).

Table 3.1 Experimental conditions examined in March 1995

O2 Concentration %	Configuration of test pieces	Ignition method	Flow velocity Va cm/s	Experimental run No.
21	2D	Wire	2.0	JAMIC1-1
			5.0	JAMIC1-10
	3D	Lamp + Wire	2.0	JAMIC1-11
			5.0	JAMIC1-14
35	2D	Wire	0.0	JAMIC1-6
			2.0	JAMIC1-8
			5.0	JAMIC1-3
	2D+Free Edge	Wire	2.0	JAMIC1-12
50	2D	Wire	0.0	JAMIC1-5
			2.0	JAMIC1-13
	3D	Lamp	0.0	JAMIC1-7
			2.0	JAMIC1-2
			2.0	JAMIC1-9
			5.0	JAMIC1-4
	3D+Free Edge	Lamp	2.0	JAMIC1-15

Table 3.2 Experimental conditions examined in March 1996

O2 Concentration %	Configuration of test pieces	Ignition method	Flow Velocity Va cm/s	Test piece material	Experimental run No.
21	3D(IR)	Lamp	10	Paper	JAMIC2-12
	3D		10	Paper	JAMIC2-20
35	2D	Wire	10	Paper	JAMIC2-6
	3D	Lamp	0	Paper	JAMIC2-5
	3D		1	Paper	JAMIC2-10
	3D(IR)		2	Paper	JAMIC2-11
	3D		2	Paper	JAMIC2-16
	3D		5	Paper	JAMIC2-19
	3D		10	Paper	JAMIC2-7
	3D(IR)		10	Paper	JAMIC2-13
	3D		0	Polyethylene	JAMIC2-9
	3D		0	Polyethylene	JAMIC2-15
	3D		2	Polyethylene	JAMIC2-18
	3D		5	Polyethylene	JAMIC2-17
	3D		10	Polyethylene	JAMIC2-14
50	2D	Wire	0	Paper	JAMIC2-2
	2D		5	Paper	JAMIC2-8
	2D		10	Paper	JAMIC2-4
	3D	Lamp	0	Paper	JAMIC2-1
	3D		10	Paper	JAMIC2-3

Table 3.3 Experimental conditions examined in March 1997

O2 Concentration %	Configuration of test pieces	Ignition method	Flow Velocity Va cm/s	Test piece material	Experimental run No.
35	2D	Wire	1	Paper	JAMIC3-10
	2D		5	Paper	JAMIC3-2
	2D		10	Paper	JAMIC3-4
	3D	Lamp	0	Paper	JAMIC3-8
	3D		5	Paper	JAMIC3-1
	3D		10	Paper	JAMIC3-5
	3D		2	NIST Paper 0.83	JAMIC3-12
	3D		2	NIST Paper 0.83	JAMIC3-13
	3D		5	NIST Paper 0.83	JAMIC3-15
	3D		2	NIST Paper 1.09	JAMIC3-9
	3D		2	NIST Paper 2.0	JAMIC3-11
	3D		5	NIST Paper 2.0	JAMIC3-3
	3D		2	NIST Paper 2.75	JAMIC3-14
50	2D	Wire	10	Paper	JAMIC3-6
	3D	Lamp	10	Paper	JAMIC3-7

3. Brief description of the research by the end of FY 1996.

3.1 Experimental conditions and measurement method

The experimental parameters selected in the research are oxygen concentration, flow velocity, V_a, configuration of the test piece and ignition method. In this experiments a total of 15 runs were conducted in Mar.1995, 20 runs were conducted in Mar.1996, and 15 runs were conducted in Mar.1997. The experimental conditions set for each run are listed in Table 3.1, 3.2, and 3.3 respectively.

Oxygen concentration and flow velocity were varied within the range of 21-50% and 0-10cm/s, respectively. In the tables, the configurations of paper sheet are designated as 2D, 3D, 2D+Free Edge and 3D+Free Edge. The 2D geometry corresponds to the case when paper is ignited two-dimensionally by a long wire fitted across the width of the paper sheet. When the paper is ignited by the radiation from the tungsten-halogen lamp, the flame propagates circularly and this is called a 3D geometry. For 2D and 3D geometries, the paper sheets were attached to the paper holder as was shown in Fig.2.5, without a free edge. In a few experiments (JAMIC 1-12 and 1-15), paper with a width less than that of the paper holder was used to provide a free edge. These conditions are denoted as 2D+Free Edge for a 2D wire ignition or 3D +Free Edge for a3D radiative ignition.

For low oxygen concentration cases (JAMIC 1-11 and 1-14) where conditions are maginal for ignition, the wire and lamp heater were used simultaneously for ignition.

During the March 1996 experiments, five experiments were conducted using a polyethylene film sheet as the fuel. The polyethylene combustion experiments were all carried out using only the 3D radiative ignition. To obtain a surface temperature distribution, an IR camera was used during three tests, denoted as 3D(IR).

Also, during the March 1997 experiments, seven tests were conducted with 4 different paper sheets with varying area density. The various area density sheets were made for NIST, and have area densities of 26.8, 35.2, 64.5, and 88.7 g/m_2 respectively. The number after "NIST paper" in the tables indicates the mass of each paper sheet per 310 cm_2.

The last column of each table shows the designation of the experimental runs. This numbering refers to the order of microgravity experiments performed at JAMIC in the first ,second, and third year respectively.

3.2 Imaging the flame spreading

The transition processes from ignition to flame spread were investigated by recording video and 35mm still camera images during the experiments. The surface view of the flame spreading over the charring material was recorded by video and an edge view of the flame shape was recorded using very sensitive film in the still camera.

The nominal fuel sample is a piece of ashless filter paper which has a area density of 80 g/m_2 and a width of 50 mm (for 2D geometry) or 85mm (for the 3D geometry). A 1 cm by 1 cm grid is marked on each sample surface as a scale reference.

A typical flame spread image for a 2D ignition is shown in Fig.3.1. This image was taken under the conditions of O_2 = 35% and V_a = 5cm/s, JAMIC1-3. Ignition was carried out at the center of the sample using a Kanthal wire. Imposed forced flow is from right to left in the image. Flame spreads primarily upstream, although some downstream fuel pyrolysis is also observed, as seen in Fig.3.1(a). The upstream spread rate is much larger than that of downstream according to the width of charred region. From the edge view shown in Fig.3.1(b), it is clear that the upstream flame front is anchoring to the paper sheet while the downstream flame tail is lifted off from the surface of the fuel sheet.

Figure 3.2 shows an example of 3D radiative ignition geometry. The experimental conditions are O_2 = 35% and V_a = 5cm/s, JAMIC2-19. In this case flame is spreading upstream from the central ignition point with a U-shaped flame. Upstream flame spread seems to be faster than that of downstream as seen in the two dimensional case. At the flame front two different color zones are observed in the front view. These are corresponding to the blue premixed region and the luminous yellow sooting fuel rich flame zone, respectively.

As shown in the figures, the flame front is quite smooth and it is easy to discern the leading edge position and char front positions. These images are used to track the flame and char front positions as a function of time to measure the flame spread rate to be discussed in the next chapter. Figure 3.3 shows the flame (char) front position as a function of time for different flow velocities at O_2=35% with two dimensional wire ignition. The slope of the line indicates the flame propagation speeds. For the downstream flame, the charred position is shown as negative values to differentiate upstream and downstream flame spread.

The upstream flame propagation rate is affected by the forced flow velocity while the downstream propagation is not very strongly affected by the flow velocity. The reason for this tendency will be discussed in the next chapter by comparing the flame spread rates for different flow velocities.

In addition to image data, temperature histories at the ignition point in the center, 2cm upstream and 2cm downstream were also recorded. Figure 3.4 is one of the typical example taken under O_2 = 35% and V_a = 5cm/s, JAMIC 2-19. Naturally, the temperature at the ignition center rises at first due to wire heating, and once ignition occurs (@4sec), the downstream temperature starts to rise due to convective heat transfer of the hot ignition gases past the downstream location. The upstream temperature remains cool until the flame approaches, and then the temperature exceeds the downstream temperature as the flame moves directly over the location. This phenomenon is explained by the effect of the forced flow, where the upstream region initially remains at the ambient temperature of the flow, but once the flame reaches the 2cm upstream it becomes higher than that of downstream because the flame front is anchored close to the fuel surface at the upstream edge with fresh oxygen supply to the flame. The downstream flame tail, which is bathed in a stream of hot combustion product gases, is stabilized much further from the fuel surface and thus provides less heat flux to the surface.

As described here the ignition and flame spread data including temperature history were successfully obtained in the experiments.

4. Research progress by the end of FY1998

- Analysis of the experimental results taken by the end of FY 1997-

4.1 Data analysis and discussion

4.1.1 flame spread phenomena

Two dimensional case

In this chapter the effect of the selected experimental parameters on flame spreading and ignition are discussed based on the experimental data obtained by the end of FY1997.

Figure 4.1 shows a comparison of the edge view of the two dimensionally spreading flame for various flow velocities. Those pictures are taken under the conditions of O_2 = 35% at 4.5s after ignition. The flame becomes brighter and longer with increasing flow velocity, which implies the oxygen supply to combustion region enhances the combustion intensity. In the quiescent case,(a), flame shows a symmetrical shape and both the upstream and downstream flame fronts anchor to the surface of the paper sheet, though the flame luminosity is low. At V_a = 2cm/s flame is still quite dim, especially the downstream flame tail which is fairly dark and lifts off from the surface. At flow velocities of 5 or 10cm/s the flame develops a luminous flame body with a blue premixed leading edge region ahead of the luminous flame. For all convective flow cases the downstream flame never attaches to the surface of the paper sheet as seen in the case of V_a = 2cm/s. In the downstream region, the combustion gases produced in the upstream flame cover the sample and the oxygen supply to the sample surface is quite limited. As a result, it becomes difficult to sustain the combustion in the vicinity of the downstream sample surface. This effect is expected to lead to the lower flame spread rates in the downstream direction.

Figure 4.2 shows the flame spread rate as a function of flow velocity for various oxygen concentrations. In this figure the data for upstream and downstream are revealed simultaneously. The upstream spread rate increases with increase in approaching flow. The downstream flame spread rate is much smaller than that of upstream. In most conditions the downstream flame looked as if spreading stopped. This is due to the reason discussed in the explanation of Fig.4.1.

The effect of oxygen concentration is also observed. The flame spread rate increases strongly with increasing oxygen concentration.

Three dimensional case

Figure 4.3 shows the comparison of flame shape for the three dimensional case at various flow velocities. These pictures are taken from an oblique angle relative to the fuel surface. When the flow velocity is low the flame color is faint blue. In these cases the flame is so dim that it is hard to see in the picture at V_a = 0 or 2cm/s. At V_a = 5 or 10cm/s the flames begin sooting as was seen in the two dimensional case. In the case of V_a = 10cm/s the spread rate is so high that the flame almost covers the sample sheet even at only 5s after ignition.

Figure 4.4 shows the flame spread rate for three dimensional case as a function of flow velocity. Flame spread rate increases with increasing flow velocity. In this case, The upstream spread rate increases with increasing approaching flow as was shown in the two dimensional case. The increase in flame spread rate with oxygen concentration is much larger between O_2 = 21 and 35% than between O_2 = 35 and 50%.

The effect of flame configuration

Figures 4.5 and 4.6 show the upstream flame spread rate and char front spread rate respectively. In these figures, the data for both two and three dimensional flame configuration case are shown for comparison. Although the difference between the two dimensional configuration and the three dimensional configuration in 50% oxygen is within the scatter of data, the results in 35% oxygen indicate that both flame spread rate and char front spread rate in the three dimensional configuration are slightly faster than in two dimensional configuration.

The effect of area density

Figure 4.7 shows the flame spread rate for four kinds of paper samples which have different area densities. In all these tests, the tunsten-halogen lamp was employed to ignite the paper sheet. Therefore, all data shown in figure 4.7 are in the 3D geometry. Oxygen concentration is 35% in all tests. Upstream flame spread rate decreases with increasing area density of the paper sample, although the decrease in flame spread rate appears to slow with increasing area density.

Discussion on flame spread phenomena

In the previous chapters some characteristic results on the effects of flow velocity, oxygen concentration, flame configuration, and area density on flame spread rate have been revealed. The results are summarized as follows;

(1) Flame spread rate increased with increasing flow velocity,
(2) Flame spread rate increased with increasing oxygen concentration,
(3) Upstream spread rate was much higher than that of the downstream,
(4) Both upstream flame spread rate and char front spread rate in the three dimensional configuration were slightly faster than in two dimensional configuration (for sufficiently low ambient oxygen concentration), and
(5) Flame spread rate decreased with increase in area density of paper sample.

Generally, there are three types of flame spread phenomena over thin solid materials. The first type is heat conduction controlled flame spread 1). The second type is Damkohler number controlled flame spread, where finite chemical reactions are too slow relative to the flow residence times 2). The third type is oxygen supply controlled flame spread 3). The most common flame spread is the heat conduction controlled type, but the condition dealt in this research is assumed to be the third type because the approaching flow velocity is zero or quite slow. In the normal gravity it is difficult to observe such an oxygen supply controlled region of flame spread because an effect of natural convection provides significant flow velocities. If the conditions for these experiments are of the third type, the characteristic phenomena summarized above are easy to explain as follows.

The results for (1) and (2) are due to the direct increase in oxygen supply, that is, increased flow velocity and oxygen concentration make the oxygen supply to the combustion region increase. If the flame spread were heat conduction controlled, the spread rate would not increase with increasing flow velocity even when the oxygen supply towards combustion region increase.

The results for (3) are due to the consumption of oxygen at the upstream combustion region which results in insufficient oxygen supply to the downstream region. For limited oxygen supply, the upstream flame consumes most of the available oxygen in the incoming flow. This phenomena has been demonstrated by the numerical calculation 4).

The results for (4) are due to a larger oxygen supply at the curved flame front. In the regime where oxygen supply is the critical rate-controlling process, a curved front has a larger area for incoming oxygen to reach. Also, this should be more clearly seen in the air case (21% O_2), but unfortunately 10 seconds is insufficient to obtain enough data for the comparison. A more detailed discussion theoretical predictions of this curvature effect is found in section 4.2.

The results for (5)I are due to the transition from thermally thin condition to thermally thick condition. According to the theoretical results 1), for a thermally thin condition, the flame spread rate over solid fuel is inversely proportional to the area density of solid fuel, and for a thermally thick condition, the flame spread rate is independent of the area density. The trend of flame spread rate shown in figure 4.7 appears to correspond to a transition thickness between thermally thin and thermally thick.

4.1.2 Comparison of ignition delay

Energy supply to ignition source

It is necessary to define the energy supply to the igniter before discussing the ignition delay of solid materials. Figure 4.8 shows a comparison of the input energy as a function of time for the wire heater used for 2-D ignition and to the tungsten-halogen lamp used for 3-D ignition. Ignition starts at the moment of capsule drop. For the wire heater the input energy reaches a given value right after ignition start and is kept constant. For the lamp heater it takes a few seconds to reach a set value. The ignition delays discussed below is including this start up time for the lamp heater.

The effect of oxygen concentration

Figure 4.9 shows the ignition delay as a function of surrounding oxygen concentration. Figure 4.9(a) and (b) shows the results of the wire ignition (two-dimensional case) and halogen lamp ignition (three-dimensional case), respectively. For both cases, ignition delay decreased with increasing oxygen concentration.

The effect of approaching flow velocity

Figure 4.10 shows the ignition delay as a function of flow velocity. The effect of the velocity is not significant, unlike that of oxygen concentration.

Though the ignition delay of wire ignition is shorter than that with lamp heater as seen in Fig.4.9 and 4.10, it is difficult to simply compare the two because the distance from the heater to the paper surface is difficult to keep constant. However, the dependency of ignition delay on oxygen concentration and flow velocity is common for both ignition method.

The effect of area density

Figure 4.11 shows the ignition delay as a function of the area density of samples. Ignition delay increased with increase in area density. A discussion of this dependency is found in the next section.

Discussion on the ignition delay

The dependency of ignition delay on oxygen concentration was more obvious than that on external flow velocity. One of the possible ignition mechanisms is the gas phase ignition of degradation gas from the solid material right above the solid surface 5). With higher oxygen concentration gas phase reaction rate becomes higher, which results in shorter ignition delay.

The flow velocity should also influence the ignition delay through the prevention of the growth of a flame kernel, if the above mechanism is occurring. In reality, the ignition delay was only slightly affected by the flow velocity. This implies that the ignition occurs very close to the surface where the boundary layer flow velocity is a small fraction of the bulk flow velocity.

Lastly, the increased sample heat capacity due to increased area density will cause an increase in the ignition delay.

4.2 Numerical calculation

Three dimensional and two dimensional simulations of the transition from radiative ignition on paper sheet to flame spread in an imposed wind were performed in microgravity 6). The focus of this numerical calculation is to investigate the influence of flame geometry on the likelihood of transition from ignition to flame spread in near quenching conditions. The mathematical models, boundary conditions, calculation scheme and rate constants for the degradation and gas phase reaction necessary for numerical calculations are described in detail in the Ref.[4,7-9].

Figure 4.12 shows the upstream flame spread rate versus V . from 2D and 3D simulations in atmospheres of oxygen mass fraction, $Y_{o\infty}$, of 0.33 and 0.5. The trend of increasing spread rate with flow velocity followed by a relatively constant spread rate for larger flow velocity is consistent with experimental results shown previously. None of the flames in the $Y_{o\infty}$ = 0.5 case were quenched. Quenching does occur in both the 2D and 3D simulations when the ambient oxygen is lowered to $Y_{o\infty}$ = 0.33. The 2D case quenches at a larger V . value than the 3D case. These results imply that V . . ≈ 0.5 cm/s for the 3D flame and V_o ≈ 1 cm/s for the 2D flame are near the quenching limit due to insufficient oxygen supply. Next, 2D and 3D results for V . = 1cm/s will be compared in order to better understand why the 3D flame survives at smaller V ..

Figure 4.13(a) and (b) show centerline (y = 0) profiles (2D and 3D cases, respectively) of the net heat flux on the sample surface (q_s, black line), the conductive/convective heat flux (q_c, red lines), and the height at which the maximum temperature occurs (solid circles). Above the centerline profiles are color contours of the reaction rate, oxygen (black) and fuel(red)mass flux vectors, and velocity streamlines. These data are at time t = 1.5s for the V_∞ = 1cm/s case; the ambient wind flows from right to left. This time is chosen because it is after ignition and is characteristic of times up to t = 3.5s when the external radiant flux stops. The net surface heat flux in both the 3D($q_{s,3D}$) and 2D($q_{s,2D}$) simulations is triple peaked. The center peak is the symmetry point of the external flux and the center of the pyrolysis region. The $q_{s,3D}$ side peaks are significantly larger and closer to the center than in the 2D case. The same is true for the reaction rates. The maximum temperatures were found to be larger in the 2D case. However, the values of $h_{mx,3D}$ and $h_{mx,2D}$(the height of the maximum temperature) in figure 4.13 show that the $q_{s,3D}$ side peaks are larger than $q_{s,2D}$ because the maximum temperatures in the 3D case occur closer to the sample surface. The presence of smaller peak temperatures located closer to the sample surface and larger gas phase reaction rates suggest that the diffusion of oxygen to the flame in the centerline plane is stronger in the 3D case. If more oxygen is present near the sample surface due to diffusion, then fuel and oxygen will mix more fully and react at lower heights. It is clear from comparison of Figs. 4.13(a) and (b) that significantly more oxygen diffusion to the flame occurs in the 3D case. Oxygen mass flux vectors near and within the flame are perpendicular or even nearly anti-parallel to the streamlines.

Figure 4.14 shows the streamlines and mass flux vectors for both the oxygen and fuel in the x-y plane at a height of z = 2.5mm for the same external wind(V_∞ = 1 cm/s)and time (t = 1.5s)values used in Fig. 4.13. The upper and lower halves of the figure contain the fuel and oxygen mass flux vectors, respectively. Pyrolysis and expansion from gas phase reaction create an obstacle which the upstream originating flow must circumvent. As in Fig. 4.13(b), far from the flame the oxygen mass flux vectors and streamlines point in the same direction (convective flux dominates). Oxygen mass flux along the outer regions of the flame is toward the centerline plane. Near the center of the flame the oxygen mass flux vectors and streamline directions are opposite; the magnitude of the flux from the side is nearly equal to the centerline flux in the upstream part of the flame. Diffusion in the 2D case can only occur within the centerline plane. Thus, it is clear that the curvature in the x-y plane of the 3D flame allows more oxygen to diffuse to the center of the flame. The 3D flame is therefore less dependent on oxygen supply from an external wind and successfully undergoes transition to flame spread while the 2D flame is quenched.

As discussed above, it is likely that the increased diffusion of oxygen in the 3D flame caused the fuel to mix with oxygen at lower heights resulting in a flame which is closer to the sample surface. The 3D flame, therefore, required less oxygen supply from an external wind to undergo transition to flame spread.

4.3 JAMIC experiments in FY 1998.

The experiments in this year will be performed in the end of FY1998, March 1999. A total of 15 experimental runs are planned. A larger apparatus with more diagnostics will be used to obtain additional new diagnostic information on the combustion process over solid materials. A high resolution infrared camera will be used to record the surface temperature distribution during ignition and flame spread, and an infrared spectroscopic array will be used to obtain gas phase temperatures, CO_2 and H_2O concentrations, and soot volume fraction and soot temperatures.

5.Preheated thick solid material combustion experiments

(NASA parabolic flight experiments)

5.1 Experimental results relating to parabolic flight experiments

5.1.1 Description of the experiment

This research studies the ignition and subsequent transition to flame spread over solid materials in a microgravity environment. The experiments to be conducted during parabolic flight of NASA KC-135 should have been done in the early period of FY1997. However, it was postponed and not performed yet as described in the first section of this report.

For these parabolic flight experiments a relatively thick solid material (compared to that used in the previous section) is examined, which requires a longer time for flame to spread. During the parabolic flight experiments the effect of preheating the material, which is one of the most important factors to dominate flame spreading, will be investigated. To do these experiments, a wire composed of core metal wire and its insulation will be used. Preheating of the material is controlled by the electric current supplied to the core wire.

Some preliminary experiments for the parabolic flight experiments were conducted at JAMIC [10, 11]. In the preliminary experiments only quiescent environment was examined because of space constraints for the experimental equipment. The effect of external flow will be investigated in the parabolic flight experiments. In this chapter results of these preliminary quiescent experiments will be reported.

5.1.2 Experimental apparatus

The experimental apparatus used in this study is shown in Fig.5.1. The dimensions of the apparatus are 425 mm (D)× 870 mm (W)× 445 mm (H), which is suitable for installation into a

¼ of the drop capsule of JAMIC. It is composed of a combustion chamber, image recording system, and control system. The combustion chamber has a volume of 10.4L and it is a pressure vessel allowing internal pressures of 0 to 2 kg/cm $_2$. It has three optical windows to allow image recording from three different directions. For the image recording, Hi-8 Video cameras were used for direct imaging. For some experiments a 35mm still camera was also used. Because of the space limitation a gas supply system to give external flow could not be included in this setup.

Figure 5.2 shows how the sample wire was supported, with the relative positions of the igniter and wire tensioner. The sample wire was vertically mounted. One end of the wire is fixed to a pin at the top right. The other end of the wire is kept under tension by a spring and pulley at the bottom of the other post. The assembly shown in Fig.5.2 was installed inside the combustion chamber.

Both ends of the wire insulation were removed to allow direct contact between the inner wire and the pin or the pulley. The pin and pulley are made of metal and act as electrodes. A constant electric current supply is connected to the pin and the pulley to keep the wire temperature at a given value via a controlled electric current. For the microgravity experiments at JAMIC, the current was applied to the wire 30 seconds before the capsule dropped into microgravity.

The tested sample used in the preliminary experiments was PE (polyethylene) insulated wire, although ETFE (ethylene tetrafluoroethylene copolymer) insulated wire was also used during the early period of the preliminary experiments. The preheated temperature (on the surface of the inner wire) for these experiments was 373K(100 ℃) for PE insulated wire, although it was 398K (125 ℃) for ETFE insulated wire. Table 5.1 shows the basic dimensions of the sample wires, the inner wire diameter, d_w,thickness of wire insulation, δ, and the outer diameter of the sample, d_s. As described in the table, four wires of different insulation thickness and the same inner wire diameter were used to examine the effect of the insulation thickness. The PE material has the chemical formula of (C2H4)n.

Table 5.1 Tested sample wires

Sample name	#1	#2	#3	#4
Wire diameter d_w (mm)	0.5	0.5	0.5	0.5
Insulation thickness δ (mm)	0.075	0.15	0.3	0.5
Sample diameter d_s (mm)	0.65	0.8	1.1	1.5

Ignition was performed with a nichrome wire coil at the top of the sample as shown in Fig.5.2. The nichrome wire coil is surrounding the tested wire but without contact, so the radiative heat from the nichrome wire actually ignites the sample. The ignition timing for the microgravity experiments is set for flames to appear 2-3 seconds after microgravity starts.

To measure the temperature change during microgravity, one K type and five R type of 0.05mm diameter thermocouples were set 20～30mm below the igniter. The K type thermocouple closest to the sample is in contact with a surface of the insulation before combustion, and the other five R type thermocouples are set to measure the radial temperature distribution with at 1mm intervals.

5.1.3 Experimental results

Effect of O_2 concentration and initial sample temperature on flame spread rate

Flame spread rates were measured by the flame front motion in recorded video images. Figure 5.3 shows the flame spread rates in microgravity as a function of oxygen concentration. The results for an unheated wire in microgravity is shown as well.

The flame spread rate increases with oxygen concentration under all conditions. The effect of preheating with an electric current is also shown in Fig.5.3. The spread rate of the unheated wire in microgravity is smaller than that with preheating. Also, at O_2= 30%, the flame spread was not sustained for #4 wire in microgravity. The increasing flame temperature caused by increasing oxygen concentration resulted in a faster flame spread rate. Also, it is thought that an increase in initial insulation temperature led to reduction of the enthalpy necessary for insulation to pyrolyze and to produce a flammable gas, which consequently caused an increase in flame spread rate.

Effect of material dimension on flame spread rate

Figure 5.4 shows the effect of insulation thickness on flame spread rates in microgravity. There was no steady flame spread in microgravity for sample #4 with 30% oxygen concentration. Flame spread rate decreases with increasing insulation thickness, although the decrease in flame spread rate appears to be slowing with increasing insulation thickness. This trend is similar to the correlation between flame spread rate and area density of paper sheet as shown in figure 4.7. It is thought that the increase in insulation thickness led to the augmentation of the fuel heat capacity, which causing the decrease in flame spread rate.

Effect of dilution gas on flame spread rate

Figure 5.5 shows the effect of dilution gas on flame spread rates in microgravity. In this work, the effect of four kinds of dilution gas, He, N_2, Ar, and CO_2, were investigated in microgravity. Flame spread rate is the largest with He diluted atmosphere at relatively higher oxygen concentration. However, flame extinction occurred at 21% oxygen concentration with He diluted atmosphere, which is the highest oxygen concentration with regard to the four types of diluent employed in this study. It implies that the flammable range in microgravity is the narrowest with He diluted atmosphere.

One of the interesting result is that at 21% oxygen concentration, there occurred steady flame spread with CO_2 diluted atmosphere in microgravity, while there was no flame spread in normal gravity. According to these experimental results, CO_2 diluted atmosphere is the only case that flammable range is wider in microgravity compared with normal gravity.

The result of temperature measurement

Figure 5.6 shows the measured maximum gas phase temperature (flame temperature) in microgravity. The data with different dilution gas is shown in figure simultaneously. The sample is all #2, and initial temperature is 373K. Flame temperature increases with increase in oxygen concentration under all conditions. Also, flame temperature appears to be the highest with Ar diluted atmosphere, and lowest with He diluted atmosphere.

5.1.4 Some comments on parabolic flight experiments

The combustion of PE insulated wire was studied during these preliminary experiments. These experiments provided important information to be applied to the planned parabolic flight experiments.

A reliable ignition method is important in these experiments. By using nichrome wire coil, ignition was performed without fail. The effect of oxygen concentration and wire dimension were also briefly studied, and provided information to aid in the selection of the experimental conditions to be studied during the parabolic flight experiments.

Polyethylene insulated wire was chosen as the sample instead of ETFE insulated wire (which had been employed at the early period of the preliminary experiments) for the following reasons. First, the chemical composition and the degradation products of ETFE are relatively complicated to analyze in detail, although it is readily available as a commercial product. Second, the electric current required to heat the wire up to a given temperature was too high for ETFE insulated wire, since its inner wire was made of copper. To solve this problem, all PE insulated wire is made of nichrome, instead of copper.

These experiences are reflected in the planned parabolic flight experiments.

5.2 Status and schedule of the parabolic flight experiments

5.2.1 Status for parabolic flight experiments

In the parabolic flight, ignition and subsequent flame spread of preheated solid material will be investigated in low external flow field. It takes a longer time for flame spreading over thick material than that for thin sheet combustion described in the previous section. Therefore, the microgravity time given by the parabolic flight is needed to obtain useful data.

The sample material to be tested in the experiments is artificially made wire with polyethylene insulation. The core wire is nichrome wire to allow preheating of the insulation. This selection is based on the results of preliminary experiments conducted in normal gravity and JAMIC. The preparation status and experimental plan for the parabolic flight experiments is described in the following section.

5.2.2 Preparation status of the experiments

The progress of the parabolic flight experiments preparation is described as follows;

1996.3 First discussions of the parabolic flight experiments were held during JAMIC experiments in Kamisunagawa, Japan. The feasibility and usefulness of the parabolic fight for this collaboration research were discussed.

1996.7 Second discussions of the experiments were held. The expected experimental parameters, the basic concept of the experimental rig, and the required number of experimental runs were discussed.

1996.10 One of the Japan researchers for this project visited NASA LeRC and NIST to see the airplane for the experiments and the experimental rig to be modified to incorporate the planned experiments. Additional equipment from Japan to mount to the rig were proposed. A list of the remaining items was made, including the design and fabrication of the test samples, modification of the computer program for the rig control, and an additional required circuit for the experiments.

1996.10-1997.2 Exchanges of technical information necessary for the preparation of the experimental rig and additional equipment were made.

1997.3 Decisions were made for the experimental parameter range sduring the collaboration experiments at JAMIC. An example sample holder specialized for the parabolic flight experiments was provided by the NASA researcher.

1997.4-5 Final preparations for the parabolic flight experiments were made.

1997.5 Shipment was completed of the additional diagnostic equipment to NASA LeRC.

1997.6.9-22 Japanese researchers travel to NASA LeRC, Cleveland, USA. A final checkout of the facility was performed. Operational training for the parabolic flight experiments was conducted. A medical screening of the Japanese researchers was completed.

1997.6.23-27, 1997.7.7 -11 First campaign was postponed due to lack of an international diplomatic agreement.

1997.6.28-7.6 Normal gravity experiments were conducted.

1998.2-1998.4 The reassigned campaign was again postponed due to lack of an international diplomatic agreement.

5.2.3 Experimental parameters and expected data

Experimental parameters

Selected experimental parameters, so far, are as follows;

- Oxygen concentrations (18%, 21%, 35%)
- External flow velocity (0-200mm/s)
- Inert gas composition (N_2, Ar, CO_2, He)
- Sample material (PE insulated nichrome wire)
- Thickness of the insulation (0.075-0.5)

※ These are subject to change.

Expected data

In the parabolic flight experiments the following data are to be obtained. To get those data some additional equipment will be installed to the original NASA's experimental rig.

- flame contour
- Flame spread rate
- Temperature history
- OH radical emission
- Time resolved spectrum change of the flame
- electric current supplied to the core wire
- electric current supplied to the ignition wire
- external flow velocity

※ These are subject to change.

5.2.5 Integration plan of the equipment

Experimental rig

Figure 5.7(a) and (b) show the front and rear view of experimental rig to be employed on the parabolic flight. Also, the schematic description of the experimental rig is shown in figure 5.8. The basic structure of the rig is called TIGER (Transition from Ignition to flame Growth under External Radiation), designed and fabricated by NASA originally for the experiments for paper sheet combustion. The TIGER rig has a flow channel into which the desired composition gas can be supplied form external gas cylinders stored in a separate rack aboard the airplane. In these experiments the sample PE wire is placed in the flow channel instead of the paper sheet. To make the PE wire experiments possible, a modification of the sample holder was done. The front view of the sample holder to be used on the parabolic flight is shown in the Figure 5.9. The ignition system was also modified. In the original rig a CO_2 laser system was installed to do the ignition experiments. In this experiment, the CO_2 laser system was taken away and the nichrome wire ignition system was installed, which helps to save space for additional measuring instruments.

Additional equipments

The following equipment has been added to the original TIGER rig to obtain the desired data:

- Photomulti channel analyzer to give the time resolved spectrum change
- Image intensifier with CCD camera to visualize the OH radical distribution
- Constant current power source for preheating of the wire
- Handycam instead of the original CCD camera to save space

6.Summary for the whole collaborative research

In this report, the whole process of the collaborative research between NEDO and NASA has been described. The research subject was ignition and subsequent flame spread over solid materials.

Prior to this year (FY1998) JAMIC experiments of thin solid sheet combustion were carried out. Ignition and flame spread data were successfully obtained at JAMIC. The effects of external flow velocity and oxygen concentration on the thin paper sheet combustion were clarified. Infrared images of the burning paper surface have also been obtained. Additionally, data for polyethylene sheet combustion was obtained.

The status of the preheated thick solid material NASA KC-135 parabolic flight tests have also been described in this report. At this time, preliminary experiments for the parabolic flight experiments have been performed. Based on the results of these prelimnary experiments, the material to be tested was selected and the experimental parameters for the tests were also determined.

Finally, this international collaborative research has been accomplished successfully by utilizing each resources for microgravity research and has given a systematic data on the ignition of solid materials and the subsequent transition to flame spread over the solid material within a low air flow velocity. The experiments with longer microgravity time given by parabolic flight will contribute to the further understanding of this subject.

References

1. De Ris, J. N., 12th Symposium (International) on Combustion, The Combustion Institute, Pittsburgh, 1969, pp. 241-252.
2. Fernadez-Pello A.C. and Hirano T, (1983), Combust. Sci. Technol.: Vol.32, pp.1.
3. Olson, S. L., Combust. Sci. Technol. 76:233-249 (1991).
4. T. Kashiwagi, K. B. McGrattan, S. L. Olson, O. Fujita, M. Kikuchi and K. Ito, 26th Symposium (International) on Combustion, The Combustion Institute, Pittsburgh, 1996, pp. 1345-1352.
5. Nakamura, Y., Kushida, G., Yamashita, H. and Takeno, T., 33rd Symposium (Japanese Section) on Combustion(1995), pp.608-610 (in Japanese).
6. W. E. Mell and T. Kashiwagi, 27th Symposium (International) on Combustion, The Combustion Institute, Pittsburgh, 1998, (in print).
7. McGrattan, K. B, Kashiwagi, T., Baum, H. R., and Olson, S. L., Combustion and Flame, 106 (1996), 377-391.
8. Kashiwagi, T. and Nambu, H., Combustion and Flame, 88 : 345-368,(l992).
9. Kashiwagi, T., Mell, W. E., McGrattan, K. B., Baum, H. R., Olson, S. L., Fujita, O., Kikuchi, M., and Ito, K., 4th International Microgravity Combustion Workshop, 1997, pp.411-416.
10. Kikuchi, M., Fujita, O., Sato, A., Ito, K., and Sakuraya, T., 27th Symposium (International) on Combustion, The Combustion Institute, Pittsburgh, 1998, (in print).
11. Kikuchi, M., Fujita, O., Ito, K., and Sakuraya, T., Journal of the Japan Society of Microgravity Application, Vol.16, No.2, 1999 (in Japanese).

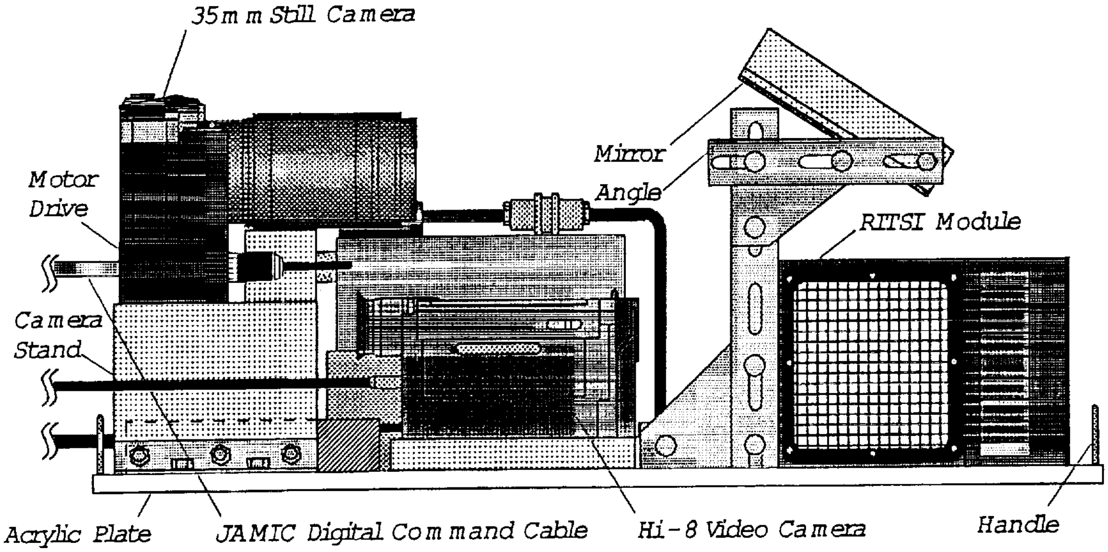

Fig. 2.1 Experimental set-up for drop experiments.

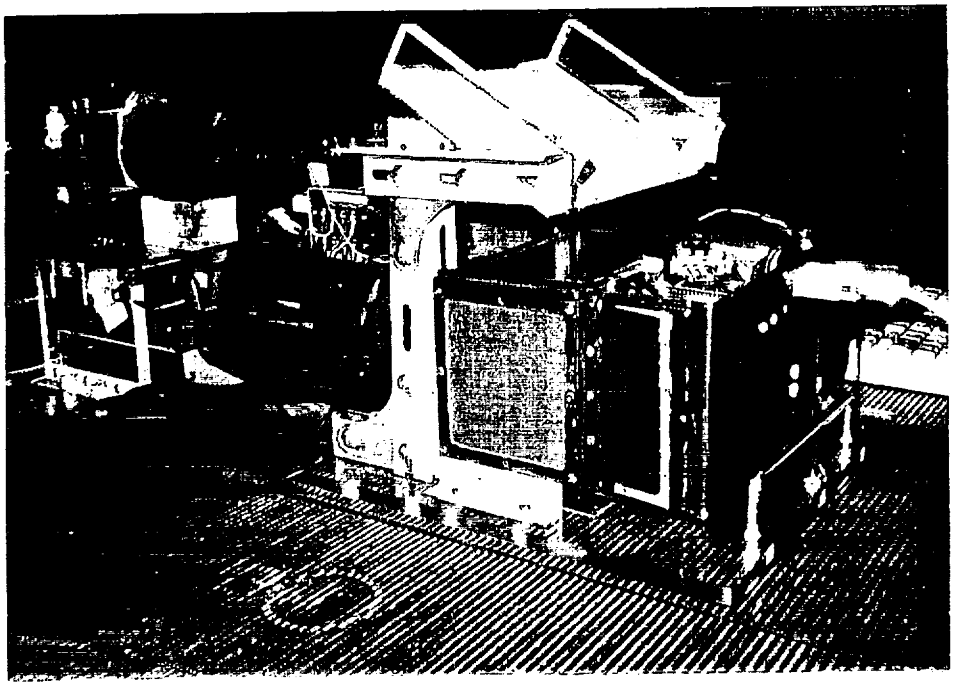

Fig. 2.2 Photograph of experimental set-up.

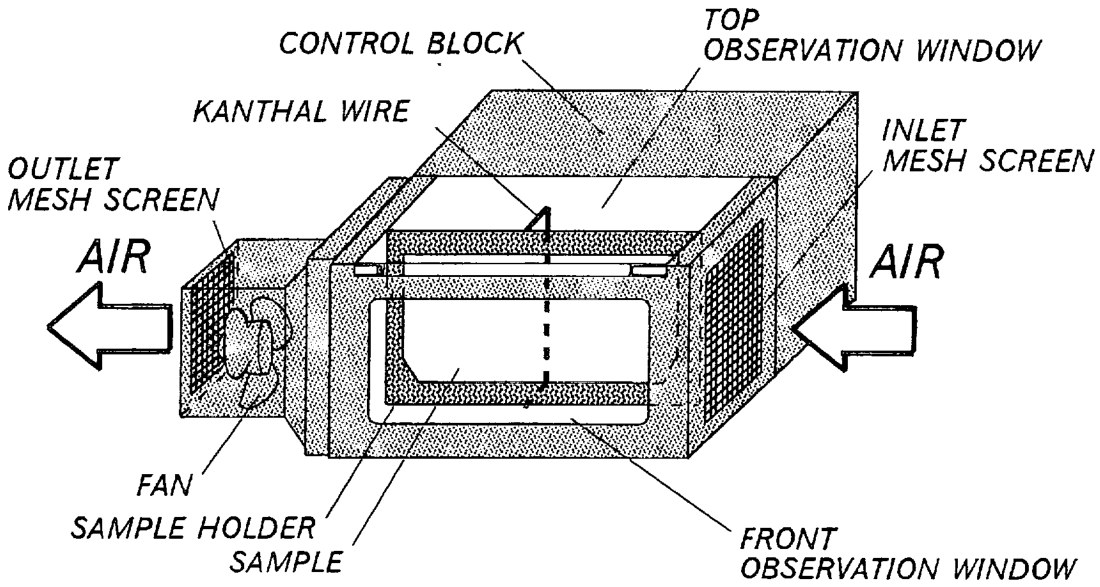

(a) Schematic description

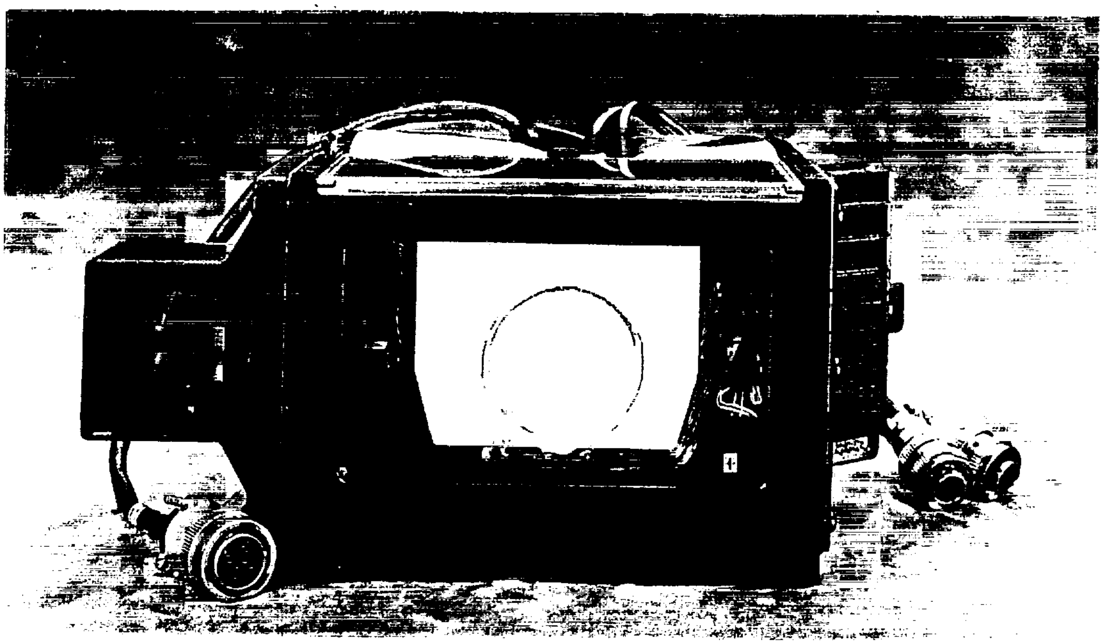

(b) Photograph of the combustion module

Fig.2.3 Combustion module for paper sheet flame spread.

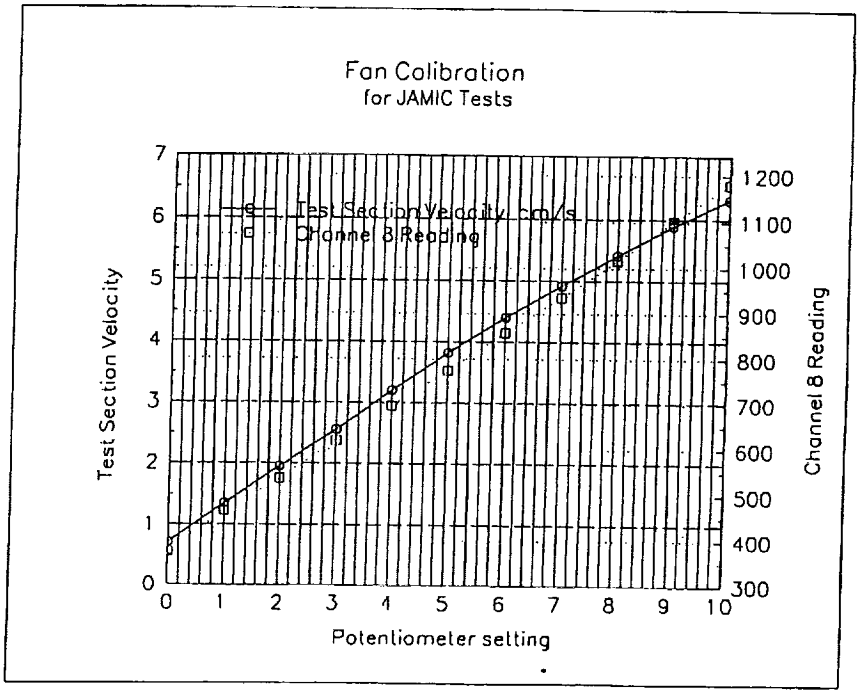

Fig.2.4 Calibration for test section velocity versus voltage supply to fan.

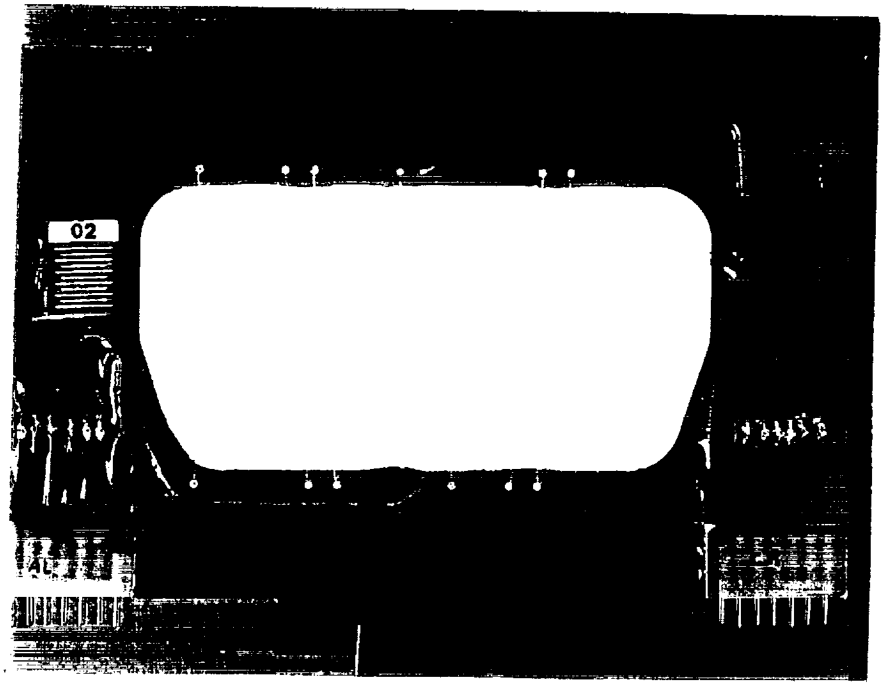

Fig.2.5 Test piece holder.

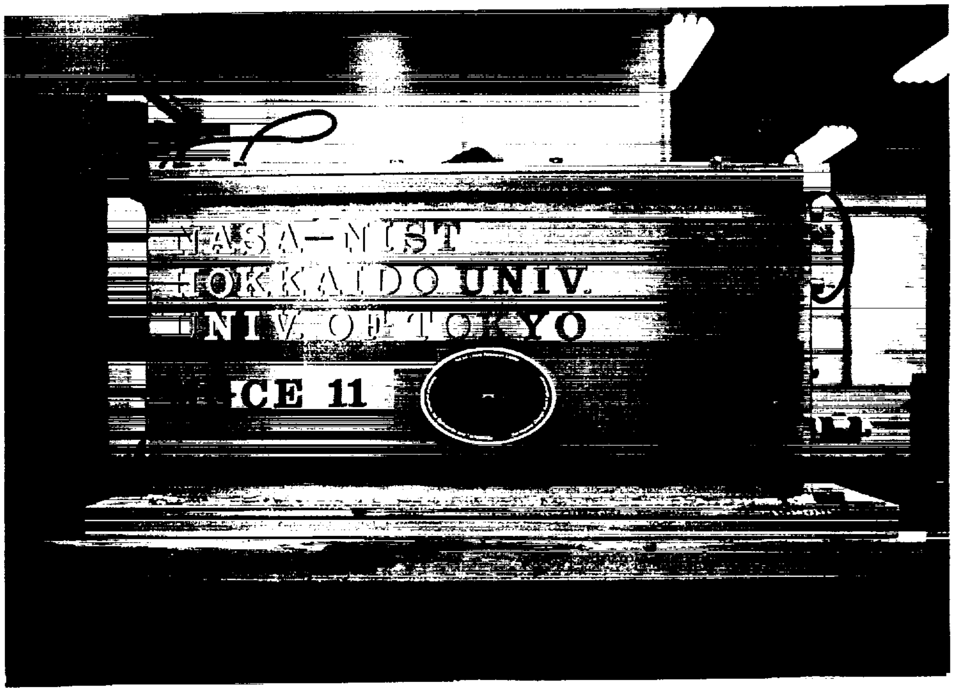

Fig. 2.6 Photograph of the air tight chamber.

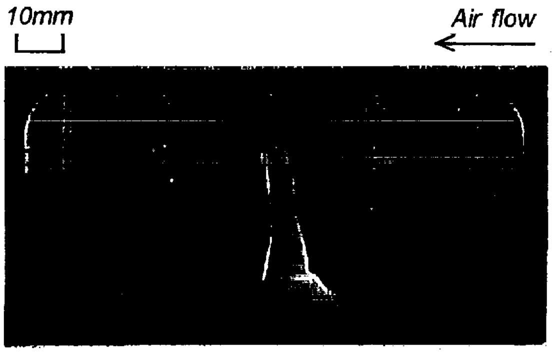

(a) Front view

(b) Top parallel view

Fig.3.1 Typical example of two-dimensional flame spread.

(O_2 =35%, V_a =5cm/s, 5s after ignition)

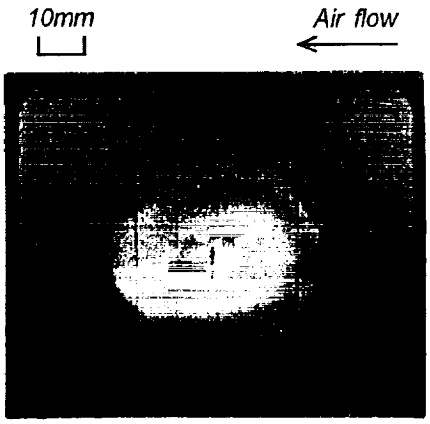

(a) Front view

(b) Top oblique view

Fig.3.2 Typical example of three-dimensional flame spread.

(O_2 =35%, V_a =5cm/s, 3.5s after ignition)

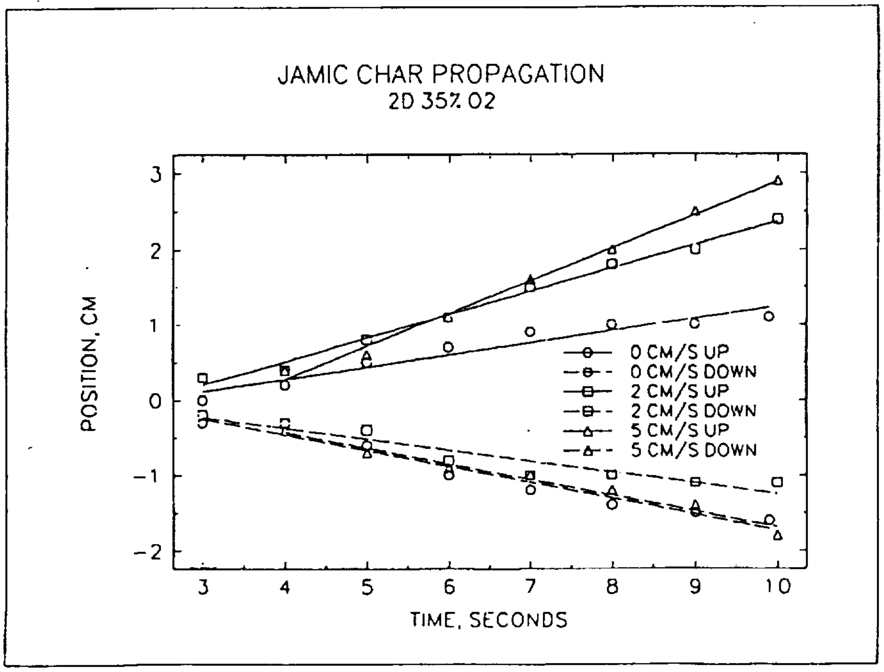

Fig.3.3 Flame front position as a function of time for 2D case.

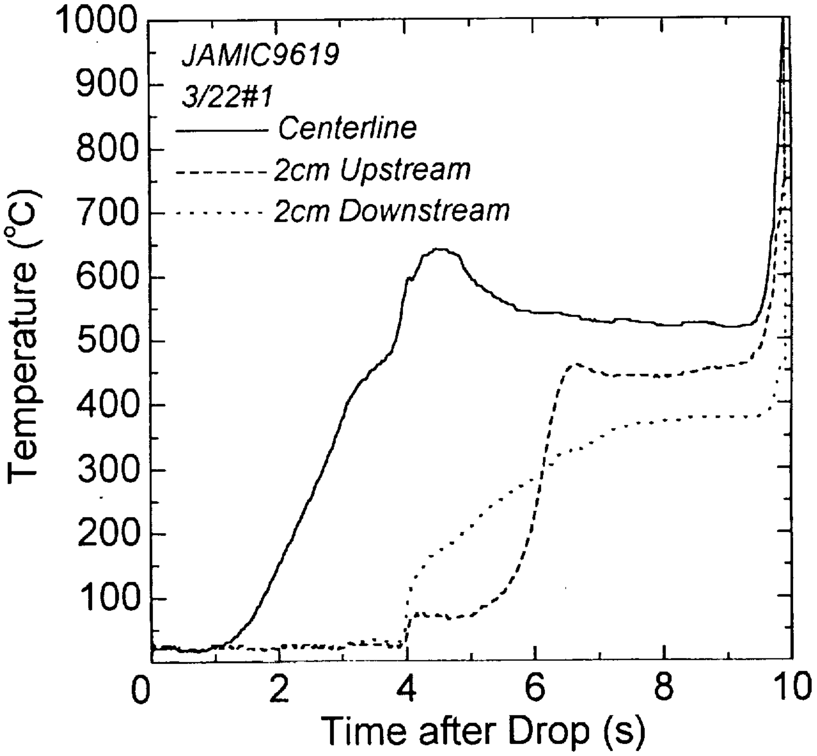

Fig.3.4 Example of temperature measurement.

(a) V_a =0 cm/s

(b) V_a =2 cm/s

(c) V_a =5 cm/s

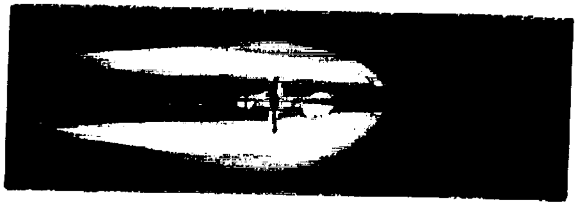

(d) V_a =10 cm/s

Fig.4.1 Comparison of flame shape for various air flow velocities (2D).
(O_2 =35%, 4.5s after ignition)

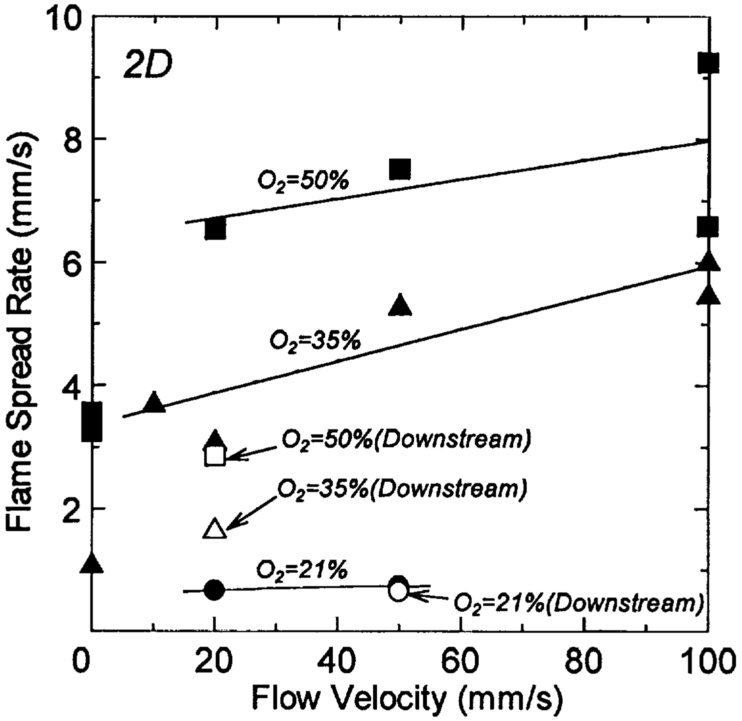

Fig. 4.2 Effect of air flow velocity on flame spread rate for two-dimensional spread case..

(a) V_a =0 cm/s

(b) V_a =2 cm/s

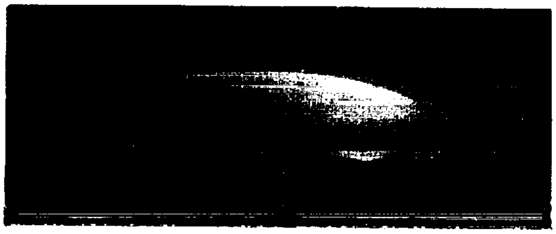

(c) V_a =5 cm/s

(d) V_a =10 cm/s

Fig.4.3 Comparison of flame shape for various air flow velocities (3D).
(O_2 =35%, 5s after ignition)

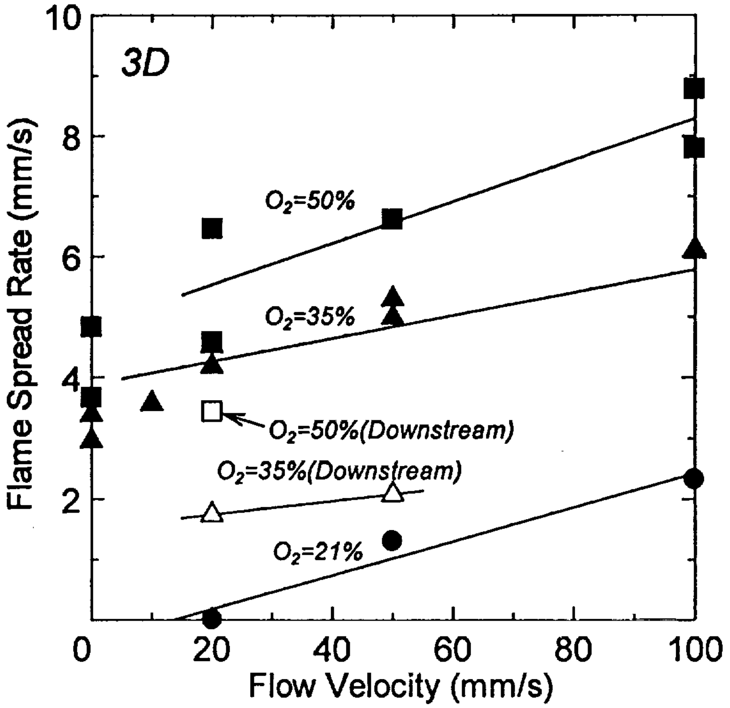

Fig. 4.4 Effect of air flow velocity on flame spread rate for three-dimensional spread case..

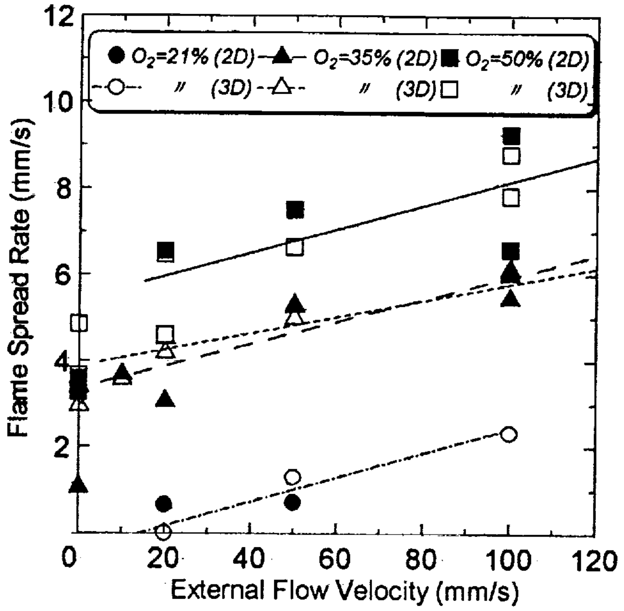

Fig. 4.5 Effect of air flow velocity on upstream flame spread rate both for two-dimensional and three-dimensional case.

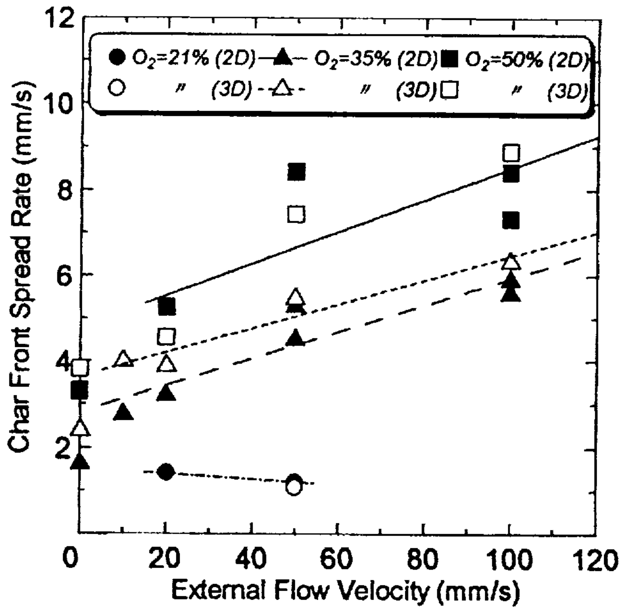

Fig. 4.6 Effect of air flow velocity on upstream char front spread rate both for two-dimensional and three-dimensional case.

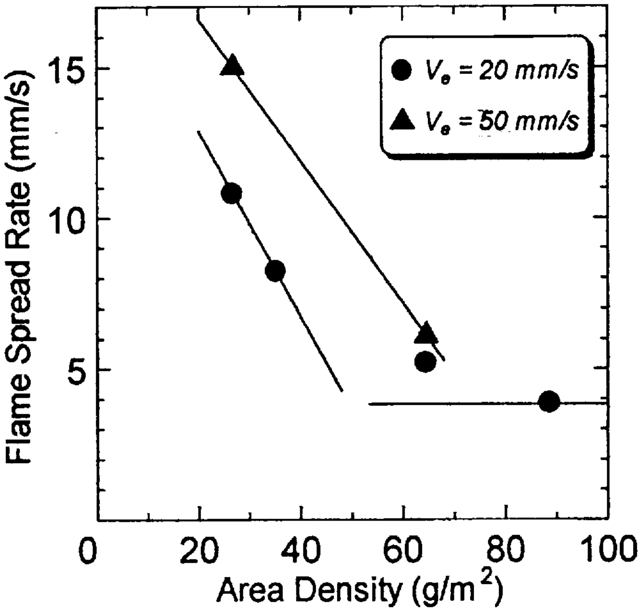

Fig. 4.7 Effect of area density on upstream flame spread rate for three-dimensional case.

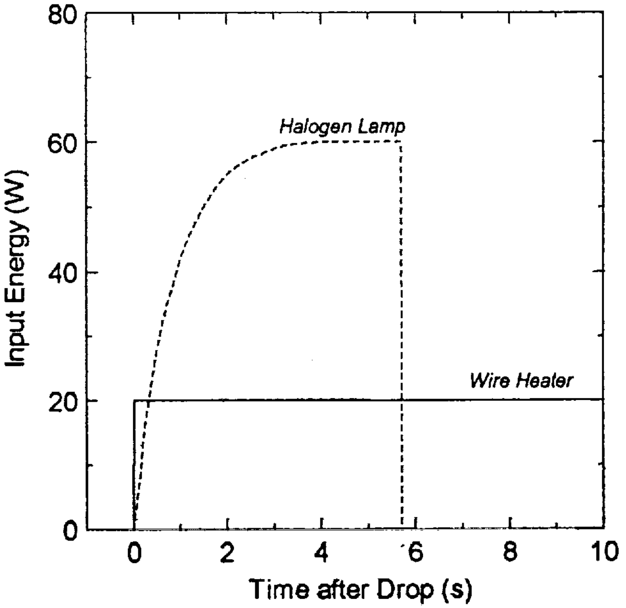

Fig. 4.8 Change in input energy for the wire heater and halogen lamp as a function of time.

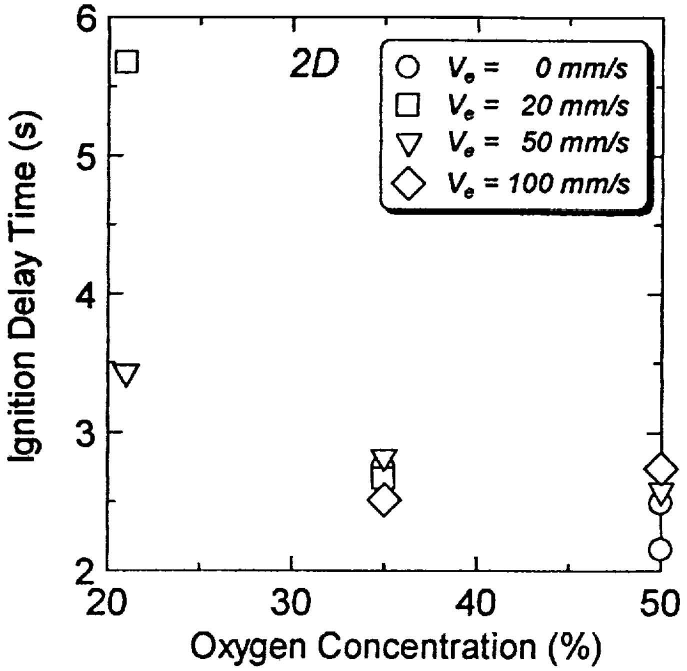

(a) Wire ignition (two-dimensional case)

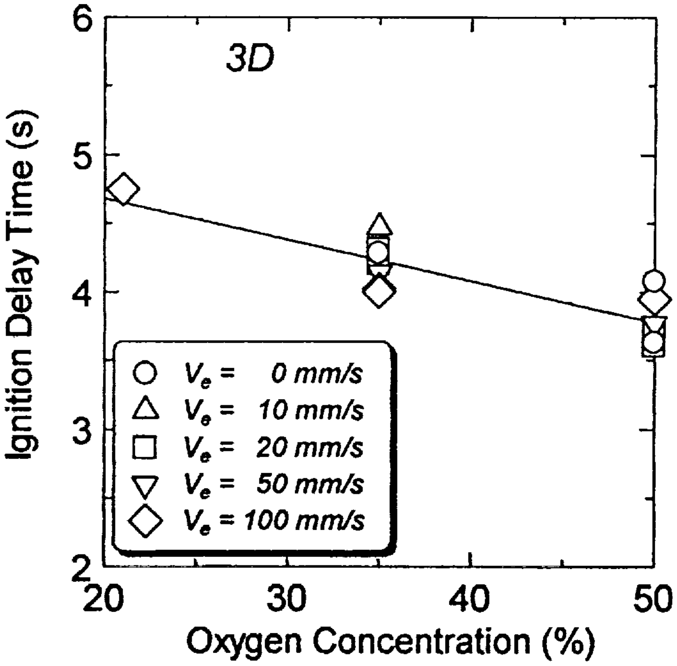

(b) Lamp ignition (three-dimensional case)

Fig. 4.9 Effect of oxygen concentration on ignition delay.

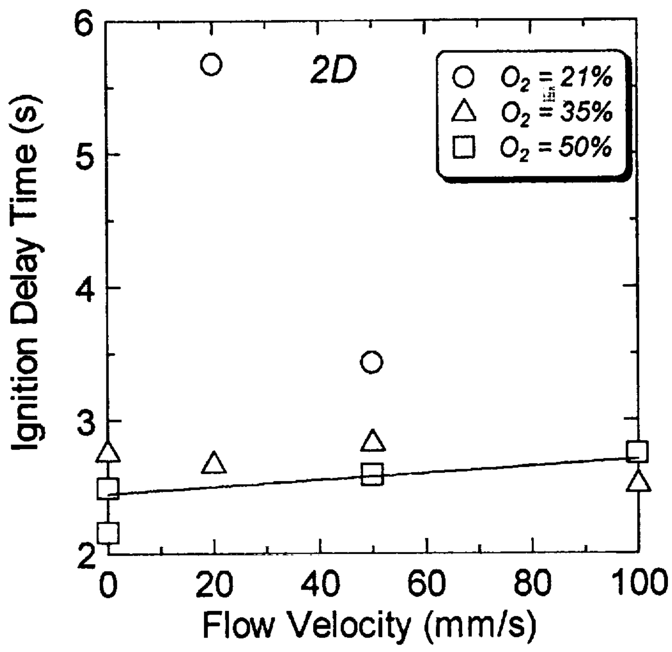

(a) Wire ignition (two-dimensional case)

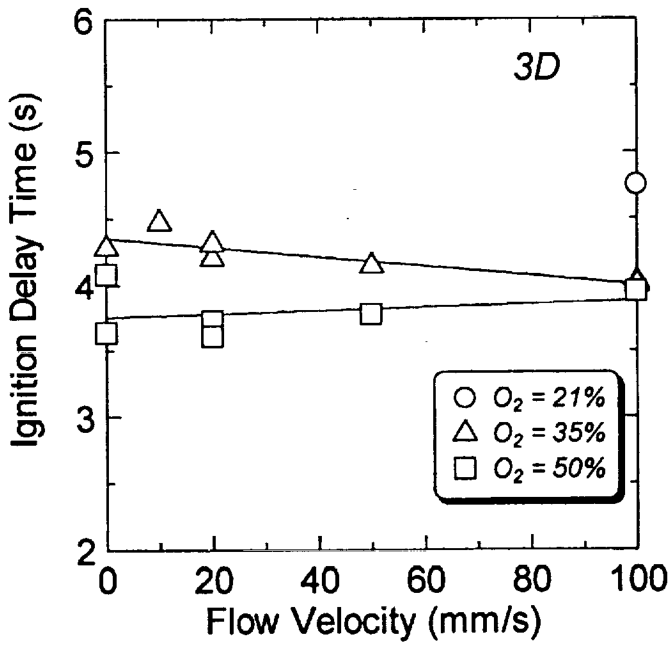

(b) Lamp ignition (three-dimensional case)

Fig. 4.10 Effect of air flow velocity on ignition delay.

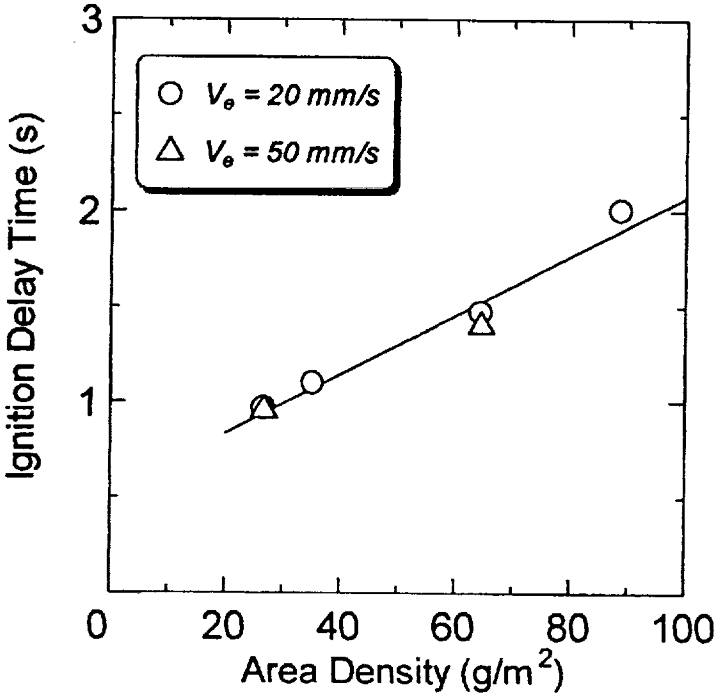

Fig. 4.11 Effect of area density on ignition delay for three-dimensional case.

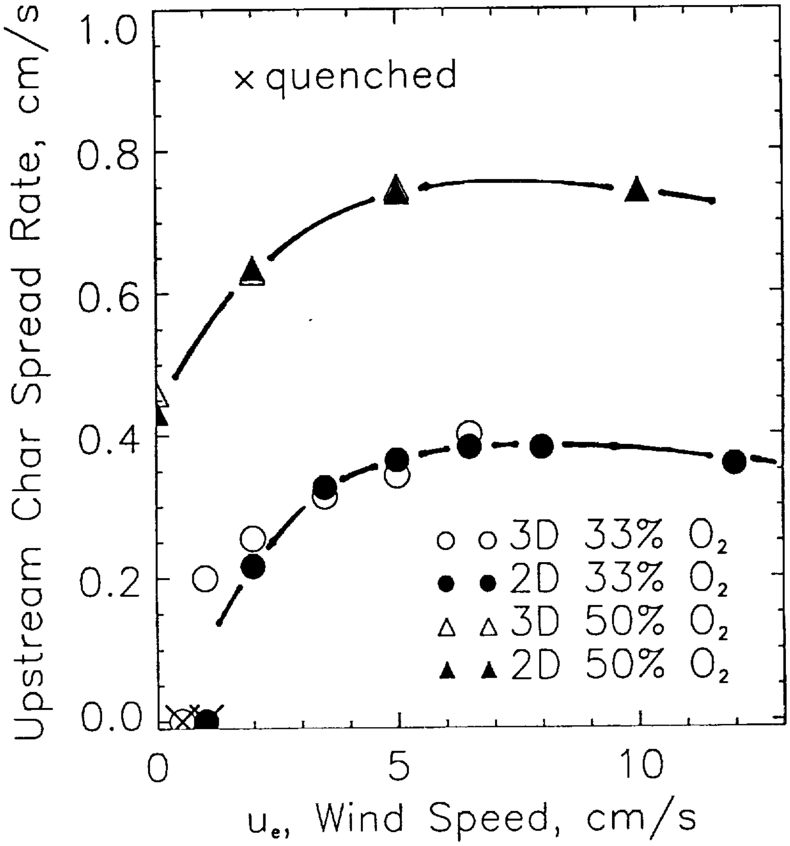

Fig. 4.12 Calculated upstream char front spread rate versus air flow velocity.

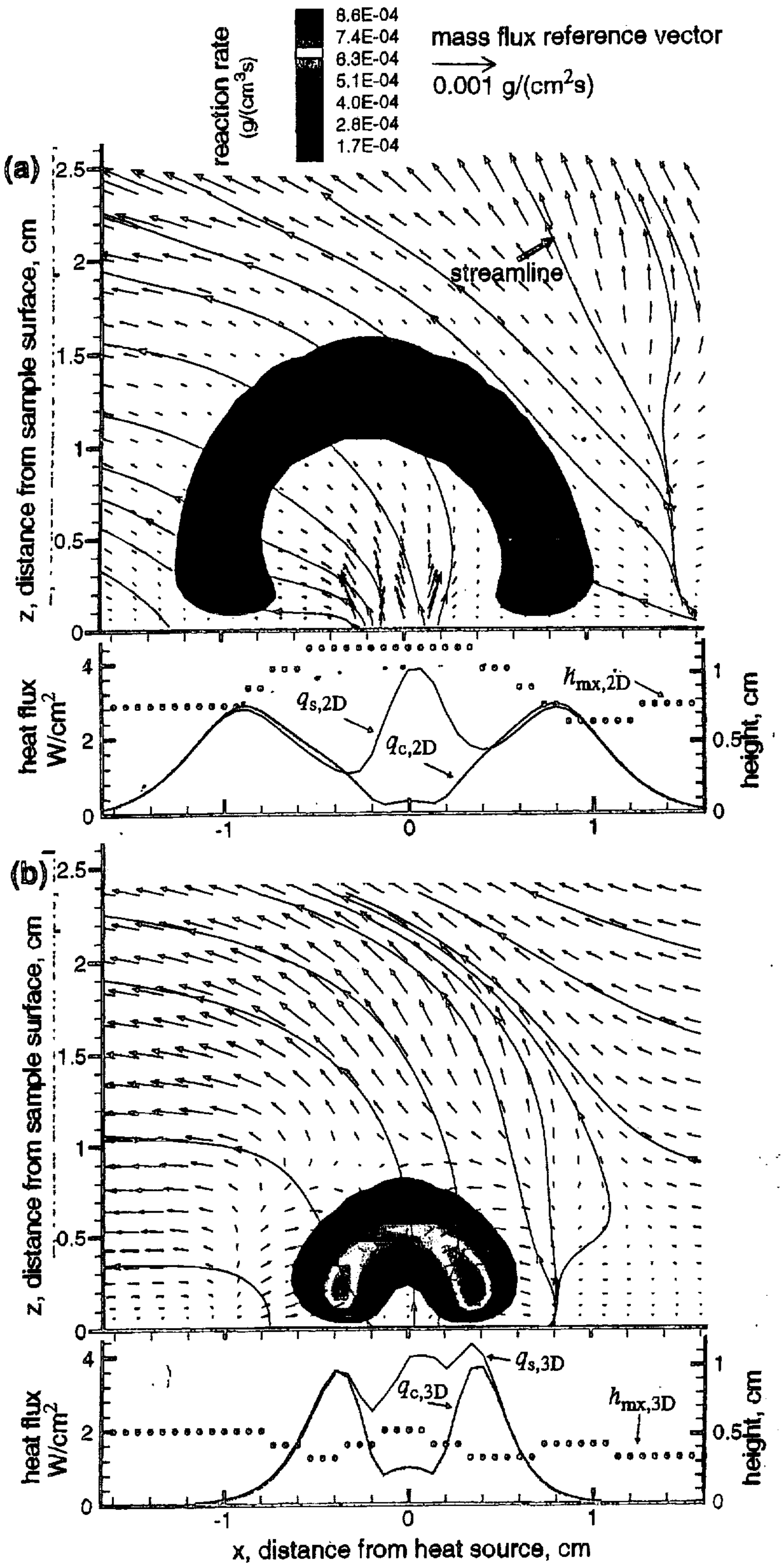

Fig. 4.13 Calculated centerline profiles of the net heat flux, the conductive/convective heat flux, and the height at which the maximum temperature occurs. Color contours of the reaction rate, oxygen and fuel mass flux vectors, and velocity streamlines are also indicated.

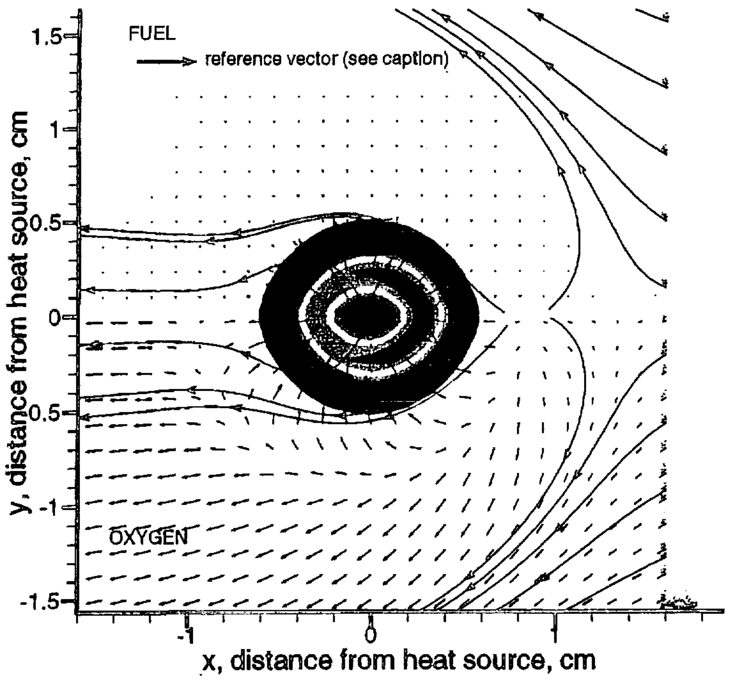

Fig. 4.14 Calculated streamlines and mass flux vectors for both the oxygen and fuel for three-dimensional case.

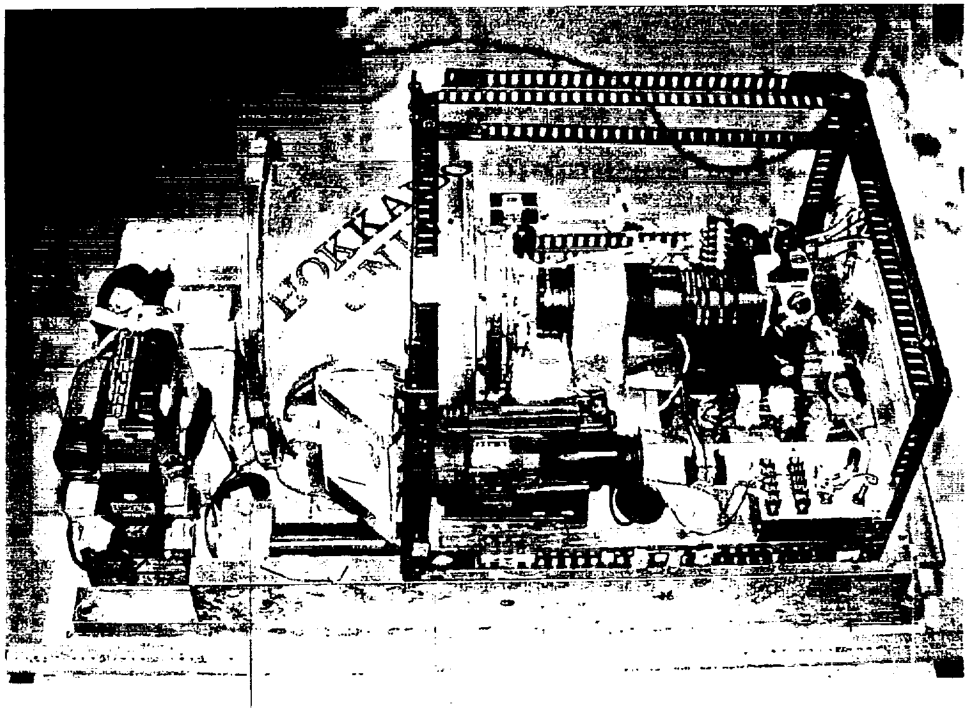

Fig. 5.1 Direct picture of the experimental apparatus.

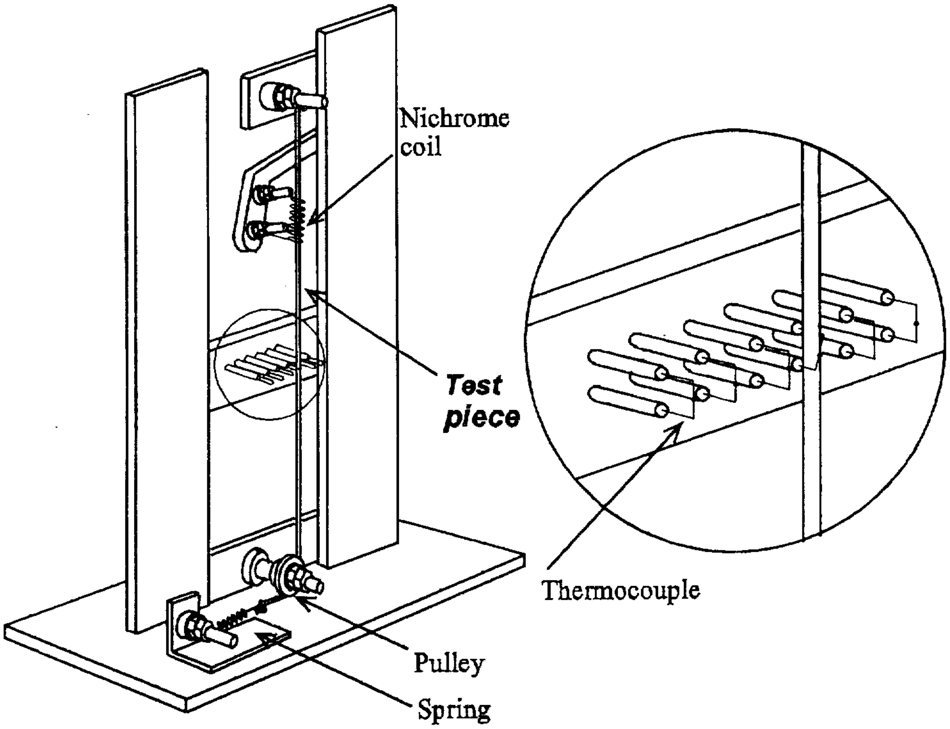

Fig. 5.2 Sample holder and ignition method.

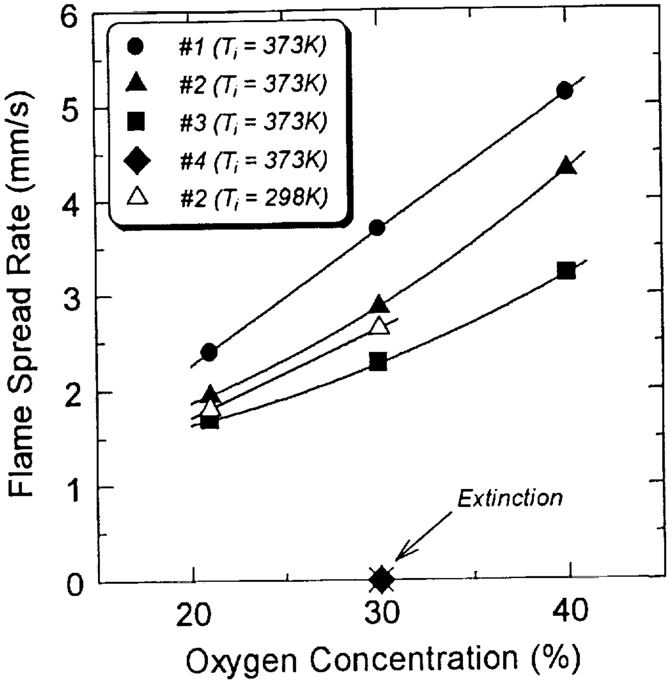

Fig. 5.3 Effect of oxygen concentration and initial sample temperature on flame spread rate.

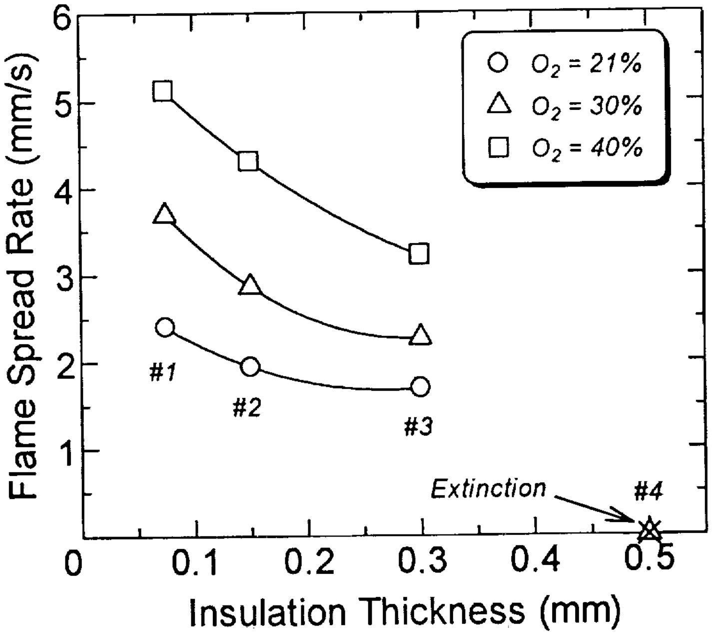

Fig. 5.4 Effect of wire insulation thickness on flame spread rate.

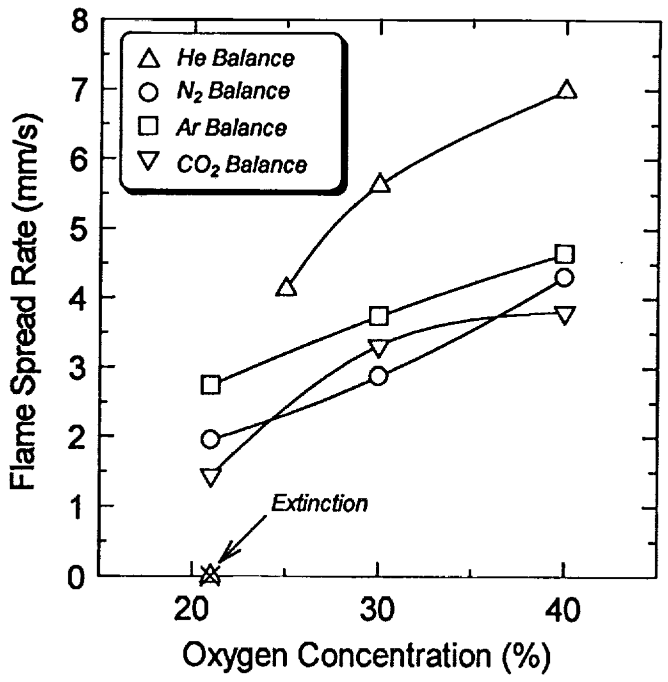

Fig. 5.5 Effect of dilution gas on flame spread rate.

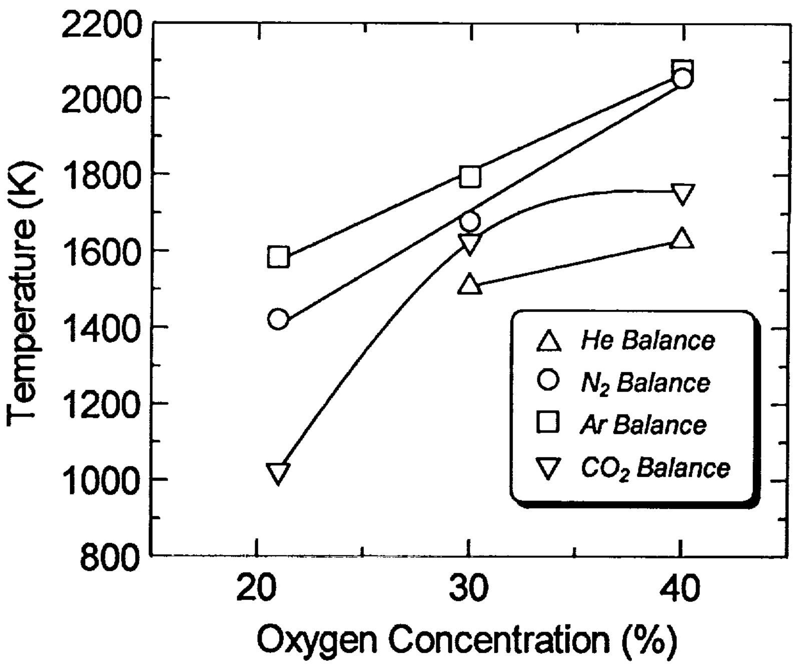

Fig. 5.6 Measured maximum gas phase temperature versus oxygen concentration.

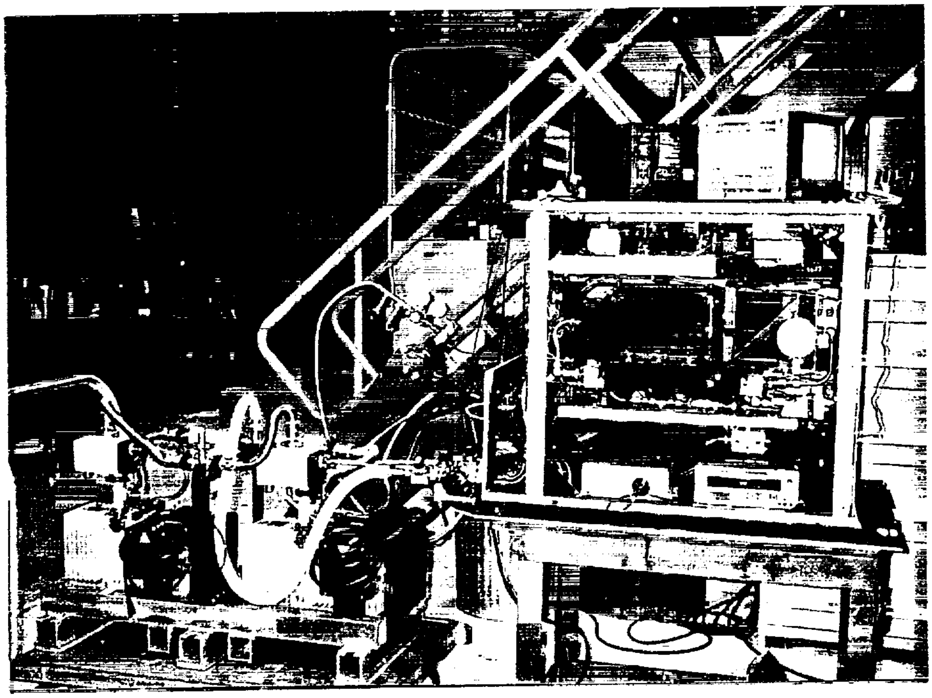

(a) Front view

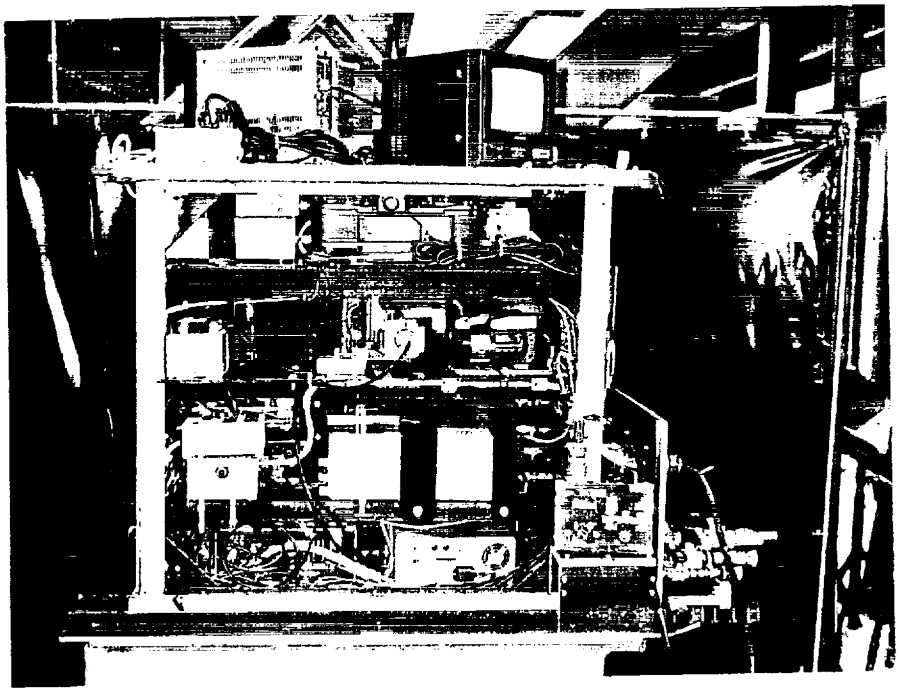

(b) Rear view

Fig. 5.7 Photograph of experimental rig to be employed on the parabolic flight.

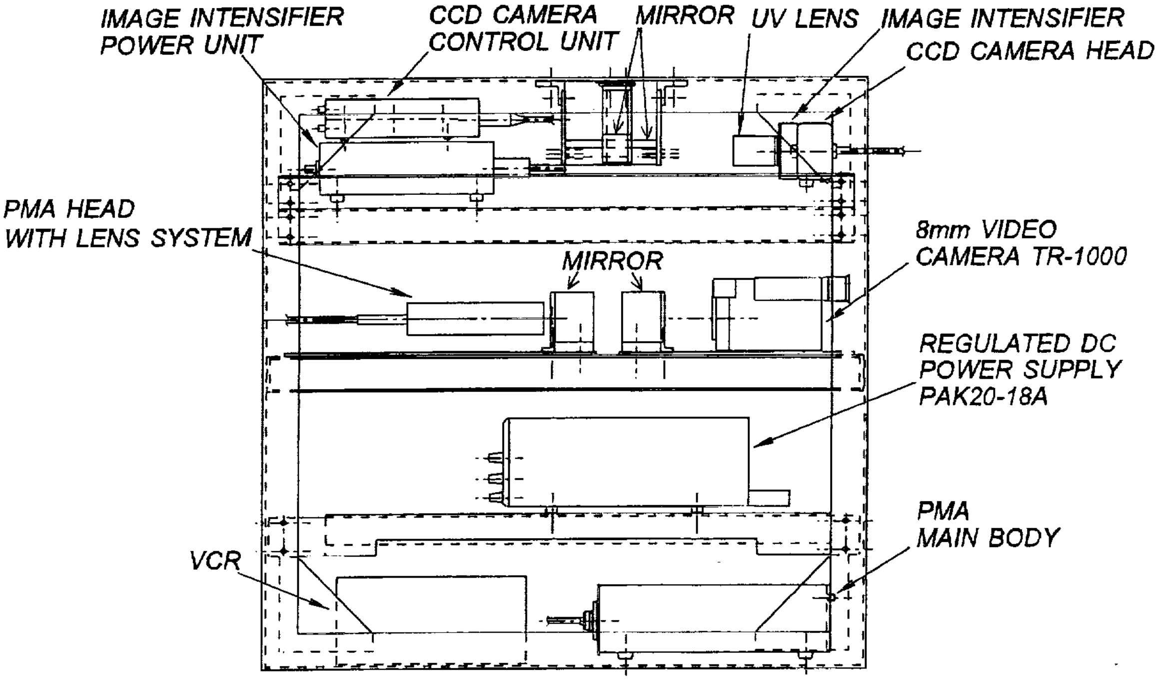

Fig. 5.8 Experimental set-up for parabolic flight.

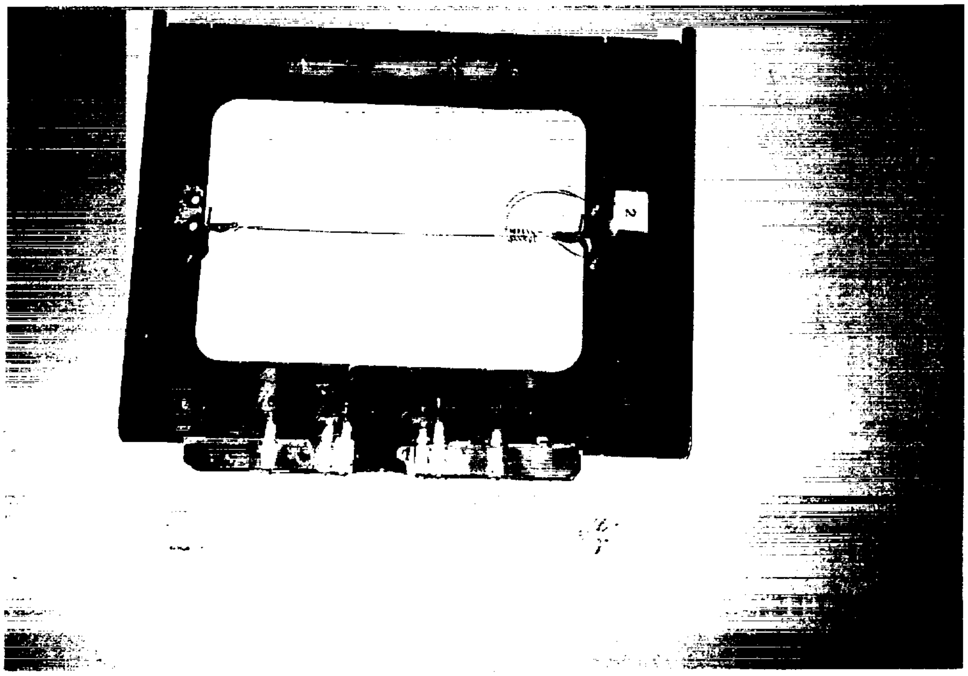

Fig. 5.9 Photograph of sample holder.

Flammability Limits and Flame Dynamics of Spherical Flames in Homogeneous and Heterogeneous Mixtures

Takashi Niioka (PI, Japanese-side), Hideaki Kobayashi, Kaoru Maruta,
Hironao Hanai and Mitsuru Ueki
Institute of Fluid Science, Tohoku University

Paul D. Ronney (PI, USA-side), Ming-Shin Wu and Mohammed Abid
Departments of Mechanical Engineering and Aerospace Engineering,
University of Southern California

ABSTRACT

This document reports the flammability lean limit and the flame dynamics of homogeneous mixture with small Lewis numbers and heterogeneous mixtures of solid particles and air, measured and observed in microgravity field. Microgravity experiments were carried out in the Japan Microgravity Center, in which 10-second duration of microgravity field of 10^{-4}g or less is given.

As for heterogeneous mixtures, a particular phenomenon found in flame propagation of PMMA particle-clouds is demonstrated. The flame propagation experiments were performed in microgravity to prevent sedimentation of the particles and the effect of buoyancy on the flame, by using a closed-vessel method and spherical polymethylmethacrylate (PMMA) particles as fuel. Observation of the flame by use of a CCD video camera, and the time history of pressure and ionization current showed that the flame propagation with alternating fast and slow modes occurred. This phenomenon is called "pulsating flame" in this paper. The pulsating flame appeared only near the lean flammability limit. The calculation results from a simplified particle-cloud model, paying attention to temperature differences between particles and gas, imply that the pulsating flame propagation arises from a cycle of conduction heat loss to the particle behind the flame and preheating of the particle-cloud in the unburned mixture.

As for homogeneous mixtures, a few several spherical flames are stationary developed near the lean flammability limit when the mass transfer rate is sufficiently larger than the heat transfer rate, that is, the Lewis number is fairly smaller than unity. Flame balls with the large diameter of about 1 cm were stationary observed, deforming their shapes a little. Based on the recent microgravity experiments, the effects of various diluent gases on steady, source-free spherical premixed flames ("flame balls") were modeled using a time-dependent numerical code with detailed chemical, transport, and radiation sub-models. The diluent gas affects the Lewis number (Le) and radiative properties of the flames. Numerical solutions for the steady properties and stability limits were obtained for lean H_2-air, H_2-O_2, H_2-O_2-CO_2 and H_2-O_2-SF_6 mixtures. Significant influences of the chemical mechanism were found, even for mechanisms that properly predict the burning velocities of H_2-air mixtures away from extinction limits. Sensitivity analysis showed that the discrepancies are due mainly to differences in the $H + O_2 + H_2O \rightarrow HO_2 + H_2O$ rate parameters for these mechanisms.

1. Introduction

Combustion of heterogeneous mixtures consisting of combustible particles and oxidizer is important in many areas of engineering, for example, coal combustion, dust explosion hazards, and propulsion systems. Many experimental and theoretical studies of combustion of particle-clouds [1-4] have been performed to explore combustion characteristics such as burning velocity, quenching distance, flammability limit, minimum ignition energy, and flame structure. However, in spite of strong practical interest, the fundamental combustion mechanisms of heterogeneous mixtures of this kind are still not known well.

There are two reasons for the difficulties in particle-cloud combustion research. One is the complexity of the combustion process. Because each particle burns through pyrolysis, gasification, mixing, and ignition, the combustion characteristics are strongly affected by chemical and physical properties and distributions of shape and size of the fuel. Therefore, the use of a simplified model of particle-cloud combustion with a simple composition and a monodispersion of fuel particles is desired for understanding the combustion mechanism. The other reason is the difficulty of performing combustion experiments in normal gravity, where most of the previous experiments for combustion of particle-clouds have been conducted. This involves problems with gravity causing sedimentation of fuel particles as well as buoyancy of the flame. Consequently, an external force such as a forced flow and electromagnetic field, which often has strong effects on the combustion process [5,6], is required for suspension of the particles in air in normal gravity. For instance, a forced flow, although it is easy to use, strongly influences the transport processes rather than diffusion processes of the particle flames themselves and tends to stratify the particle-cloud in eddies by centrifugal forces which often result in flame quenching.

On the other hand, a microgravity field can provide "ideal" conditions for combustion experiments of particle-clouds. Turbulence generated by an air jet to disperse particles into an experimental device decays without sedimentation of the particles, and no buoyancy effect due to the flame appears. Therefore, microgravity experiments are very effective for elucidating combustion mechanisms of particle-clouds. [7-13].

It is well known that radiation heat transfer is the dominant process affecting flame propagation of particle-clouds. The radiation heat transfer produces excess enthalpy in the combustion field, increases burning velocity, and also increases the flame thickness drastically [14]. However, the radiation behavior in the particle-cloud combustion is so complicated that the influences of radiation have not yet been understood quantitatively. Joulin et al. [15-17] described the effects of radiation heat transfer in a mixture of reactive gas and inert particles analytically. In their model, the radiative heat transfer from the particles in the burned gas to the particles in the fresh mixture is the dominant process. Buckmaster et al. [18,19] also showed the effects of the radiation heat transfer on the spherical propagating flame with a model similar to that suggested by Joulin et al. [15-17].

Recent microgravity experiments in drop towers [20], aircraft [21] and orbiting spacecraft [22] have shown that stable, stationary spherical premixed flames ("flame balls") can exist near flammability limits in mixtures with low Lewis number (Le), defined as the ratio of the thermal diffusivity of the bulk mixture to mass diffusivity of the stoichiometrically limiting reactant. Flame balls are supported by diffusion of reactants to the ball surface and heat and product diffusion away from the ball. Convection plays no role; the mass-averaged fluid velocity is zero everywhere at steady-state. Consequently, flame balls represent probably the simplest possible flame and thus are attractive for comparison to theoretical and computational models.

Theories [23-25] and numerical simulations [26-28] of flame balls show that while equilibrium solutions exist for all combustible mixtures, Le and volumetric radiative heat loss effects play dominant roles in determining flame ball stability. Low Le is required so that increasing curvature enhances flame temperature (thus heat release rate). Radiative loss is required so that increasing the flame ball radius (r^*) decreases temperature. This is because the temperature gradient at the ball surface decreases linearly with r^* but the surface area increases with r^{*2}, thus the net heat release increases linearly with r^*, while the volumetric loss is proportional to r^{*3}. Since the loss increases more rapidly with r^* than does heat release, the larger flame have lower temperature and thus lower reaction rate. Of course, the loss must be small enough to avoid extinguishment. With these two features, stable solutions exist for a range of mixtures near extinction limits. (With radiative loss, two equilibrium radii exist for every mixture, but the other branch of smaller, nearly adiabatic flames is always unstable [23-25,28].)

Despite the simplicity, to date the agreement between model predictions and experimental observations, particularly with regard to the flame ball radius, has not been satisfactory [21,28,29]. One substantial problem is the uncertainty in the appropriate chemical model to employ for the very lean H_2-O_2-diluent mixtures in which most flame ball studies have been conducted; different published chemical mechanisms predict widely varying flame ball properties, even among models that predict the burning velocities of propagating planar H_2-air flames quite well [29]. The flame ball calculations compare favorably with independent calculations [30] when the same chemical and radiation sub-models are employed, thus numerical accuracy issues are not considered a significant factor in these discrepancies.

Recent improvements in intensified video camera technology have now made OH imaging feasible, even in drop-tower and aircraft μg experiments. UV emissions from OH are more indicative of the location of heat release because they occur only where O, H and OH radicals are present, whereas the near-IR/visible emissions are more indicative of the locations where H_2O and other stable radiating species are present at high temperature. The former may provide a more meaningful test of H_2-O_2 chemical kinetic models. Consequently, the purpose of this study is a comparison of predicted and measured UV emissions from excited-state OH molecules, and a comparison of the UV emissions to near-IR/visible emissions from H_2O (and to a lesser extent CO_2 and SF_6 in mixtures containing these molecules).

In one work on combustion of heterogeneous mixtures, lean flammability limit are measured under a microgravity condition, and a particular phenomenon found in flame propagation of PMMA particle-clouds near the lean flammability limit in microgravity, i.e. pulsation flame propagation, are reported. And in another work on flame balls, experiments are performed using varying diluent gases to study Le and radiation effects, and diluent effects are assessed numerically for comparison with theoretical predictions [23-25] and the results of experiments.

2. Flame behavior of PMMA Particle-Cloud near the Lean Flammability Limit

2.1 Experimental Apparatus and Method

The spherical PMMA particles used in the present experiment have a narrow size distribution with mass median diameters of 5.0, 8.4, 13.5, 30.4, and 48.5 μm. Microgravity experiments were performed at the Japan Microgravity Center (JAMIC). Figure 1 shows a schematic diagram of the experimental apparatus. The experiments were conducted using a cylindrical steel vessel with an inner diameter of 200 mm and a length of 250 mm (8-liter). A particle dispersion device is mounted at the end of the vessels as shown in Fig. 1. PMMA particles are injected with an air jet and are dispersed in the vessel as soon as the drop capsule is released, producing a uniform mixture of particles and air in the vessel. The dispersion air raised the pressure in the vessel up to 0.11 MPa absolute. We confirmed the uniformity of the mixture by particles sampling with syringe. Charge-coupled device (CCD) images of the particle clouds in microgravity illuminated by a halogen lamp also showed that the particle cloud is quiescent and uniform at 6 seconds after the termination of the dispersion jet. The igniter using an electrically heated wire was activated at the center of the vessel, and then flame propagation occurred. In this paper, the fuel concentrations are represented by the equivalence ratio accurately calculated by excluding the PMMA particles that remained in the fuel pool and stuck on the vessel wall. A window with a diameter of 200 mm was installed at the opposite side of the particle dispersion device to observe the flame in the vessels A CCD video camera was placed ahead of the windows. The pressure in the vessel was measured with a pressure transducer mounted on the vessel wall. The instantaneous flame position was monitored by using ionization probes consisting of platinum wire with a diameter of 0.4 mm installed in the vessels. A notebook PC recorded the output signal of the pressure transducer and the ionization probes via an A/D converter.

For the purpose of comparison with the microgravity experiments, combustion experiments in normal gravity were also conducted using the same experimental set up. However, in order to prevent significant sedimentation of the particles, ignition of the mixture had to be made as soon as the air jet for particle dispersion was terminated.

2.2 Results

(a) Flame Propagation Characteristics in Normal Gravity and Microgravity

Photographs of typical propagating flame of PMMA particle clouds in normal gravity and microgravity reproduced from the video images are shown in Figs. 2 (a) and (b), respectively. The flame propagates outward with time but, in normal gravity, the shape of the flame is not spherical as shown in Fig. 2 (a). Since the particles are ignited just after the end of the dispersion of particles to prevent the sedimentation of the PMMA particles in air, the flame propagates with strong turbulence. In the case of large particles, a stronger air jet is needed to disperse uniformly and to sustain the particles in air because the terminal velocity (0.1 cm/s for a 5 μm particle and 9 cm/s for a 48.5 μm particle) is large. As mentioned before, ignition has to be made before the decay of turbulence because sedimentation of particles occurs rapidly. Buoyancy must also affect the flame shape. Therefore, the flame is usually corrugated. On the other hand, in microgravity, the flame propagates spherically because the ignition was delayed until the turbulence decayed sufficiently and the mixture became quiescent, as shown in Fig.2 (b).

Figure 3 shows the flame speeds as a function of equivalence ratios of PMMA particle-clouds with the particle diameter of 8.4 μm in normal gravity and microgravity. The flame speed was measured by the outputs from the ionization probes. The data at the bottom of Fig. 3 indicate the cases in which flame propagation did not occur. We can see from Fig. 3 that the flame speeds in normal gravity are larger than those in microgravity, and the former data are scattered, indicating clearly the effects of the turbulence induced by the dispersion air jet. Kauffman et al. [5] and Pu et al. [6] investigated the effects of turbulence on burning velocities of dust flames in a closed vessel and showed that a stronger turbulence in the vessel produces larger burning velocities.

The combustion of particle-cloud is affected by several factors in the normal gravity experiments; i.e., turbulent flows due to dispersion of fuel particles, buoyancy caused by the flame, and sedimentation of fuel particles. In these effects, the sedimentation and turbulence cannot be controlled independently. In order to reduce the turbulence in the normal gravity experiments, the ignition of the mixture was delayed for 1 second after the dispersion was terminated. As shown in Fig. 3, the flame speed becomes smaller compared to that for zero-delayed ignition because of the decay of turbulence and the decrease in particle concentrations due to sedimentation. As a result, some experimental conditions near the lean flammability limit resulted in smaller flame speeds than those in microgravity.

(b) Lean Flammability Limit in Normal gravity and Microgravity

The lean flammability limits as a function of particle diameter in the normal and the microgravity experiments are shown in Fig. 4. The determination of flammability or nonflammability was made according to the flame behavior observed by video images and pressure histories. If the flame propagates for a short distance and then is extinguished, the pressure rise is very small because a rapid increase in pressure occurs at the last stage of combustion. This case was defined as nonflammable in this experiment. Although the mixture was strongly turbulent under normal gravity conditions when ignited, the lean flammability limits in normal gravity almost agreed with those in microgravity in a range of diameters from 8.4 μm to 30.4 μm. For the large particle diameter of 48.5 μm, however, the lean flammability limit in normal gravity was narrower than that in microgravity. Furthermore, for larger particles with a mass median diameter of 100.0 μm that is not indicated in Fig. 4, the equivalence ratio at the lean flammability limit in normal gravity was 4.7 which was much larger than the value predicted by extrapolation of the data in microgravity. This is due to the large terminal velocity (9 cm/s for the 48.5 μm particles and 35 cm/s for the 100.0 μm particles) under the normal gravity condition. It is difficult to keep the particles in air and to produce a uniform mixture. Actually, even with a stronger air jet, it was doubtful that the mixture of the 100.0 μm particles and air became uniform in normal gravity. Consequently, we can say that turbulence and buoyancy are less effective for the determination of lean flammability limits of particle-cloud combustion, while the sedimentation effect is much more effective particularly for larger particles.

Judging from these results, measurements of the lean flammability limit of a heterogeneous mixture in normal gravity as well as measurements of the burning velocity are very difficult in terms of obtaining accurate data under the normal gravity condition particularly for large particles. Therefore, a microgravity condition where quiescent and uniform mixtures are obtainable is essential for these measurements.

(c) Combustion characteristics in microgravity

The effects of the equivalence ratios and the particle diameters on the flame speed measured in microgravity are shown in Fig. 5. From this figure, it is seen that the flame speeds in microgravity decrease as the particle diameters are increased. This tendency basically agreed with the previous studies [31-33] using a flat flame burner, a propagation tube, and a closed vessel in normal gravity although the normal gravity experiments have the difficulties mentioned above. As seen in Fig. 5, the flame speed rapidly decreases as the equivalence ratio near the lean flammability limit is decreased, and then the lean flammability limit appears. Thus the pertinence of the method we employed was confirmed.

The equivalence ratios at the limits for the PMMA particle-cloud with the diameters of 8.4, 13.5, 30.4, and 48.5 μm in microgravity are 0.68, 0.76, 0.86, and 1.05, respectively, as shown in Fig. 4. For the particles with the mean diameters ranging from 8.4 to 48.5 μm, the lean flammability limit increases linearly as the mean diameter is increases. Mizutani and Ogasawara [34] showed, in the theoretical study of spray combustion assuming no sedimentation of droplets and no buoyancy, that the lean flammability limit increases gradually as the droplet diameter becomes larger. The results in the present study qualitatively agree with those in their theoretical study.

Hertzberg et al. [35,36] showed that the lean flammability limit of dusts such as polyethylene, coal, and PMMA dust were independent of the particle size below the critical diameter of 100 μm in normal gravity conditions. They mentioned that the volatile evaporation of the particles below the critical diameter must be completed before or in the flame, so that the lean limit strongly depends on the concentration of combustible volatile. For the larger diameters than the critical value, the concentration of particle clouds at the lean flammability limit rapidly increased. They showed that the equivalence ratio at the lean limits was a constant, that is, 0.47 for a PMMA particle-cloud with a particle diameter below 100 μm, which is lower than 0.68 for much smaller particles of 8.4 μm in the present result. This difference might be caused by the pyrotechnic igniters they used. Zhen and Leuckel [37] examined the effect of ignition energy of pyrotechnic igniters ranging from 75 J to 10 kJ on a dust explosion in 1-m^3 and 20-liter vessels, and showed that the 10 kJ igniter significantly enhanced the combustion rate compared with the low energy igniters. It is presumed, therefore, that the strong pyrotechnic igniter used by Hertzberg et al. [35,36] significantly extended the lean flammability limit.

(d) Pulsating flame propagation near the lean flammability limit

The pulsating flame occurred only for the mixture near the lean flammability limit. Here, first of all, we present an outline of the phenomenon of the pulsating flame. When a nichrome hot wire igniter is activated, a flame kernel is formed around the igniter and flame propagation starts immediately. Soon the flame speed decreases and the brightness of the flame also decreases. However, the flame that seemed to be weakened, forms another bright flame around the weakened flame and starts to propagate fast. And again, the flame becomes weak and then repeats the same process. Thus, the flame propagation repeats this sequence in a pulsating manner. We call this phenomenon "pulsating flame". This phenomenon seems to be different from flame instabilities, such as acoustic-type and Helmholtz-type instabilities.

Photographs of the pulsating flame taken by the CCD camera, 60 frames per second, are shown in Fig. 6. The mean particle diameter is 30.4 μm and the equivalence ratio is 1.78. As seen in Fig. 6, a flame kernel is formed when the mixture is ignited by the hot nichrome-wire and then flame propagation commences (17 ms), but the flame speed decreases drastically and brightness of the flame decreases gradually (50 ms). The flame appears to be almost extinguished (67 ms). Then, the weakened flame suddenly forms a new flame front around it, and brightness with luminous of flame (83 ms) greatly increases. Thereafter, the flame speed and brightness decreases again (133 ms-167 ms), and the flame behaves as before (183 ms). Thus, "strong" and "weak" combustion appears repeatedly during the flame propagation.

Figure 7 shows the movement of the flame front with time. In Fig. 7, solid circles are the data that estimated with VTR images shown in Fig. 6 and circles are the data that calculated by the output signals of the ionization probes. As mentioned before, it was difficult to correctly determine the exact point of ignition of the mixture with each method. Therefore, each datum in Fig. 7 is plotted assuming that the peak output of the probe located at 3.31 cm from the ignition point corresponds to the time of the flame radius of 3.31 cm measured by the VTR images. As seen in Fig. 7, the flame movements measured by the two methods agree with each other and show the pulsation phenomena.

Typical time histories of the pressure and the gradient of pressure rising (dP/dt) in the vessel, when the pulsating flame propagating occurred, are shown in Fig. 8. The mean particle diameter was 8.4 μm and the equivalence ratio was 0.75. The abscissa in Fig. 8 is also arbitrary time for the same reason as previously noted. As seen in Fig. 8, the dP/dt has several minima and maxima on its curve, indicating the existence of pulsating flame propagation. In this case, five maxima exist between the starting point of the pressure rise around 0.6 to 0.7 seconds and the maximum pressure point.

Frequency of the pulsating flame in the vessel as a function of the equivalence ratio and the particle mean diameter is shown in Fig. 9. The frequency was calculated from the intervals between the turning points on the curve of dP/dt. Because the frequency slightly increased with the pressure, the averaged frequency for each experimental condition was calculated. As seen in Fig. 9, the frequency increases and then decreases with increasing equivalence ratios. Also, the frequency decreases with increasing particle diameters. The range of the equivalence ratio in which the pulsating flame is observed is extended with increasing particle diameters; that is, the maximum equivalence ratio for pulsating flames are 1.2 for 8.4 μm and 13.5 μm particles and 1.8 for 30.4 μm particles, respectively. In the case of 48.5 μm particles, the maximum equivalence ratio could not be detected because of the limitation of equivalence ratio range in this experiment.

Figure 9 can be explained as follows. With the decrease in particle diameter at a constant equivalence ratio, that is, an increase in the number of particles per unit volume, the absorption length of radiation decreases, and the flame speed increases as shown in Fig. 5. Also, in this case, since the heat capacity of a unit particle decreases, the cycle of pulsation increases so that the frequency increases. A further decrease in particle diameter results in complete gasification of the particle near the flame front; thus, the pulsating flame cannot appear any more, because the flame behaves like ordinary gaseous flame.

On the other hand, with increasing particle diameter, the frequency of pulsation decreases and the amplitude increases. In the case of larger particles, however, it is difficult to observe pulsating flame in laboratory scale experiments because the absorption length is so large. Near the lean flammability limit where the number of the particles is small, the flame temperature is very low and the amount of radiation is small so that it becomes impossible for the pulsating flame to occur. When the equivalence ratio is increased, the absorption length decreases and the flame temperature increases so that the frequency of pulsation is increased. With further increases in equivalence ratios, the heat release rate becomes high and the effect of the large particles as the effect of the heat absorber decreases, causing steady flame propagation.

However, as shown in Fig. 9, the frequency increases with the equivalence ratio and then decreases again after reaching a maximum frequency at a certain equivalence ratio. This mechanisms are not clear at present, but some possibilities can be stated. For example, with increasing equivalence ratio, the form of the particles combustion changes to group combustion [38]. In such a case, the volume fraction of luminous flame decreases and the amount of radiative heat transfer decreases, causing the frequency of the pulsation to decrease. Also, since the heat capacity per unit volume increases, heating time increases and hence the frequency decreases. To confirm this mechanism, the degree of change in radiation heat amount for increased equivalence ratios should be measured.

Judging from the images of flame shown in Fig. 6, it seems that some heat losses and some heat gains in the gas phase of the flame region depending on time, cause the pulsating flame of particle clouds. It is suggested that the heat losses are related to the heat conduction to PMMA particles and the heat to be used for pyrolysis of solid particle in flames, while the heat gain is related to the preheating of particles in fresh mixtures by radiation from the flames. Therefore, the flame is weakened first by the heat loss, but then enhanced by the radiation heat gain so that the fast and the slow propagation flame occur repeatedly.

(e) Numerical simulations of pulsating flame

The radiation behavior in the particle-cloud combustion is so complicated that the influences of radiation have not yet been understood quantitatively. Joulin et al. [39-41] described the effects of radiation heat transfer in a mixture of reactive gas and inert particles analytically. In their model, the radiative heat transfer from the particles in the burned gas to the particles in the fresh mixture is the dominant process. Buckmaster et al. [42,43] also showed the effects of the radiation heat transfer on the spherical propagating flame with a model similar to that suggested by Joulin et al. [39-41].

A numerical simulation was conducted by using a flame model based on the conduction heat loss to the particles in and behind the flame and the radiation heat exchange between the particles. To simplify the phenomena, a flame propagating model of a gaseous mixture seeded with inert particles was employed. The nonsteady equations for energy and species conservation were solved in rectangler coordinates at constant pressure. The particle assumed a black body.

Figure 10 shows burning velocities at various conditions. As seen in Fig. 10, the pulsating phenomena exist in this system. Calculation results such as the dependence of pulsation frequency on the particle diameter and the particle weight concentration agreed qualitatively with those in the experimental results.

Consequently, we understand that the mechanism of pulsating flame of particle-clouds is due to a cycle of the conduction heat loss to the particle behind the flame, which makes burning velocity slower, and the preheating of the particle-cloud in the unburned mixture, which makes burning velocity faster.

3. Flame balls near flammability limit

3.1 Experimental Apparatus and Method

A total of 30 drop-tests were conducted in the JAMIC facility. The experimental apparatus consisted of a combustion chamber, spark generator, and video imaging system. The entire experimental apparatus described below was mounted in a 0.92 m x 0.87 m x 0.43 m frame that was installed in the JAMIC drop capsule. The combustion chamber was a cylindrical vessel with inside diameter 200 mm and length 250 mm. Quartz windows on the side and on top of the vessel enabled observation of the flames by the intensified video cameras described below. The combustible gas mixtures tested in this chamber were prepared by filling a mixing chamber via the partial pressure method, then transferring this mixture to the combustion chamber. Except where noted otherwise, all tests were conducted at an initial pressure of 1 atm. The estimated accuracy of the mixtures is ±1 % of each component, *e.g.*, 5.00 ± 0.05% H_2. This accuracy level was verified by gas chromatography. The spark generator, which was functionally identical to that used in previous μg experiments [20,21,44], provided about 5 J of energy in 25 ms to ignite the very weak mixtures of interest in this study. The spark gap was located at the center of the chamber.

Two types of intensified video cameras were used in the JAMIC experiments. One camera, used for all tests, detected near-IR/visible emissions from 400 to 900 nm. A 12-mm focal length lens transmitted these emissions practically without attenuation. No filter was used on this camera/lens system. The other camera used in some tests was of similar design but with a different intensifier capable of detecting UV and visible emissions from 300 to 600 nm. A 50-mm focal length lens with quartz optical elements was used in order to transmit and focus these emissions. A bandpass filter centered at 310 nm with 10-nm width at 50% of the peak transmission blocked essentially all emission except that from OH^*. Both video signals were recorded by on-board 8 mm VCRs.

3.2 Numerical model

A one dimensional, time dependent flame code employing detailed chemical and transport sub-models [45,46], was employed. The usual non-steady equations for energy and species conservation were solved in spherical geometry at constant pressure. H_2-air mixtures were examined along with H_2-O_2-CO_2 and H_2-O_2-SF_6 mixtures with a fixed H_2:O_2 ratio of 0.5, corresponding to equivalence ratio=0.25, and diluted with CO_2 or SF_6 to near the extinction limits, as opposed to the H_2-air mixtures where the O_2:N_2 ratio is fixed at 0.21. The H_2-O_2 chemical kinetics were extracted from the GRI methane oxidation mechanism [47]. In H_2-O_2-CO_2 mixtures, wet CO chemistry was included though its influence was found to be negligible. N_2 and SF_6 were assumed inert. Gas chromatography confirmed that very little SF_6 decomposition occurred in the space experiments [22], which was expected since the rate of radical attack on SF_6 at combustion temperatures is much lower than the rate of radical attack on H_2 or O_2 [48,49]. No third-body recombination efficiencies could be found for SF_6, so they were assumed equal to N_2. Opticallythin radiation was assumed with loss per unit volume (L)=4 σ $a_p(T^4-T_o^4)$, where σ , a_p, T and T_o are the Stefan-Boltzman constant, Planck mean absorption coefficient, local temperature and ambient temperature (300K), respectively. Data on a_p were taken from [50] for H_2O, CO_2 and CO and [51] for SF_6.

Boundary conditions were ambient temperature and composition at the outer boundary (r=100 cm) and zero-gradient at r=0. 151 to 191 grid points were employed with dynamically-adaptive re-gridding and time-stepping. Once a steady solution for one mixture was obtained, the outer boundary composition was modified slightly and the calculation re-started to obtain solutions for other compositions. Near the lean and rich dynamic stability limits, the H_2 mole fraction (X_{H2}) was changed in increments of 0.0001 to ensure accurate limit determination. Prior work [28] showed that these limits are physical, not numerical, in nature because at these limits small positive (negative) radial perturbations from the steady solution led to expanding (shrinking) flames and eventually extinguishment, whereas farther from these limits, perturbations were damped and convergence to the steady solution was observed. Hence, our computed limits are dynamic stability limits, analogous to those determined by linear stability analyses [23-25], rather than static turning-point limits, and thus may be more readily compared to experiments.

For both computations and experiments, r^* was arbitrarily defined as the intensity profile half-width at one-third of the peak intensity. The computed intensity-based radii (r^*_{VIS}) were always slightly smaller than the computed radius at the maximum volumetric heat release rate (r^*_{HRR}). For brevity in the results reported below, r^*_{HRR} is shown for all conditions, but r^*_{VIS} is shown only for conditions where experimental data are available for comparison.

3.3 Results

(a) Flame behavior of H_2-air

Figure 11 shows the example of OH-image photo for 5% H_2-air. The same photo taken by the former KC-135 flight [26] showed flames with a shape of slender body first, each flame being divided into two flame balls. Since the g-level is very low in JAMIC, cellular flames were formed just after ignition and then the division of cellular flames into balls slowy proceeded. Slendar-body flames appeared in KC-135 flights were not observed in the present experiments. In 3.8% H_2, three large flame balls were formed just after ignition and then they were divided themselves into six balls after a few seconds. In 3.5% H_2, one large flame ball was observed. The concentration of 3.4% H_2 was outside the flammability limit, but in the present JAMIC experiment two flame balls were observed, showing the different flammmability limit. Also, flame balls observed in these experiments did not move, also being different from the parabolic flight, It should be noted from these results that the present experiments were conducted with a high quality of microgravity.

(b) Flame ball radius

The variation of the flame ball radius with the fuel concentration for H_2-air is shown in Fig. 12. There are not enough data at this stage to discuss in detail, but radii obtained by these experiments are larger than those obtained by the KC-135 flights. According to the former analytical result [26], when heat loss decreases, the flame ball radius becomes large in cold giant balls. This must be the reason why radii become small in KC-135 flights, in which drift of balls was caused and therefore heat loss increased. Actually, when flame balls did not drift much in the parabolic flight, their radii increased [21].

(c) Radial profiles

Figure 13 shows non-dimensional radial profiles of temperature, integrated heat release (Q_R) and integrated radiative heat loss (Q_L) for H_2-air, H_2-O_2-CO_2 and H_2-O_2-SF_6 mixtures at the dynamic stability limit. Profiles of temperature and Q_R are fairly similar for all mixtures, which is expected since the radial coordinate is non-dimensionalized with r^*_{HRR}. Because heat release rates increase rapidly with temperature, heat release occurs at small r where T is highest; half of Q_R occurs at $r/r^*_{HRR}=1.7$ for all cases. Q_R rises slightly more rapidly for H_2-air than H_2-O_2-CO_2 or H_2-O_2-SF_6 mixtures because T(r) drops more rapidly for H_2-air, thus more reaction occurs at smaller r/r^*_{HRR}.

Q_L profiles are less similar because $a_{P,SF6} >> a_{P,CO2}$ and because for H_2-air the only radiator is the product H_2O, whose concentration decays to zero in the far-field, whereas for H_2-O_2-CO_2 and H_2-O_2-SF_6 the primary radiator is the diluent, whose concentration is constant in the far-field. Consequently the Q_L profile rises fastest (slowest), and far-field radiation is least (most) important, for H_2-O_2-SF_6 (H_2-air) mixtures. In all cases less than 1% of Q_L occurs at $r/r^*_{HRR}=1$ because radiative loss is far less sensitive to temperature than heat release is. Despite this fact, simple estimates [28] for flame balls in near-limit H_2-air mixtures show that near-field and far-field radiation have roughly equal influences on stability properties. Consequently, for H_2-O_2-CO_2 and H_2-O_2-SF_6 mixtures, near-field radiation is far more influential. Further evidence of the impact of near-field losses for these cases is presented later. This may explain why oscillating flame balls predicted by theory when far-field losses are important (particularly when Le is very low as in H_2-O_2-SF_6 mixtures) have never been observed experimentally nor predicted by computations using realistic chemical and transport models, and why three-dimensional breakup of flame balls, which is related to near-field losses [23,24], is always observed for mixtures not far removed from the limits.

(d) Effects of chemical models

The agreement between computed and measured values of r^*_{VIS} is unfavorable, even for H_2-air mixtures where reabsorption effects are negligible. Previously [27,28] the importance of the chemical mechanism on r^* has been noted. Figure 14a shows that three widely-accepted H_2-O_2 oxidation mechanisms [47,52,53] yield similar predictions for the burning velocities (S_L) of planar flames far from extinction limits and agree well with experiments, yet Fig. 14b shows that these models yield widely varying predictions for r^{*}_{HRR}. Also, agreement of these mechanisms with each other and with experiments is poor near the lean planar flammability limit (Fig. 14a). The inset in Fig. 14a shows that radiative losses cannot account for the discrepancies in S_L. In all cases, the mechanisms underpredict the net heat release rate for near-limit mixtures.

These observations motivate a simple sensitivity analysis on the elementary reaction rates. The results reveal that the sensitivity coefficients are highest by far for the chain-branching step $H+O_2 \rightarrow OH+O$ and inhibiting step $H+O_2+H_2O \rightarrow HO_2+H_2O$. Similar behavior is found for near-limit propagating H_2-air flames [54,55]. (Note that the sensitivity to the $H+O_2+N_2 \rightarrow HO_2+N_2$ inhibiting step is considerably lower because the efficacy of N_2 is much lower than H_2O.) The ratios of the rates at 1075K (a typical value at the location of maximum heat release rate) for the Yetter *et al.* [52], GRI [47] and Peters [53] mechanisms are 0.782:1.00:0.883 for the chain-branching step and 0.497:1.000:1.205 for the inhibiting step. Similar discrepancies exist at other temperatures. Thus, most of the differences seen in Fig. 14b are attributed to differences in the inhibition step rate. Uncertainties in this rate in this temperature range has been noted previously [55]. Decreasing the inhibition rate would improve the agreement between model and experiment and would improve the agreement in S_L for lean H_2-air mixtures (Fig. 14a). In contrast, changing the branching rate would hurt the favorable comparison between predicted and measured S_L away from the limits, since these S_L are much more affected by branching than termination rates [54,55].

With this motivation, calculations were performed with varying $H+O_2+H_2O \rightarrow HO_2+H_2O$ rates. It was found that the rate must be decreased by a factor of about 5 to match the experimental r^{*}_{VIS}. This decrease also yields a similar improvement in the match with S_L experiments (Fig. 14a). Still, such a large change cannot readily be reconciled with other experimental data upon which the mechanisms [47,52,53] are based, thus further assessment of the appropriate rate for near-limit flames is required.

(e) Measured and predicted flame ball emission profiles

Figures 15a and 15b show comparisons of predicted and measured flame ball near-IR/visible and UV intensity profiles, respectively, for a 3.44% H_2-air mixture. The predicted near-IR/visible radius is smaller than the predicted UV radius, whereas the measured near-IR/visible radius is larger than the measured UV radius. This behavior was observed for all mixtures. For the H_2-air mixtures, the predicted UV radius is larger than the measured value, whereas the predicted near-IR/visible radius is smaller than the measured value. The discrepancy between model and experiment is less for the UV radii. Note also that the measured UV intensity decreases monotonically with increasing radial distance from the center of the ball whereas the predicted UV intensity exhibits a peak at non-zero radial distance.

This 3.44% H_2-air mixture is at the computational lean stability limit and thus is the leanest mixture for which comparisons between model and experiment can be made. The prediction of 3.44% H_2 compares reasonably well with the experimental results 3.35 ± 0.05% H_2 from earlier KC135 experiments [21] and 3.2 ± 0.1% H_2 inferred from the JAMIC tests.

Prior numerical investigations [28,29] have shown that the lean limit and the flame radii near the limit are strongly affected by the chemical mechanism and in particular the rate constants for the $H + O_2 + H_2O$□□ $HO_2 + H_2O$ recombination step, which are quite different for different published H_2-O_2 oxidation mechanisms. Improved agreement between model and experiment for both the UV and near-IR/visible radii can be obtained with a smaller rate for this reaction than that given in the GRI mechanism, though this would not change the prediction that (contrary to experiment) the UV radius is larger than the near-IR/visible radius. Of course, changes in the Planck mean absorption coefficient will also affect the predictions. Recently the accuracy of the radiation data for H_2O from Hubbard and Tien [56] has been challenged by Bedir *et al.* [57] and Ju *et al.* [58] because Hubbard and Tien used older (pre-1965) integrated band absorption coefficient data whereas high-resolution spectral data are now available [59]. Slightly better agreement between model and experiment is obtained with the Ju *et al.* [58] radiation data; the lean limit is shifted from 3.44% to 3.34% H_2 while $r^*_{OH\bullet}$ and r^*_{VIS} for the 3.44% H_2 mixture are shifted from 2.12 and 1.27 mm, respectively, with Hubbard and Tien radiation to 2.81 and 1.68 mm, respectively, with Ju *et al.* radiation.

Figures 16 shows comparisons of predicted and measured flame ball UV and near-IR/visible radii as a function of fuel concentration. The differences between these radii discussed above in relation to Fig. 15a are seen in all these data, with no effect of fuel concentration on these trends. Note that the number of UV points is sometimes lower than the number of near-IR/visible points because of the much smaller field of view for the UV camera discussed earlier. Fig. 16 shows that data obtained in all three facilities, JAMIC, KC135 [21] and space experiments [22], are quite consistent. The agreement between JAMIC and space experiments might be expected based on the earlier discussion of the time scale for development of the steady radius but it is somewhat surprising that the KC135 flame balls, which suffer from much higher acceleration levels than the JAMIC or space experiments, would exhibit nearly identical radii. Thus, UV and near-IR/visible radii are rather robust properties of flame balls.

3.4 Discussion

The results show significant differences between model and experiments, even for H_2-air mixtures where reabsorption effects are negligible [29], especially for near-IR/visible radii. Particularly surprising is that the relative sizes of UV and near-IR/visible radii are different in model predictions and experimental observations. The data obtained in all three experimental facilities are quite consistent, indicating that variations in acceleration level and experiment duration cannot account for the differences. Alternative chemical mechanisms and radiation models can account for some but seemingly not all of the discrepancy, nor can it account for the observation that the relative sizes of UV and near-IR/visible radii are different in model predictions and experimental observations. Decreasing the $H + O_2 + H_2O$□□ $HO_2 + H_2O$ rate by a factor of 5 would provide favorable comparisons between measured and predicted near-IR/visible radii in H_2-air mixtures [29], but such a large change cannot readily be reconciled with other kinetic data, would lead to a predicted lean stability limit much leaner than the experimental limit, and would adversely affect the moderate agreement between measured and predicted r^{*}_{OH*} radii shown in Fig. 16. Also, agreement between predicted total radiative emissions in H_2-air mixtures and measurements obtained in long-duration space experiments is favorable [29] and would be adversely affected by any change in the model that would increase the size of the thermal field and thus the total radiative loss.

4. Conclusions

The combustion experiments of PMMA particle-clouds were conducted in microgravity and normal gravity. In the normal gravity experiments, the propagating flame was distorted because of the turbulent flow generated by an air jet to disperse and suspend PMMA particles in air. On the other hand, in the microgravity experiments, the flame became spherical and relatively smooth because the ignition of particle clouds could be delayed until the turbulence was sufficiently decayed. Flame speeds measured by using ionization probes increased with decreasing particle diameters in microgravity. The equivalence ratios at the lean flammability limit for PMMA particle-clouds with diameters of 8.4, 13.5, 30.4, and 48.5 μm in microgravity were 0.68, 0.76, 0.86, and 1.05, respectively, being narrowed linearly as the particle diameters were increased.

By observing the spherically propagating flame of PMMA particle-cloud in microgravity, pulsating flame propagation was detected. The "pulsating flame" could be seen only near the lean flammability limit. The frequency of the pulsating flame first increased and then decreased with increasing equivalence ratio. At a higher equivalence ratio, no pulsating flames were observed. The frequency decreased with increasing particle diameter. The ranges of equivalence ratio where the pulsating flame propagation were observed are extended with increasing particle diameter. The propagation mechanisms of the pulsating flame can be explained based on the concept of heat absorption to the particle in the burned gas and radiative heat transfer to the particle in fresh mixtures. The heat absorption and the heat gain change the flame speed repeatedly, resulting in a pulsating flame. Also the mechanisms of the pulsating flame in particle-clouds were shown numerically using a simplified particle-cloud model.

Flame balls in lean H_2-air, H_2-O_2, H_2-O_2-CO_2 and H_2-O_2-SF_6 mixtures were investigated to examine the effects of varying diluents on size and radiant emission. Radial profiles of temperature, integrated heat release and integrated radiative heat loss at the dynamic stability limit were clarified. Improved chemical reaction mechanisms for near-limit H_2-O_2 oxidation may be required, particularly for the 3-body $H + O_2 + H_2O \rightarrow HO_2 + H_2O$ reaction.

Near-IR/visible and UV emission profiles of flame balls in H_2-O_2-diluent mixtures were obtained in µg experiments employing drop tower. Data for both types of emissions obtained in the drop tower, aircraft and space-based facilities were quite consistent, indicating that radius is a rather robust property of flame balls. In marked contrast to experiments, the predicted near-IR/visible flame radii were always smaller than UV radii. The magnitude of discrepancy between measured and predicted flame ball properties was lower for UV radii than near-IR/visible radii in H_2-air mixtures but higher for near-IR/visible radii in H_2-O_2-CO_2 mixtures.

The most puzzling aspect of the observations is the remarkably large size of the experimental IR radii in H_2-air mixtures compared to theoretical predictions. The magnitude of the adjustment in chemical or transport coefficients required to change the predicted temperature profiles enough to obtain agreement between model and experiment seems unjustifiable and would adversely affect the more favorable agreement with UV radii, flammability limits, and total radiative heat loss. A search for alternative sources of emissions suggested that experimental radii would be consistent with a chemiluminescence reaction of the form $HO_2 + HO_2$ □ $H_2O_2 + O_2$ producing an excited state of H_2O_2, however, no appropriate transition of $H_2O_2^*$ could be identified. These findings indicate that while a stationary flame ball is perhaps the simplest combustion system, quantitative agreement between computation and experiment has been elusive, even when using detailed chemical, transport and radiation sub-models, and thus represents a continuing modeling challenge.

REFERENCES

1. Horton, M. D., Goodson, F. P. and Smoot, L. D., Combust. Flame 28: 187 (1977).
2. Bradley, D., Habik, S. L. and Swithenbank, J. R., Twenty-First Symposium (International) on Combustion, The Combustion Institute, Pittsburgh, 1986, p. 249.
3. Slezak, S. E., Fitch, D. J., Krier, H. and Buckius, R. O., Combust. Flame 54: 103 (1983).
4. Seshadri, K., Berlad, A. L. and Tangirala, V., Combust. Flame 89: 333 (1992).
5. Kauffman, C. W., Srinath, S. R., Tezok, F. I., Nicholls, J. A. and Sichel, M., Twentieth Symposium (International) on Combustion, The Combustion Institute, Pittsburgh, 1984, p. 1701.
6. Pu, Y. K., Jarosinski, J., Johnson, V. G. and Kauffman, C. W., Twenty-Third Symposium (International) on Combustion, The Combustion Institute, Pittsburgh, 1990, p. 843.
7. Hironao Hanai, Mitsuru Ueki, Kaoru Maruta, Hideaki Kobayashi, Susumu Hasegawa and Takashi Niioka, "Lean Flammability Limit of Polymethyl-methacrylate Particle-Cloud in Microgravity," Combustion and Flame (in press).
8. Hironao Hanai, Kaoru Maruta, Hideaki Kobayashi and Takashi Niioka, "Pulsating Flame

Propagation of PMMA Particle-Cloud in Microgravity," Twenty-Seventh Symposium (International) on Combustion, The Combustion Institute, Pittsburgh (in press).

9. Kobayashi, H., Ono, N., Okuyama, Y. and Niioka, T., Twenty-Fifth Symposium (International) on Combustion, The Combustion Institute, Pittsburgh, 1994, p. 1693.
10. Okuyama, Y., Ohtomo, Y., Maruta, K., Kobayashi, H. and Niioka, T., Twenty-Sixth Symposium (International) on Combustion, The Combustion Institute, Pittsburgh, 1996, p. 1369.
11. Ballal, D. R., Proc. R. Soc. Lond. A385: 21 (1983).
12. Hegde, U., Ross, H. D. and Facca, L. T., *Combust. Sci. Technol.* 94: 279-294, (1993).
13. Peraldi, O., Landry, C., Lee, J. H. and Knystautas, R., *Fourteenth International Colloquium on Dynamics of Explosions and Reactive System*, University of Coimbra, Portugal, (1993).
14. Krazinski, J. L., Buckius, R. O. and Krier, H., Prog. Energy Combust. Sci. 5: 31 (1979).
15. Joulin, G. and Deshaies, B., *Combust. Sci. Technol.* 47: 299-315, (1986).
16. Joulin, G., *Combust. Sci. Technol.* 52: 377-395, (1987).
17. Joulin, G. and Cambray P., *Combust. Sci. Technol.* 52: 397-412, (1987).
18. Buckmaster, J. and Agarwal, A., *Combust. Sci. Technol.* 103: 191-206, (1994).
19. Buckmaster, J. and Jackson, T. L., *Combust. Sci. Technol.* 103: 299-313, (1994).
20. Ronney, P. D., *Combust. Flame* 82:1-14 (1990).
21. Ronney, P. D., Whaling, K.N., Abbud-Madrid, A., Gatto, J.L., Pisowicz, V.L., *AIAA J.* 32:569-577 (1994).
22. Ronney, P. D., Wu, M.-S., Pearlman, H.G., Weiland, K.J., *AIAA Journal*, to appear (1998).
23. Buckmaster, J. D., Joulin, G., Ronney, P. D., *Combust. Flame*, 79:381-392 (1990).
24. Buckmaster, J. D., Joulin, G., Ronney, P. D., *Combust. Flame* 84:411-422 (1991).
25. Lee, C., Buckmaster, J. D., *SIAM J. Appl. Math.* 51:1315-1326 (1991)
26. Buckmaster, J. D., Smooke, M.D., Giovangigli, V., *Combust. Flame* 94:113-124 (1993).
27. Smooke, M.D., Ern, A. NASA Conference Publication 10174, pp. 445-450 (1995).
28. Wu, M.-S., Ronney, P. D., *Combust. Flame* , to appear (1998).
29. Wu, M.-S., Liu, J.-B., Ronney, P. D., *Twenty-Seventh Symposium (International) on Combustion*, to appear (1998).
30. Buckmaster, J. D., Smooke, M. D., Giovangigli, V., *Combust. Flame* 94:113-124 (1993).
31. Smoot, L. D., Horton, M. D. and Williams, G. A., Sixteenth Symposium (International) on Combustion, The Combustion Institute, Pittsburgh, 1977, p. 375.
32. Horton, M. D., Goodson, F. P. and Smoot, L. D., Combust. Flame 28: 187 (1977).
33. Peraldi, O., Lee, J. H., Knystautas, R., Landry, C., Gregorio, P. and Shemie, M., 14th International Colloquium on Dynamics of Explosions and Reactive Systems, University of Coimbra, Portugal, 1993.
34. Mizutani, Y. and Ogasawara, M., Int. J. Heat Mass Transfer 8: 921 (1965).
35. Hertzberg, M. and Zlochower, I. A., Twenty-Third Symposium (International) on Combustion, The Combustion Institute, Pittsburgh, 1990, p. 1247.

36. Hertzberg, M., Cashdollar, K. L., Ng, D. L. and Conti, R. S., Nineteenth Symposium (International) on Combustion, The Combustion Institute, Pittsburgh, 1982, p. 1169.
37. Zhen, G. and Leuckel, W., "Effect of Igniter and Turbulence on Dust Explosions", Proceedings of the Seventh International Colloquium on Dust Explosions, Christian Michelsen Research AS, Bergen, Norway, 1996.
38. Chiu, H. H., Kim, H. Y. and Croke, E. J., Nineteen*th Symposium (International) on Combustion*, The Combustion Institute, Pittsburgh, PA, 1982, pp. 971-980.
39. Joulin, G. and Deshaies, B., *Combust. Sci. Technol.* 47: 299-315, (1986).
40. Joulin, G., *Combust. Sci. Technol.* 52: 377-395, (1987).
41. Joulin, G. and Cambray P., *Combust. Sci. Technol.* 52: 397-412, (1987).
42. Buckmaster, J. and Agarwal, A., *Combust. Sci. Technol.* 103: 191-206, (1994).
43. Buckmaster, J. and Jackson, T. L., *Combust. Sci. Technol.* 103: 299-313, (1994).
44. Ronney, P. D., *Combust. Flame* 62:120-132 (1985).
45. Rogg, B., in: *Reduced Kinetic Mechanisms for Applications in Combustion Systems*, Appendix C, Springer-Verlag, Berlin-Heidelberg, 1993.
46. Rogg, B., "RUN-1DL: The Cambridge Universal Flamelet Computer Code," User Manual, 1993.
47. Frenklach, M., *et al.*, "An Optimized Kinetics Model for Natural Gas Combustion," *25th Symposium (International) on Combustion*, Poster 26, 1994.
48. Fenimore, C., Jones, G., *Combust. Flame* 8:231-234 (1964).
49. Wray, K. L., Feldman, E. V., *Fourteenth Symposium (International) on Combustion*, Combustion Institute, Pittsburgh, 1972, pp. 229-238.
50. Hubbard, G. L., Tien, C. L., *J. Heat Trans.* 100:235-239 (1978).
51. Dunn, D.S., Scanlon, K., Overend, J., *Spectrochimica Acta* 38A:841-847 (1982).
52. Yetter, R.A., Dryer, F. L., Rabitz, H., *Combust. Sci. Tech.* 79:97-128 (1991).
53. Peters, N., in: *Reduced Kinetic Mechanisms for Applications in Combustion Systems*, Chapters 1 and 5, Springer-Verlag, Berlin-Heidelberg, 1993.
54. Coffee, T.P. and Heimerl, J.M., *Combust. Flame* 50:323-340 (1983).
55. Egolfopoulos, F.N. and Law, C.K., *Twenty-Third Symposium (International) on Combustion*, Combustion Institute, Pittsburgh, 1990, pp. 413-421.
56. Hubbard, G. L., Tien, C. L., *J. Heat Trans.* 100:235-239 (1978).
57. Bedir, H., Tien, J. S., Lee, H. S., *Combust. Theory Modeling* 1:395-404 (1997).
58. Ju, Y., Guo, H., Liu, F., manuscript in review (1998).
59. Rothman, L. S., *et al.*, *J. Quant. Spectros. Radiat. Trans.* 48:469-507 (1992).

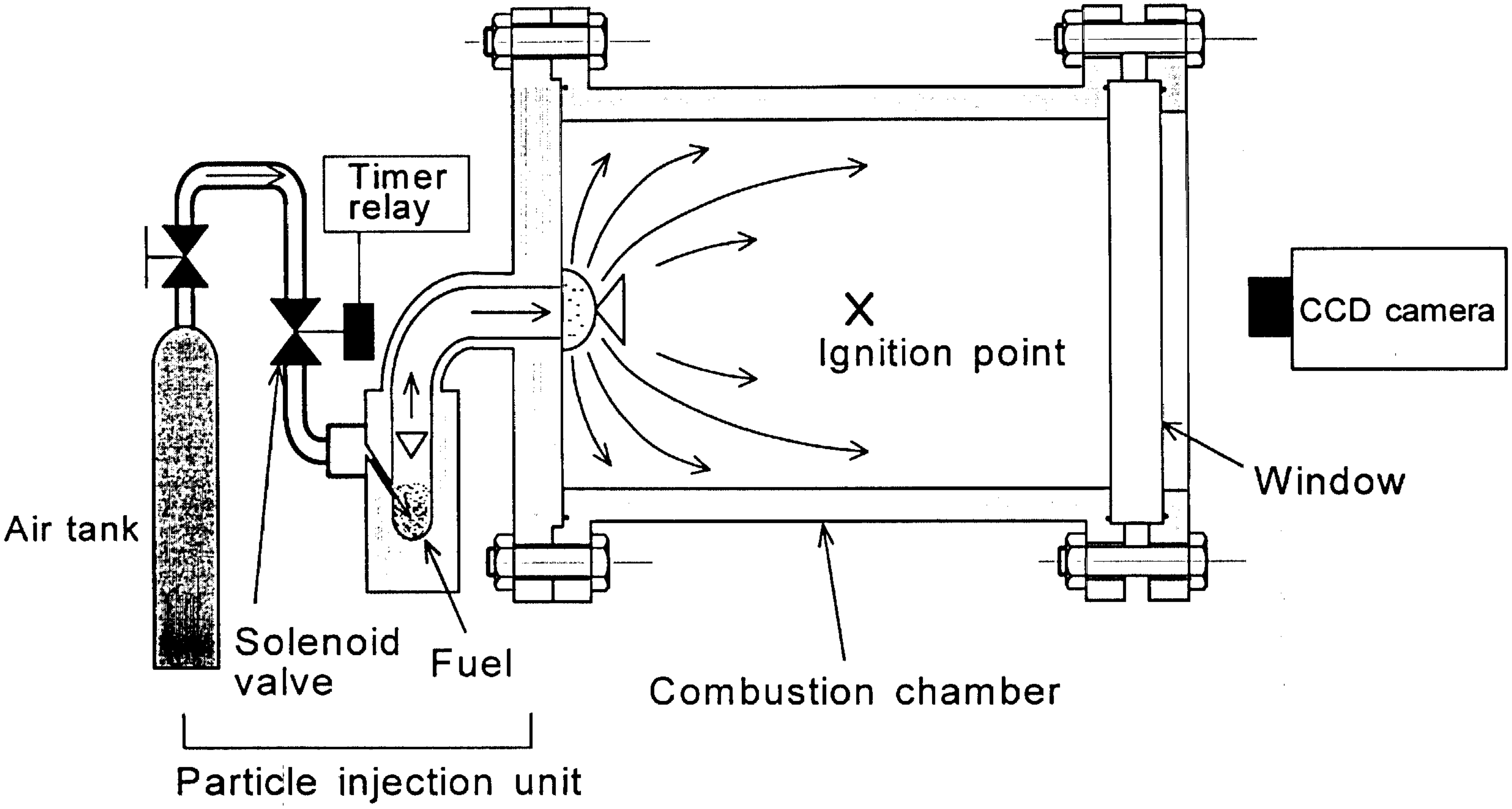

Fig. 1 Schematic diagram of experimental apparatus

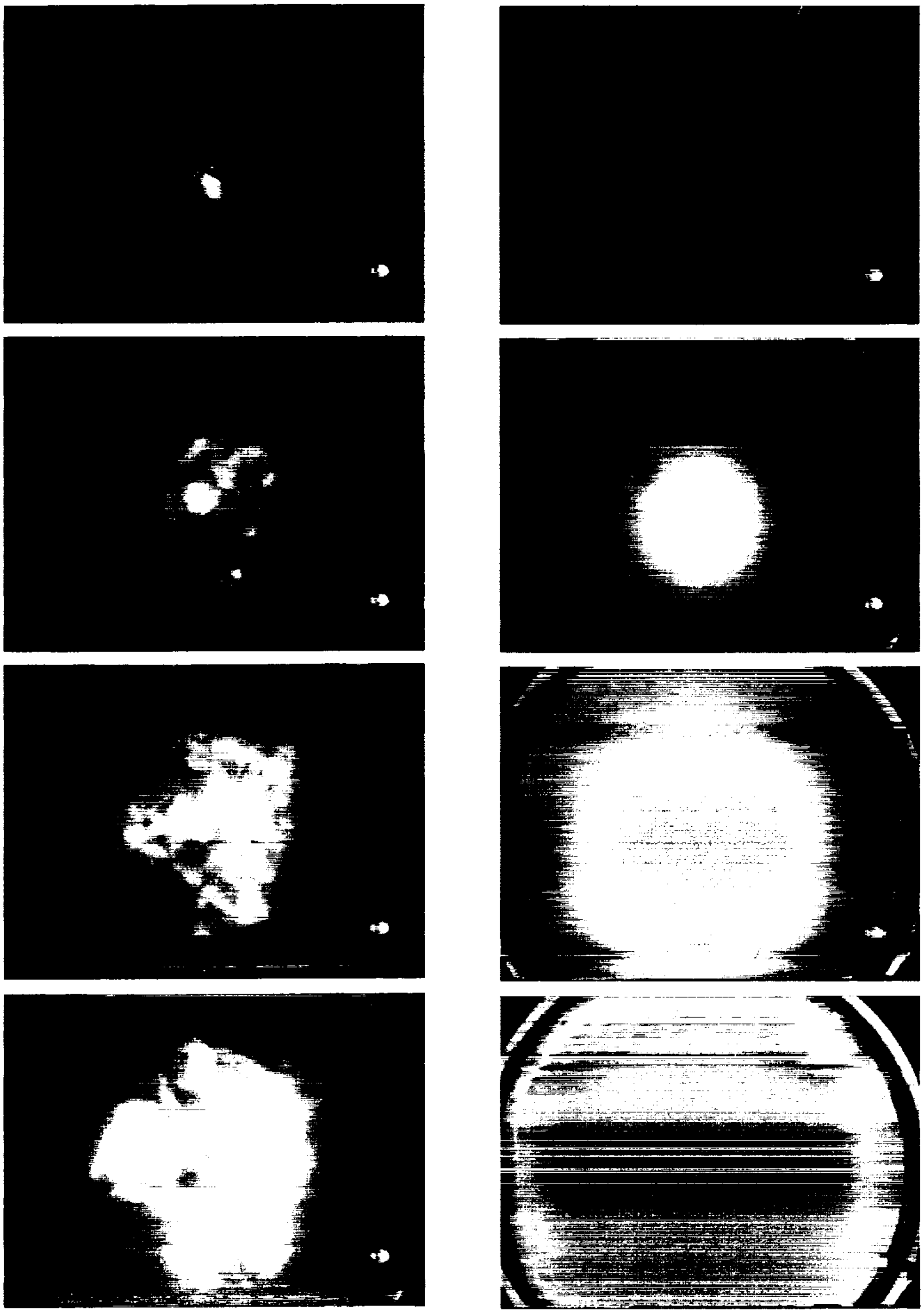

(a) Normal gravity (b) Microgravity

Fig. 2 Photographs of propagation flames:
(a) normal gravity and (b) microgravity

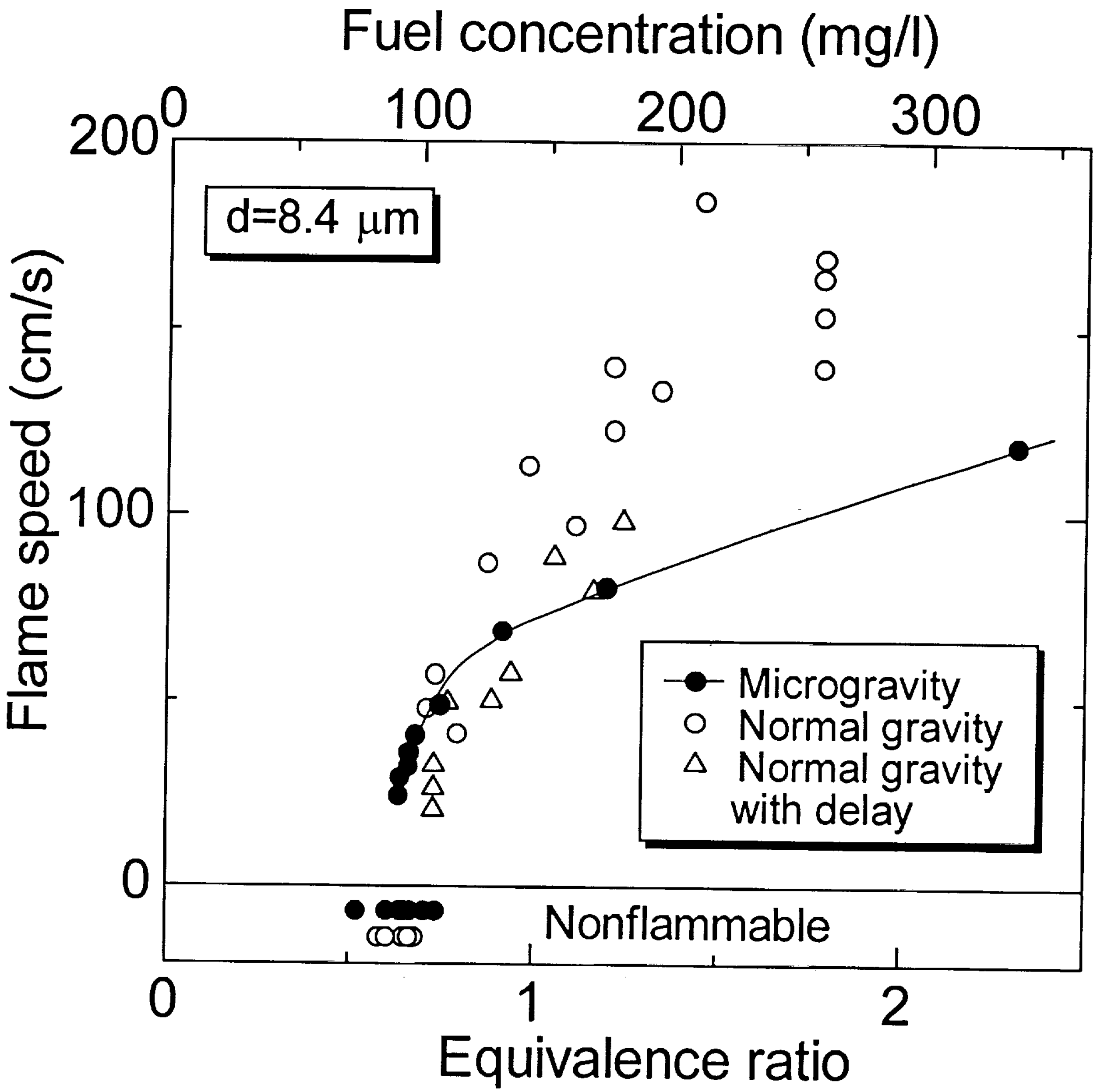

Fig. 3 Flame speed as a function of equivalence ratio in microgravity and in normal gravity

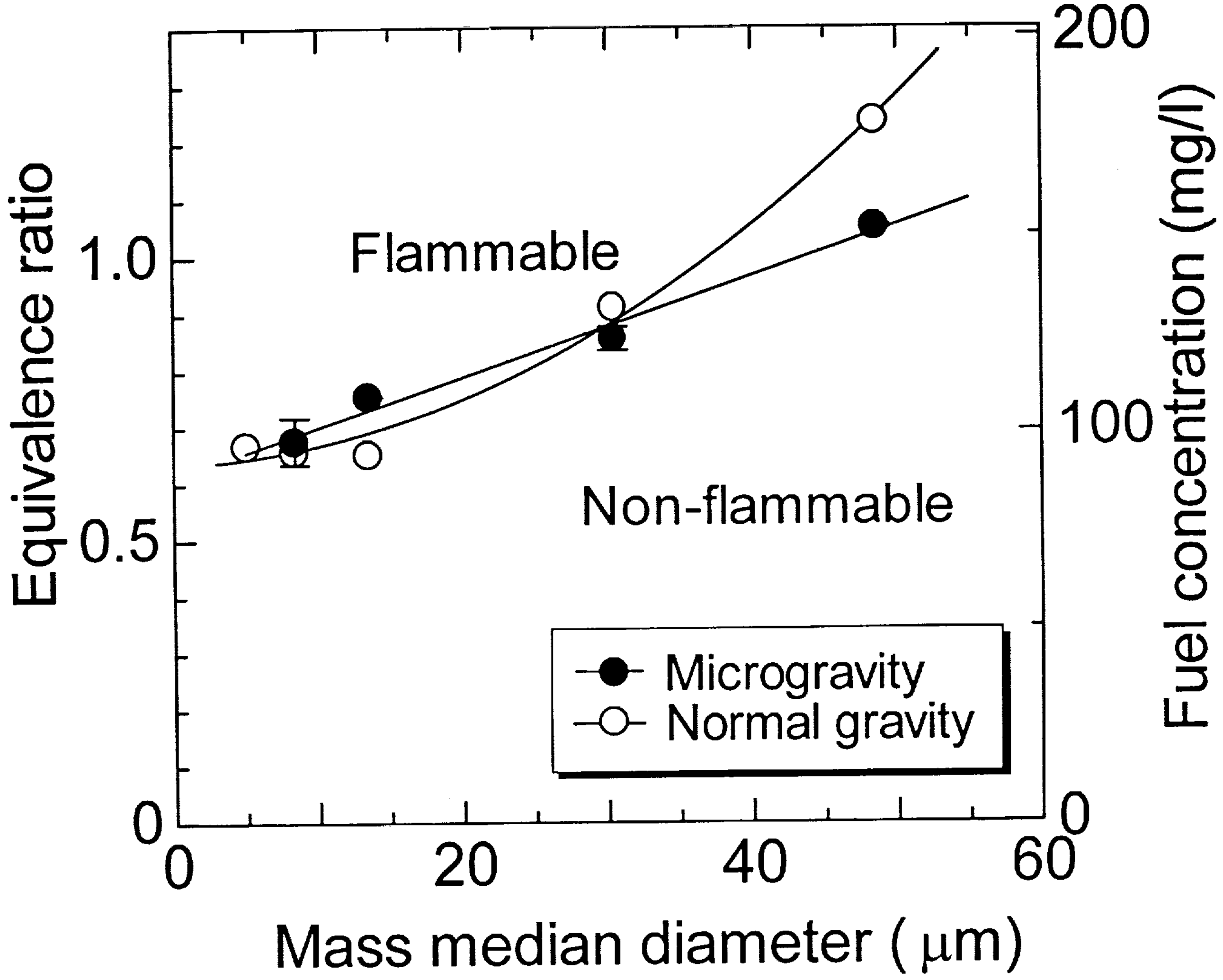

Fig. 4 Effect of mass median diameter on lean flammability limit in microgravity and normal gravity

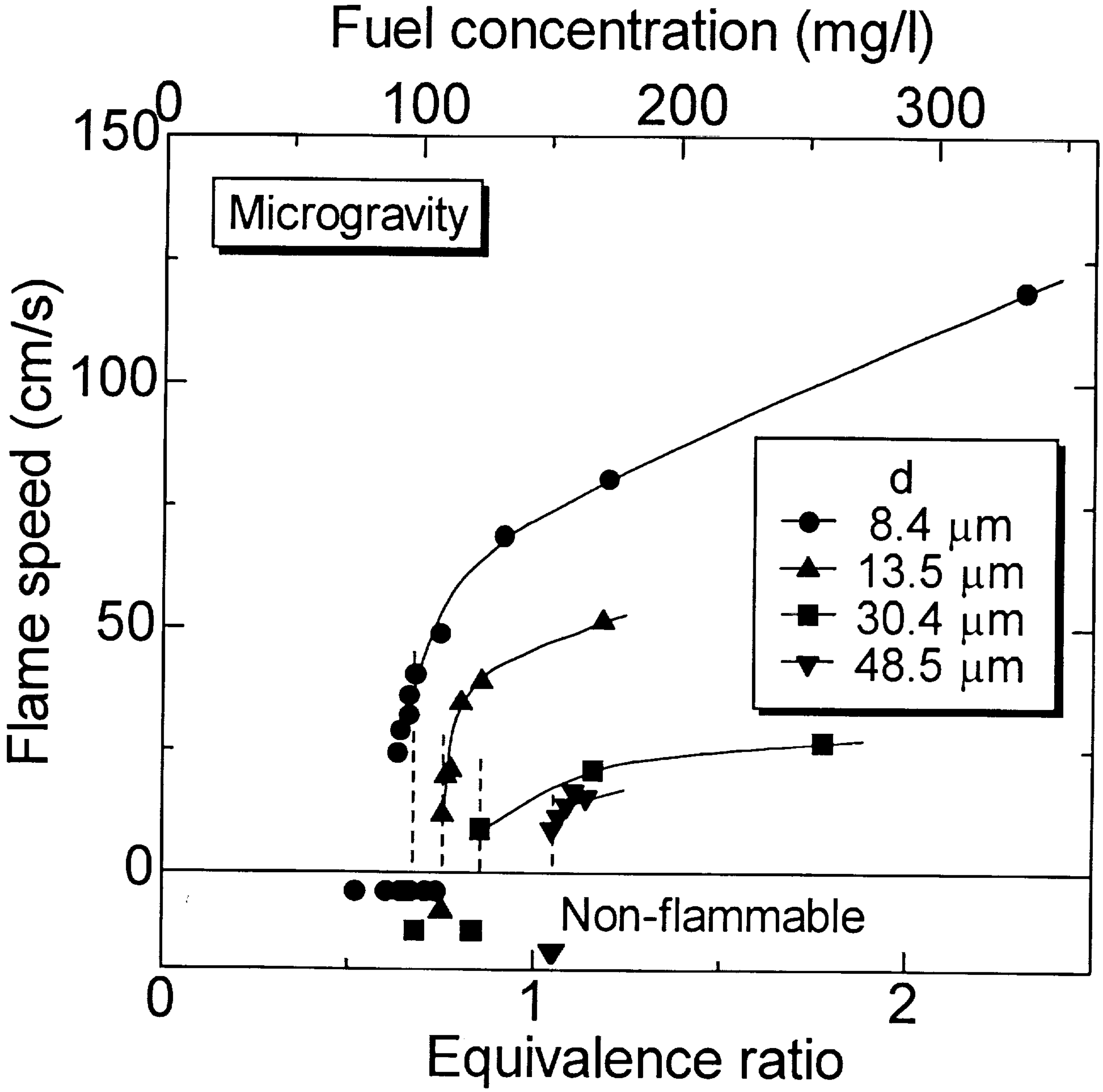

Fig. 5 Flame speed as a function of equivalence ratio and particle diameter in microgravity

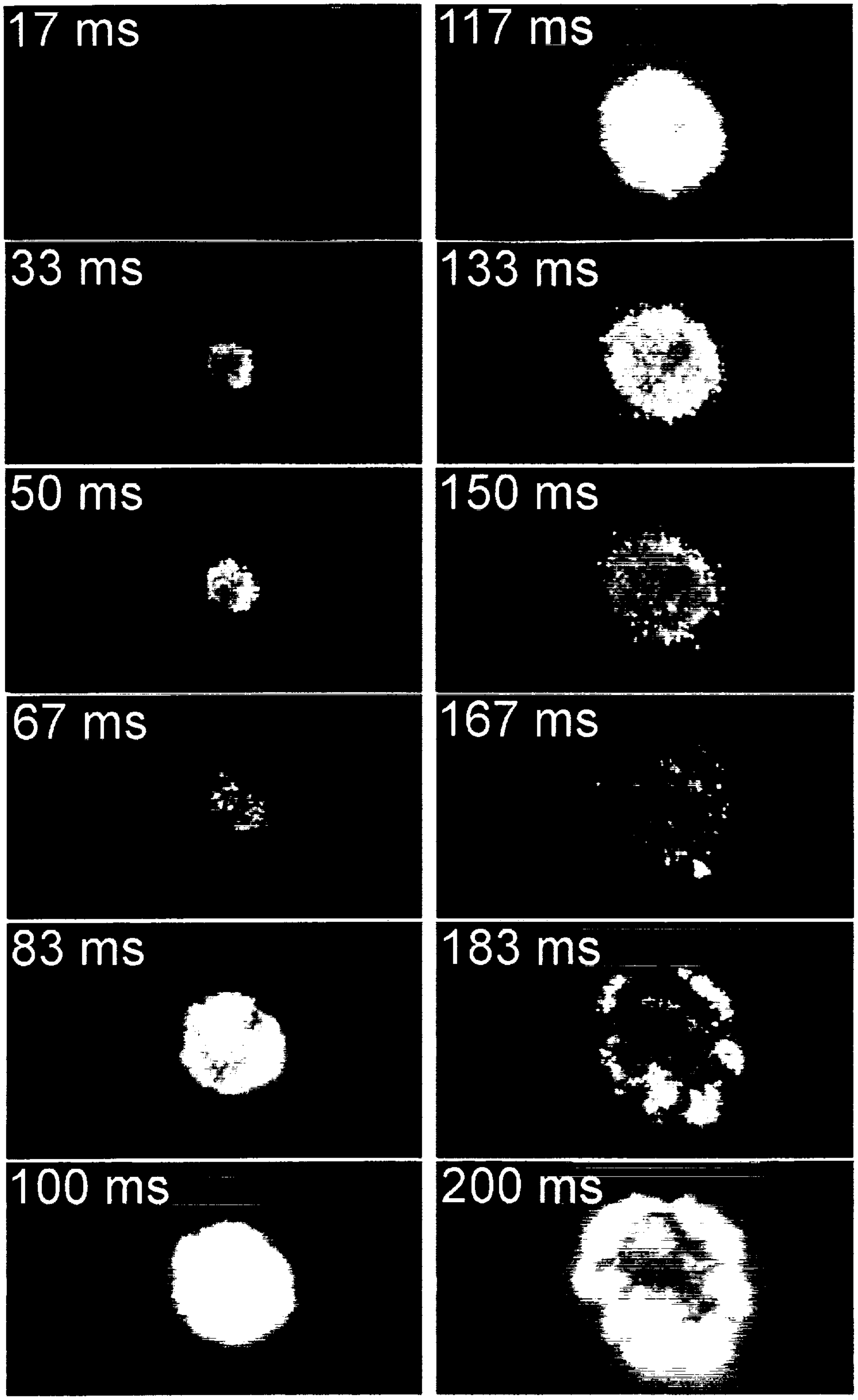

Fig. 6 Photographs of pulsating flame

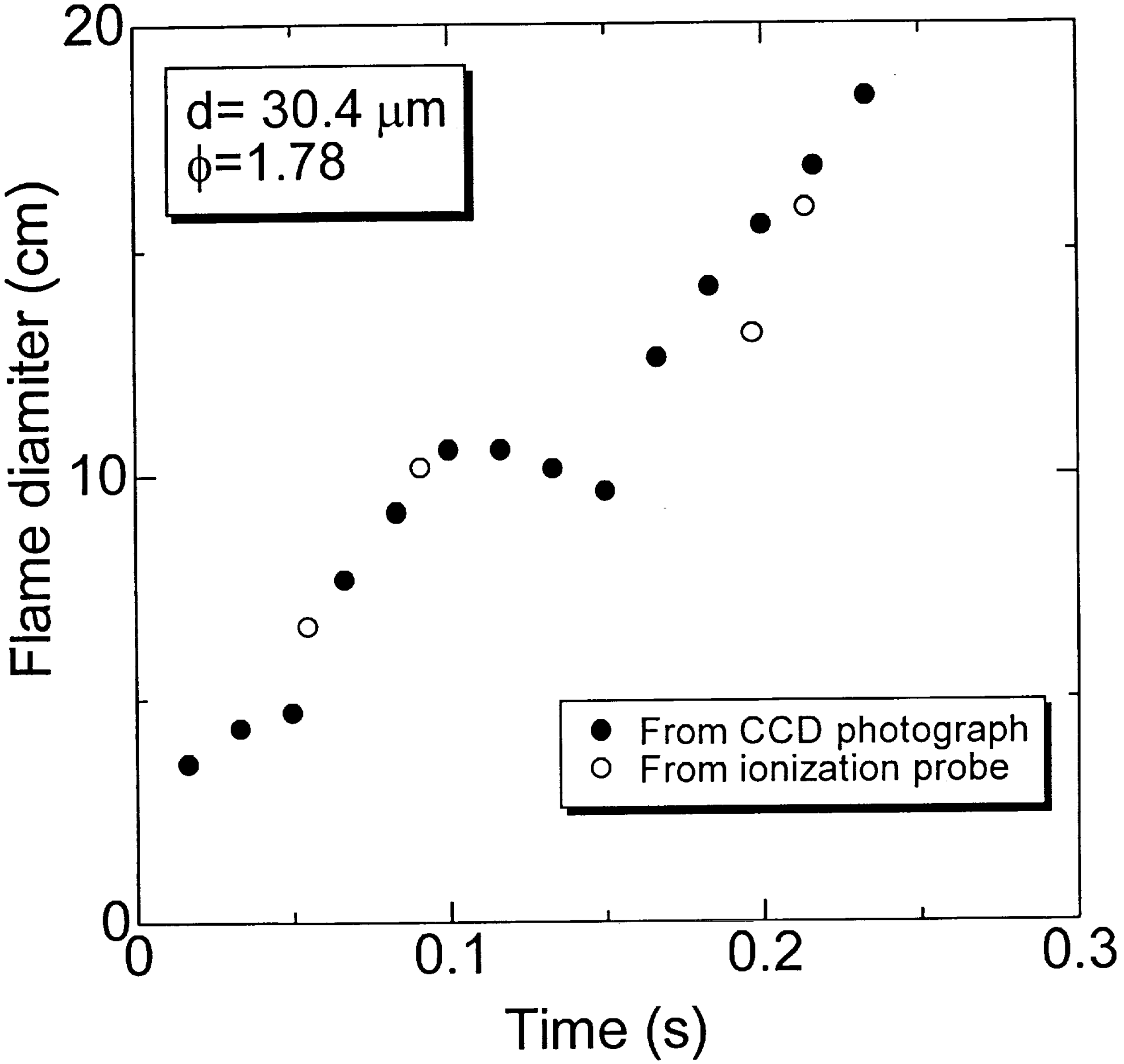

Fig. 7 Movement of the pulsating flame front

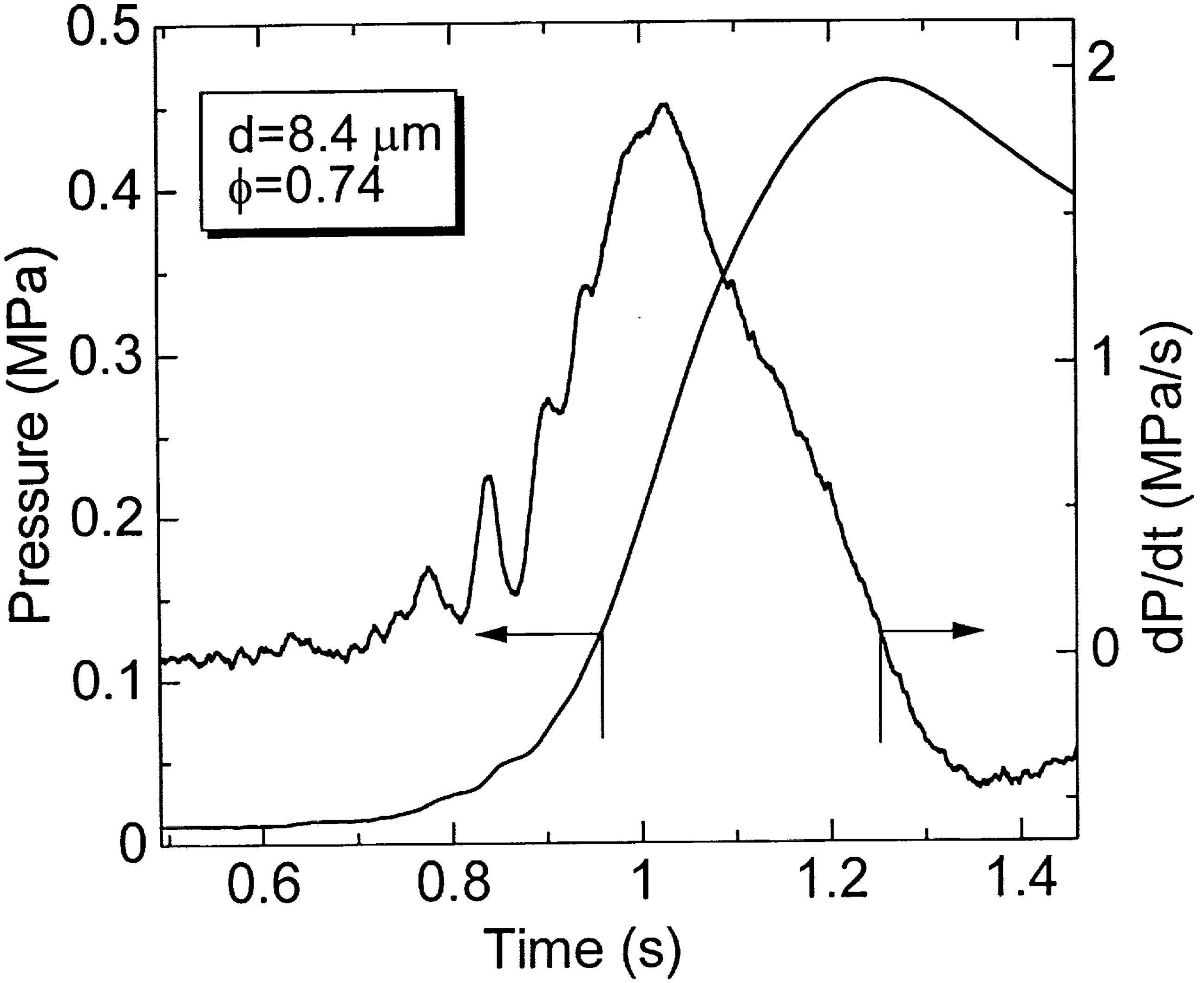

Fig. 8 Time histories of pressure and gradient of pressure rise

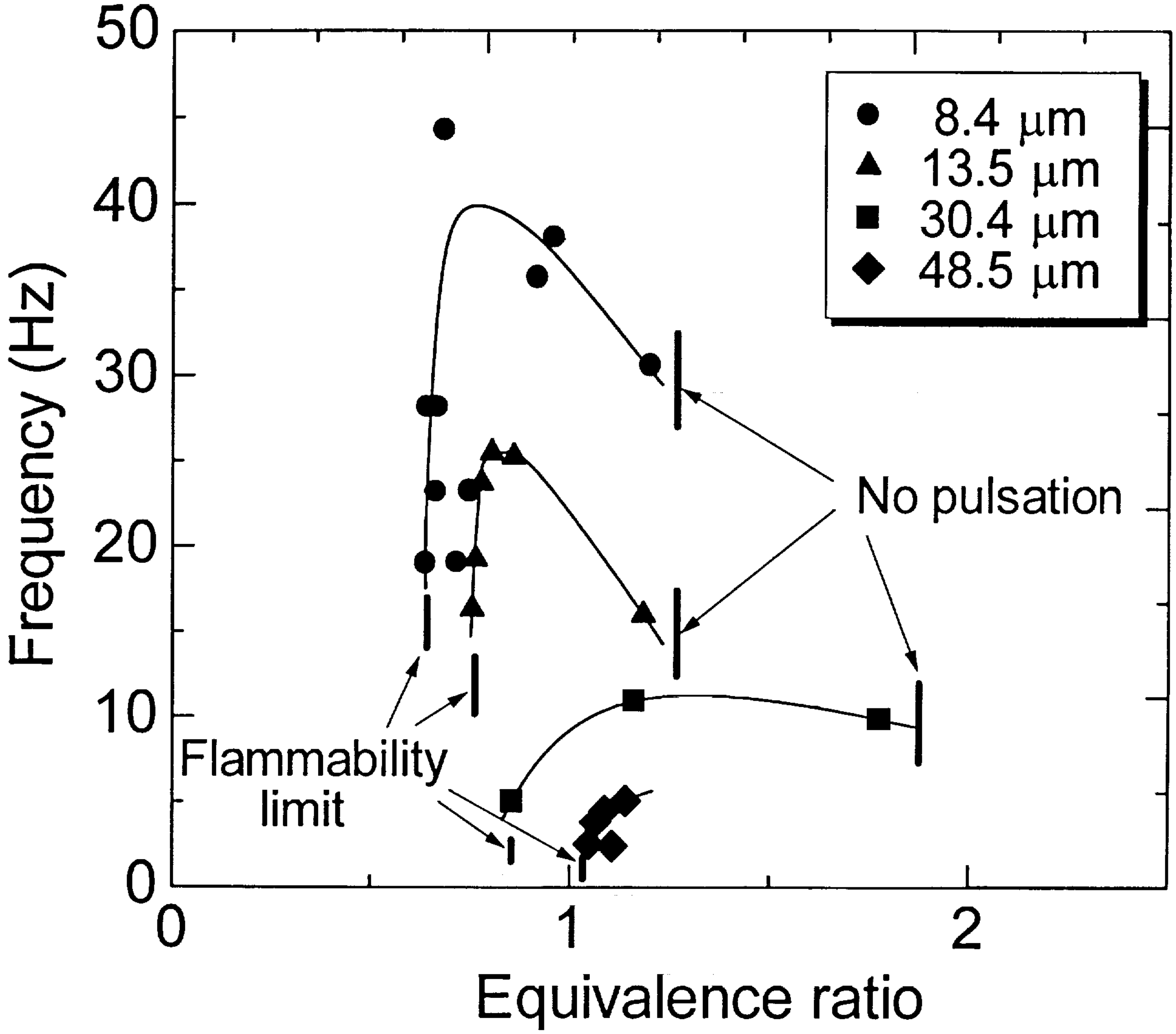

Fig. 9 Frequency of pulsating flame as a function of equivalence ratio and particle diameter

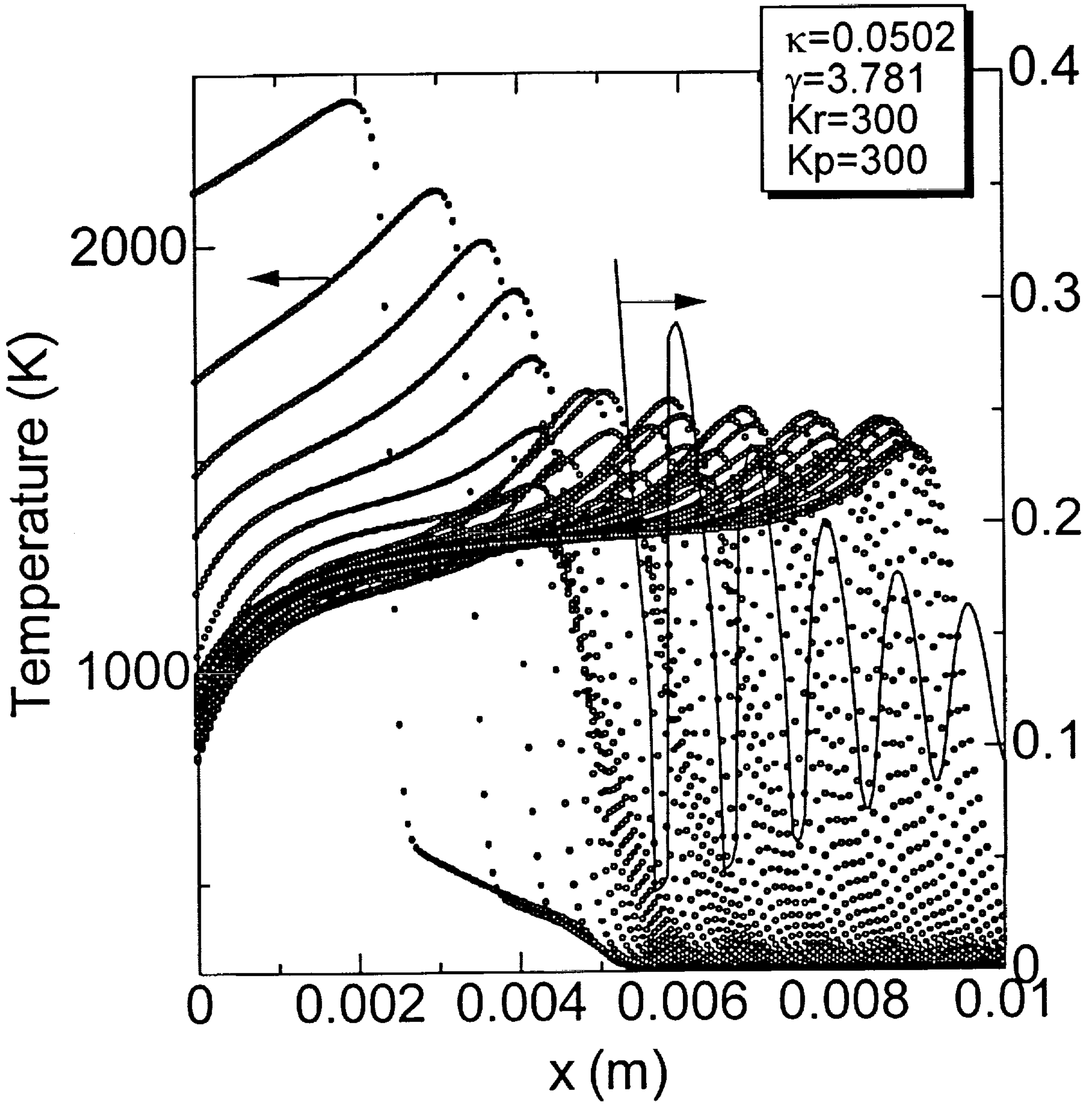

Fig.10 Temperature profiles and burning velocity of pulsating flame

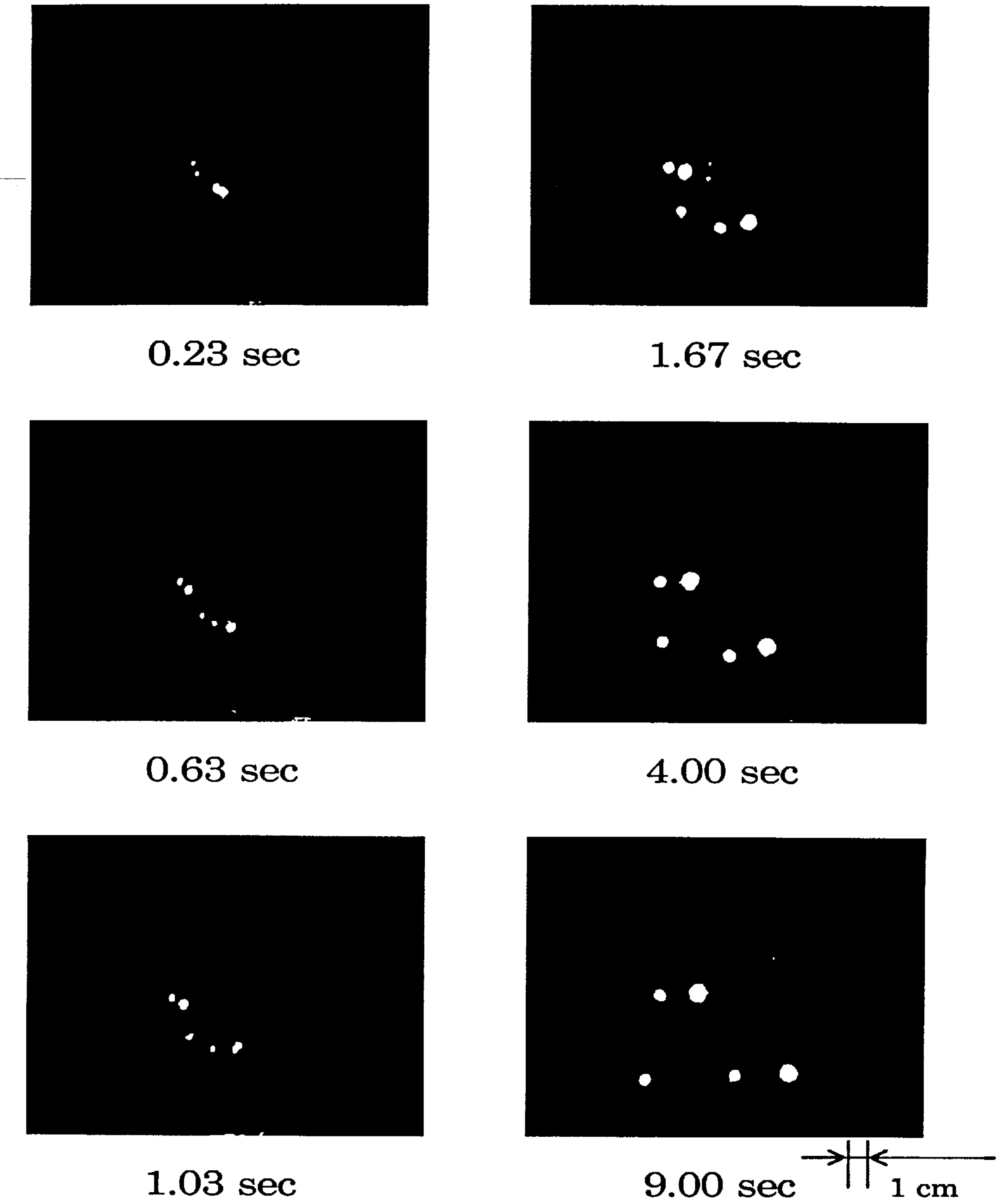

0.23 sec

1.67 sec

0.63 sec

4.00 sec

1.03 sec

9.00 sec

Fig. 11 OH-image photographs for H_2-air

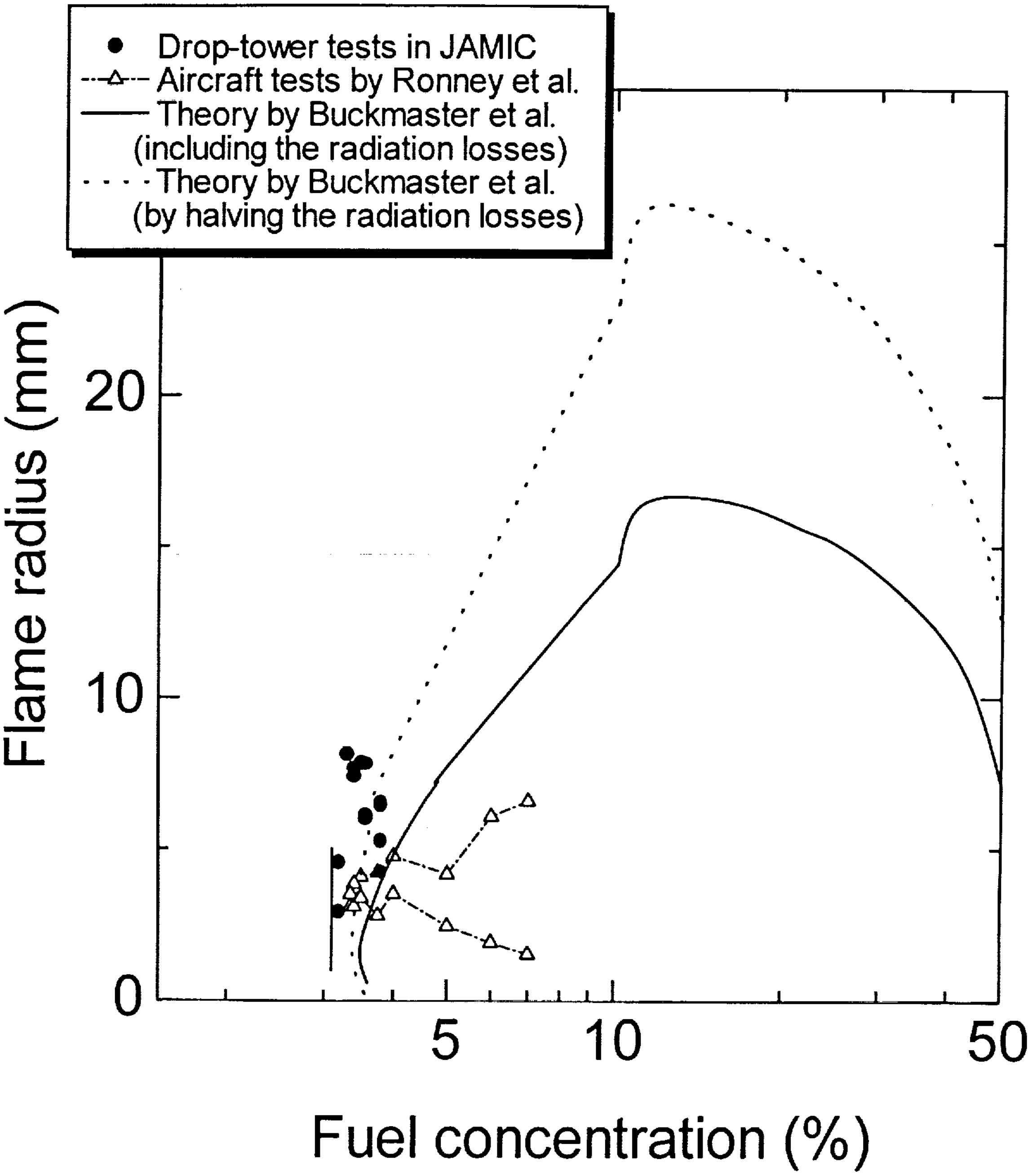

Fig. 12 Variation of the flame ball radius with fuel concentration for H_2-air

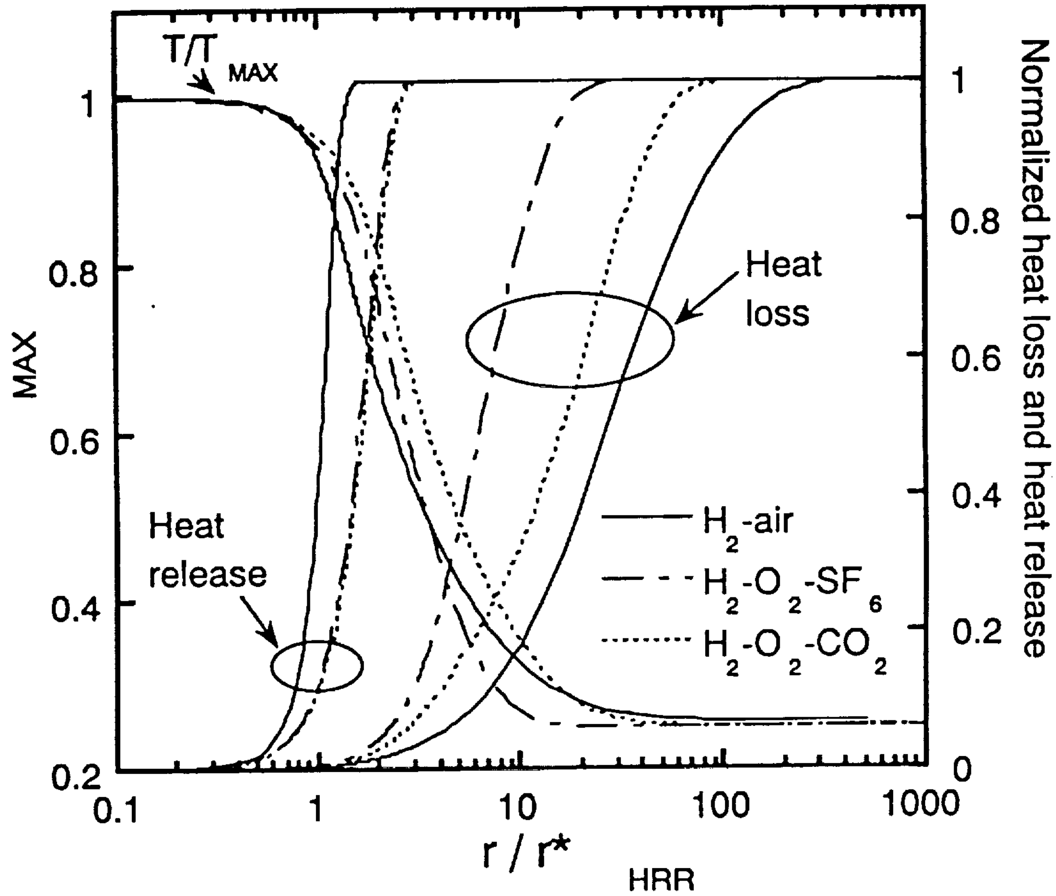

Fig. 13 Profiles of temperature, integrated heat release and integrated heat loss profiles for steady flame balls in H_2-air, H_2-0_2-CO_2 and H_2-0_2-SF_6 mixtures at the dynamic stability limit

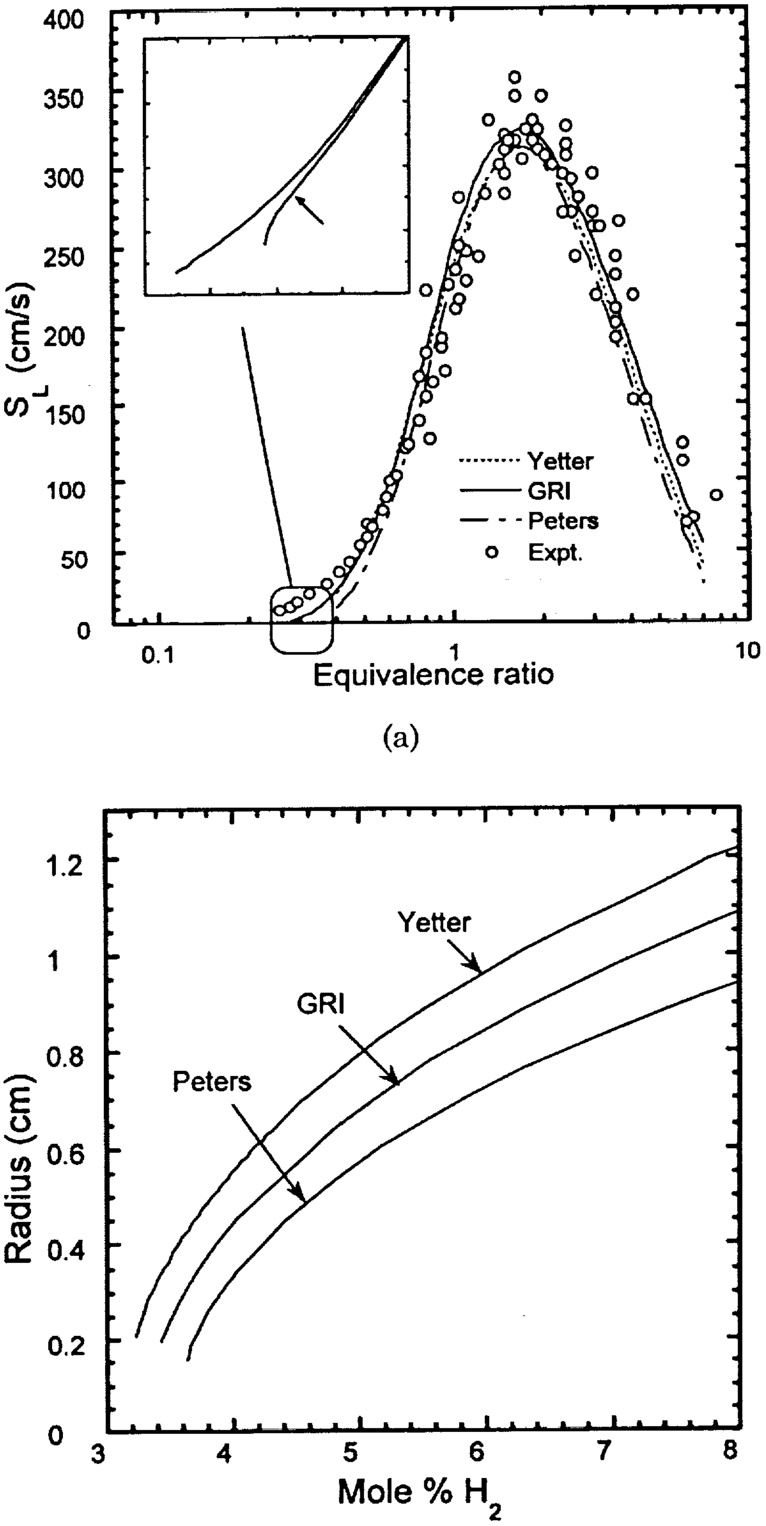

(a)

(b)

Fig. 14 Comparison of computed flame properties for 3 different H2-O2 chemical mechanisms [47,52,53]: (a) Burning velocity as a function of ϕ in H2-air mixtures and (b) r^*_{HRR} as a function of X_{H2} for steady flame balls in H_2-air mixture

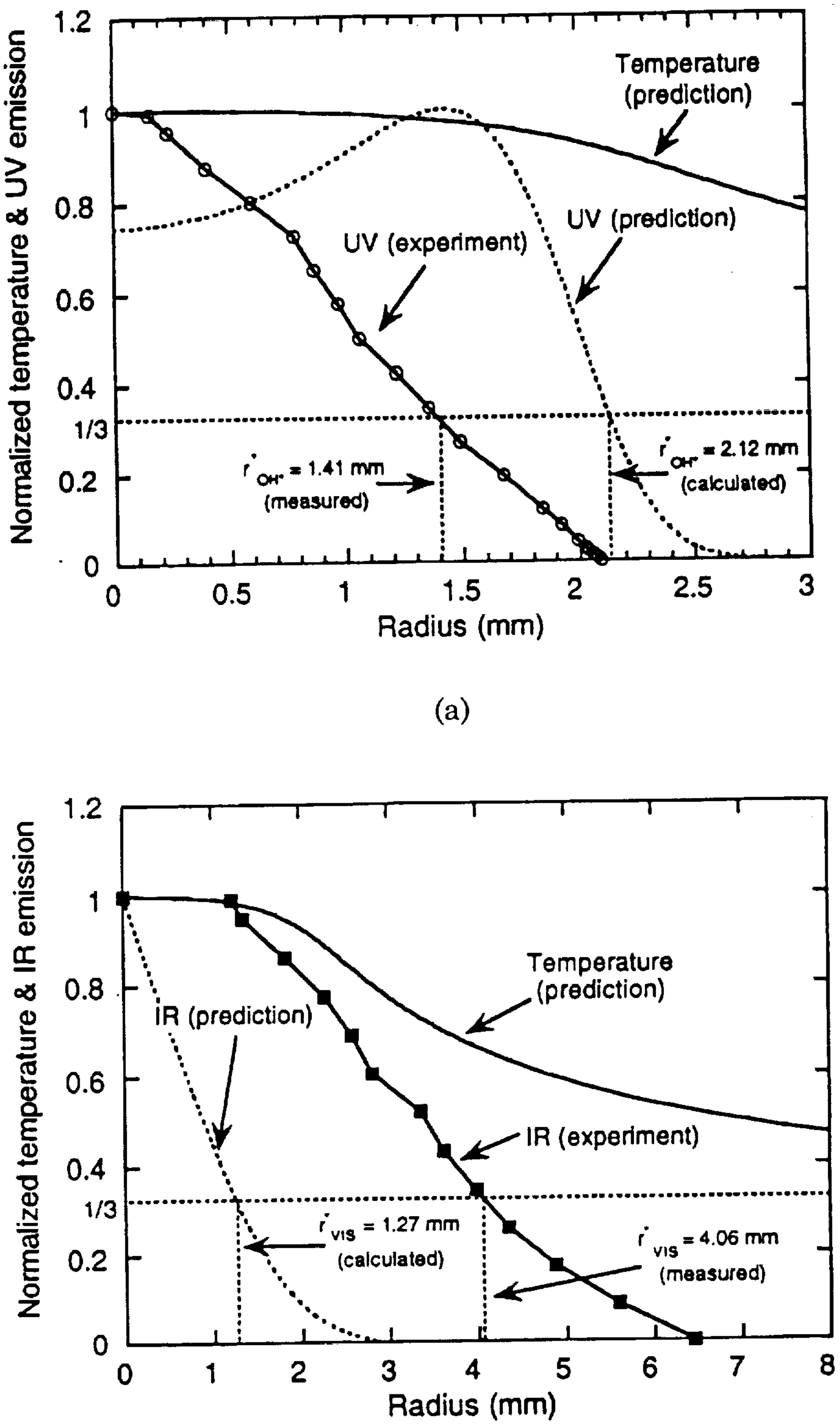

(a)

(b)

Fig. 15 Measured and predicted (Abel-transformed) flame ball emission profiles, H_2 in air :
(a) UV emissions and (b) near-IR/visible emissions

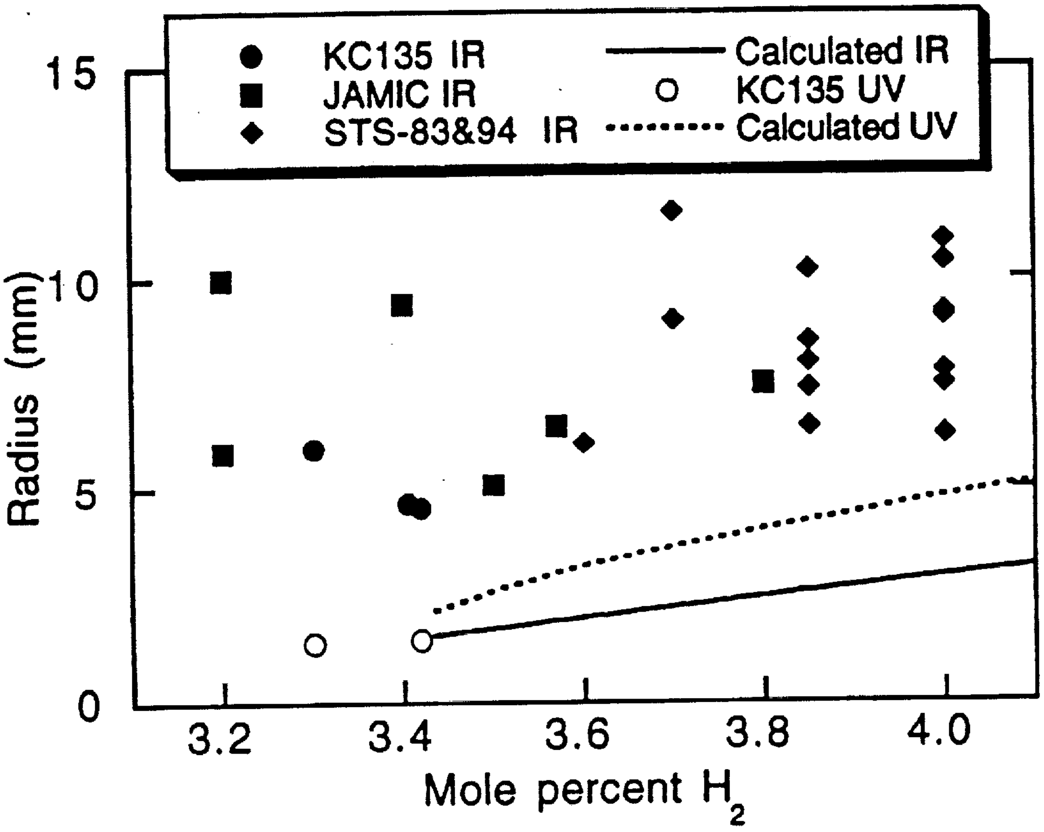

Fig. 16 Comparison of predicted (Abel-transformed) flame ball radii along with measured values from JAMIC, KC135 and preliminary results from the STS-83 and STS-94 space flight experiments, H2-air mixture

Experiments and Model Development for Investigation of Sooting and Radiation Effects in Droplet Combustion

Toshisuke Hirano, Ritsu Dobashi, Masataro Suzuki (The University of Tokyo)
Frederic Dryer (Princeton University)
Mun Choi (Univeristy of Illinois)

(1) BACKGROUND

Based on recent observations in microgravity experiments performed in support of the current effort, it appears that the formation and lingering presence of soot within the fuel-rich region of isolated droplets can modify the burning rate, flame structure, extinction and the effective thermophysical properties. The numerical model we propose to extend to include sooting has already shown that radiative effects from gas-phase species can modify burning rate and extinction properties. Clearly, radiative effects from soot which is more prevalent must produce corresponding, if not greater, influence. The complex nature of sooting and radiation effects have not been fully elucidated, nor have models which reproduce experimental behavior or serve to identify and rank important processes been developed. Thus, controversy and disagreements still surround the quantitative and even qualitative influence of sooting and attendant radiation on droplet burning behavior.

Microgravity droplet combustion is an ideal platform for advancing our understanding of the influence of sooting and radiation on combustion behavior. As opposed to other configurations, the rate of burning for droplet combustion is intimately coupled to the magnitude of sooting and radiation flux. For example, the rate at which fuel issues from a porous sphere burner, or from axi-symmetric jets and counterflow burners is ***not*** affected by the magnitude of sooting and attendant radiation. Experimental measurements and numerical modeling for droplet combustion provides a robust test of this important interaction on burning rate, flame structure, and flame extinction without affecting geometrical dimensional considerations. Isolated droplet combustion in μg also provides the flexibility to vary the residence time over a wide range (residence time is an important and desirable parameter adjustment for studying soot processes) by changing the droplet size and/or environmental parameters (pressure, inert, oxygen index). Finally, chemical composition, temperature, convection, soot particle drag, diffusion and thermophoresis are all radially oriented. Because of the geometric simplicity, particle temperature and spatial history are well defined, and robust models of each of the processes can be developed in great detail without overwhelming computational resources. In comparison, gas-jet diffusion flames under μg conditions display two dimensional particle pathlines dependent on fuel flowrate and are non-linearly coupled to sooting parameters. Thus, accurate descriptions of forces acting on soot particles, particle temperature history, etc. are more difficult to define, and considerably greater computational resources (with likely, more simplified sub-model descriptions to compensate) will be required for comparison with experiments and parametric sensitivity studies.

Droplet combustion theories devoid of sooting and/or radiation effects have recently been validated by constraining or eliminating sooting processes experimentally. For example, methanol, a fuel which does not produce soot under any conditions, is under study as part of the DCE program and has already received attention in drop tower and shuttle glovebox experiments. These studies have contributed immensely to advancing our knowledge of gas phase diffusive combustion processes including spectral radiation. In other recent experiments using n-heptane as fuel, sooting was experimentally attenuated by reducing pressure, oxygen index, and employing helium as inert for comparison with numerical model with no soot mechanisms. None of the techniques for reducing sooting have been successful however, sooting remains a critical component in the analysis of n-heptane combustion, commensurate with its importance in the burning of conventional fuels. There is growing sentiment that sooting in droplet combustion must no longer be neglected and that "perhaps one of the most important outstanding contributions of μg droplet combustion is the observation that in the absence of asymmetrical forced and natural convection, a soot shell is formed between the droplet surface and the flame, exerting an influence on the droplet combustion response far greater than previously recognized".

The scientific objectives of this collaborative work are to elucidate unresolved issues related to sooting and accompanying radiation effects in the simple, spherically-symmetric geometrical configuration of isolated droplet burning in microgravity. This configuration is an ideal platform for advancing understanding of diffusion flames in general and those involving soot in particular, for hydrocarbon fuels that are typical of those used in internal combustion engines and gas turbines. Recently, μg Droplet Combustion Experiments (DCE) aboard the STS-94 MSL-1 have demonstrated this configuration as a powerful and robust platform paralleling that available for one-D, pre-mixed flames. The study of larger liquid droplets in μg, combined with detailed numerical modeling provide opportunities to advance our understanding of the fundamentals of transient diffusion flames, as well as to test and validate the chemical kinetic, transport, sooting and radiation sub-models for realistic fuel systems. Refinements of these models through comparison against well-characterized experiments can yield new and important understanding, as well as sub-models that can be further simplified for implementation in more complex geometries.

The specific objectives of our proposal are to

1) Determine the influence of sooting and radiation on droplet burning rates. Investigate the influence of initial droplet diameter on sooting behavior in droplet combustion configuration for a wide range of conditions.
2) Define the influence of sooting and radiation on flame dynamics and structure.
3) Further elucidate through both experiments and modeling the mechanisms through which sooting affects the extinction of droplet flames.
4) Develop and validate numerical models (inclusive of sooting and radiation effects) using accurate and reliable experimental measurements. The numerical model will serve not only as a useful predictive and analytical tool, but as a skeletal model against which simplifications of various submodels can be evaluated.
5) Determine the effects of parameter adjustments (pressure, oxygen, inert, etc.) on sooting and burning behavior.
6) Test current models of thermophoretic transport and sootshell formation.
7) Study the influence of flame residence time on the physical morphology of soot.

The proposed program would continue and extend the earlier studies using n-heptane as fuel, and additionally we propose to include ethanol as a second fuel for our studies. The use of n-heptane is synergistic with other studies that have used this fuel, both as a pure fuel and as a binary mixture component. However, ethanol has some unique qualities as a fuel which make it ideal for the study of sooting issues. In particular, ethanol does not soot at combustion pressures near one atmosphere, but soots profusely as the ambient pressure is raised to pressures near three atmospheres. These pressures are much more compatible with vapor pressure characteristics of the fuel and achieving less perturbations of soot derived in the droplet ignition process. In addition, the chemical kinetics of oxidation are simpler, and the transport, and thermochemical properties of the fuel and species produced during its combustion are better defined than those for n-heptane. These differences offer significant advantages in developing robust numerical models for droplet combustion which include sooting phenomena.

Shaw [1988] first reported the formation of a truly spherically-symmetric sootshell formed within the region bounded by the droplet and the flame. **Figure 1a,b** displays photographs of the soot-containing region and then luminous flame for a n-heptane droplet burning in 1 atm air. Figure 1c is a schematic of a soot shell surrounding the droplet. The current understanding of soot shell formation suggests that soot particles formed near the flame front are acted upon by viscous drag (caused by Stefan flow), thermophoresis and diffusion. The balance of the various transport mechanisms causes the transient accumulation of soot particles and the formation of a spherical soot shell on the fuel-rich side of the diffusion flame. **Jackson and Avedisian [1992]** considered a soot particle size-dependent model by incorporating the thermophoretic formulation developed by **Talbot et al. [1980]** to analyze the formation of the soot shell. In this approach, the non-dimensional drag force was given by

$$F_D = \left(\frac{F'_D}{(F'_D)r = r_d}\right)\left[\frac{1}{r_p/\lambda + 1.20 + 0.41\exp\left(-0.88 r_p/\lambda\right)}\right] \qquad (1)$$

where

$$F'_D = \frac{6\pi\mu r_p^{2}\upsilon_g}{\lambda} = 3\sqrt{8\pi}r_p^{2}\left(\frac{R}{T}\sum\frac{Y_i}{W_i}\right)^{1/2}\frac{K\rho t r_d}{8r^2} \qquad (2)$$

The non-dimensional thermophoretic force is given by

$$F_{th} = \left(\frac{F'_D}{(F'_D)r = r_d}\right)\frac{16 r_d \mu}{K\rho_l}\left(\frac{dT}{dr}\right)\left[\frac{C_t C_s}{\left(\frac{r_p}{\lambda} + 3C_m\right)\left(\frac{r_p}{\lambda} + 2C_t\right)}\right] \qquad (3)$$

where √θ is the mean free path and r_p is considered to be the soot radius. The empirical constants are C_s which is the thermal slip coefficient (assumed to be around ~1.2) and C_t which is the kinetic theory coefficient for temperature jump at interface (assumed to be around ~2.2). Although diffusion was neglected in this analysis, future detailed modeling of sootshell formation can include the transport of soot by using the diffusion coefficient:

$$D = \frac{3}{2}\left[\frac{kT}{4r_p 2\rho\sqrt{\frac{2\pi RT}{W}}\left(1 + \frac{\pi}{8}\right)}\right] \qquad (4)$$

where r_p is the characteristic dimension of soot. The non-dimensionalized radius is defined as

$$\xi = \left(\frac{r - r_d}{r_f - r_d}\right) \qquad (5)$$

where r_f and r_d are the instantaneous flame and droplet radii, respectively. The non-dimensionalized net force, ζ is shown in **Figure 2** for a variety of soot particle size, r_p. Negative net forces will induce particle motion towards the droplet while positive net force pushes particles towards the flame. Position #1 (where ζ is equal to zero) is defined as a stable region of soot shell whereas position #2 (ζ is equal to zero) is considered to be unstable. It is believed that small perturbations in flow near position #2 will cause particles to either move towards the soot shell or towards the flame to be oxidized. Note that the soot shell location, which is defined as the radius for which ζ is equal to zero, increases with the size of the soot particles. This suggests that particles that can grow (through surface growth and agglomeration) to large sizes by virtue of residing in the stable soot shell for a long period can be transported towards the flame since the distinction between stable and unstable region becomes blurred. Evidence of this type of behavior was observed for n-heptane droplets burning in 40% O_2/N_2 atmosphere under microgravity conditions (See **Figure 3**). After the formation of a spherically symmetric soot shell, opacity of the soot-containing region appears to diminish along the azimuthal directions resulting in the formation of large particles. The higher temperatures produced in oxygen enhanced environments will result in a smaller flame, higher temperatures and larger temperature gradients within the fuel-rich region. These factors can promote particle agglomeration.

More recently, **Dobbins et al. [1995]** suggested an alternative mechanism for the formation of sootshells. They reported that the particles within the sootshell may initially be comprised primarily of soot precursor particles. Soot precursor particles are nearly-transparent particles that are considered to be intermediate structures, chronologically forming during the transition from large PAH molecules to carbonaceous soot. The carbonaceous particles are formed through the process of carbonization. The rate of carbonization is a function of the temperature-time histories experienced by the precursor particles:

$$\Delta\tau = \left(\frac{2.303}{A}\exp\left(\frac{E}{RT}\right)\right) \tag{6}$$

where $\Delta\tau$ is the time required for 90% carbonization of soot, $A = 1.78\text{x}10^6/\text{s}$, $E = 113$ kJ/mol and R is the universal gas constant. Based on preliminary estimates of the delay time of the formation of carbonaceous materials within the sootshell, the temperature within the n-heptane droplet sootshell is believed to be ~ 1200 K. Further work characterizing the chemical and physical evolution of material is required to better understand soot formation and sootshell development in droplet combustion.

It is shown in **Figure 2** that the range in particle sizes that are considered does not significantly affect the soot shell locations. However, what is not clear is the definition of particle diameter used in the thermophoretic analysis. For example, is the characteristic dimension the primary particle size or the aggregate dimension (typically defined as the radius of gyration? **Ku et al. [1995]** performed soot sampling using thermophoretic means and subsequent transmission electron microscopy to measure soot primary particle sizes produced in laminar gaseous flames. It was found that soot particles formed microgravity are much larger than their normal-gravity counterparts. By virtue of the thermophoretic trapping of soot, particles in microgravity droplet flames experience residence times that can be significantly longer than that produced in gaseous flames. Thus, measurements for laminar flames may not suffice for droplet combustion analysis. Physical and chemical characterization of soot produced in microgravity droplet combustion flames is sparse. **Avedisian [1996]** measured particle diameters for soot produced in microgravity toluene flames. Since soot was collected ex-situ from the deposition along the walls of the chamber, the specifics regarding the residence time experienced by the soot and the location from which it emanated could not be offered. Recently, **Hua et al. [1998]** performed thermophoretic sampling measurements for hexane droplet flames in microgravity and compared to measurements in normal-gravity. **Figure 4** displays soot collected at the soot shell location at a time corresponding to $t = 0.5$ seconds after ignition. The primary particle was measured by digitizing the image and using edge identification methods. Comparisons of the measured primary particle sizes for soot produced in microgravity flames are nearly double the size of soot particles produced using the same fuel in normal-gravity (**Figure 5**). Additional studies examining the effects of long aging on the soot (while residing within the soot shell) is required to determine the effects on the physical and chemical characteristics of the soot. **Jackson and Avedisian [1994]** speculated that the growth of soot particles (within the soot shell) through surface reactions with some of the vaporized fuel as a possible mechanism for enhancing the degree of sooting. This reduces the concentration of vaporized fuel to be consumed at the flame front, thereby reducing the burning rate. Variation in the soot primary size as a function of size can be used to ascertain the magnitude of this effect. The transport of large soot particles observed in **Figure 3** tend to support this hypothesis but further study is required.

As mentioned above, thermophoretic force strongly influences the sooting behavior on droplet combustion. Japanese collaborators are studying about thromophoresis (**Toda et al. [1995, 1996, 1998], Ohnishi et al. [1997], Dobashi et al. [1998]**). Japanese collaborators are accurately measuring fundamental data of thermophoresis performing microgravity experiments. They are also examining the effects of thermophoresis on carbon particles, which are of similar composition and structure to soot particles. These results of Japanese collaborators could be of great help to understand the sooting behavior observed in this study.

(2) PURPOSE

The scientific objectives of this collaborative work are to elucidate unresolved issues related to sooting and accompanying radiation effects in the simple, spherically-symmetric geometrical configuration of isolated droplet burning in microgravity (μg). This configuration is an ideal platform for advancing understanding of diffusion flames in general and those involving soot in particular, for hydrocarbon fuels that are typical of those used in internal combustion engines and gas turbines. Recently, μg Droplet Combustion Experiments (DCE) aboard the STS-94 MSL-1 have demonstrated this configuration as a powerful and robust platform paralleling that available for one-D, pre-mixed flames. The study of larger liquid droplets in μg, combined with detailed numerical modeling provide opportunities to advance our understanding of the fundamentals of transient diffusion flames, as well as to test and validate the chemical kinetic, transport, sooting and radiation sub-models for realistic fuel systems. Refinements of these models through comparison against well-characterized experiments can yield new and important understanding, as well as sub-models which can be further simplified for implementation in more complex geometries.

The specific objectives of our proposal include,

1) Determine the influence of sooting and radiation on droplet burning rates. Fully investigate the influence of initial droplet diameter on sooting behavior in droplet combustion configuration for a wide range of conditions.
2) Define the influence of sooting and radiation on flame dynamics and structure.
3) Further elucidate through both experiments and modeling the mechanisms through which sooting affects the extinction of droplet flames.
4) Develop and validate numerical models (inclusive of sooting and radiation effects) using accurate and reliable experimental measurements. The numerical model will serve not only as a useful predictive and analytical tool, but as a skeletal model against which simplifications of various submodels can be evaluated.
5) Determine the effects of parameter adjustments (pressure, oxygen, inert, etc.) on sooting and burning behavior.
6) Test current models of thermophoretic transport and sootshell formation.
7) Study the influence of flame residence time on the physical morphology of soot.

The proposed program would continue and extend the earlier studies using n-heptane as fuel, and additionally we propose to include ethanol as a second fuel for our studies. The use of n-heptane is synergistic with other studies which have used this fuel (DCE, FSDCII), both as a pure fuel and as a binary mixture component. However, ethanol has some unique qualities as a fuel which make it ideal for the study of sooting issues. In particular, ethanol does not soot at combustion pressures near one atmosphere, but soots profusely as the ambient pressure is raised to pressures near three atmospheres. These pressures are much more compatible with vapor pressure characteristics of the fuel and achieving less perturbations of soot derived in the droplet ignition process. In addition, the chemical kinetics of oxidation are simpler, and the transport, and thermochemical properties of the fuel and species produced during its combustion are better defined than those for n-heptane. These differences offer significant advantages in developing robust numerical models for droplet combustion which include sooting phenomena.

(3) JUSTIFICATIONS

The original proposal describing the work was selected and funded as a flight definition program under NRA-93-OLMSA-01. We have submitted a renewal proposal for this work in response to NRA-97-HEDS-01, and have again requested that the work be considered for flight definition. The proposed range of droplet sizes to be studied is 1 to 5 mm in diameter, and this nearly all of this range will require extended microgravity times beyond that offered from the NASA-LeRC 2.2 sec and 5.2 sec facilities. The JAMIC facility will provide duration for observing the entire burning lifetime of the droplets in the range of 1 to 2.5 mm in diameter. The extended duration afforded by JAMIC facility will also be beneficial for observing the initial burning behavior for larger droplets (2.5 to 5 mm in diameter). The use of large droplets will improve the spatial resolution for soot concentration and temperature measurements. The extent of the flame for a 1 mm droplet burning in μg is approximately 5-6 mm whereas for a 5 mm droplet, the flame is approximately 25-30 mm. The JAMIC facility will also provide an ideal platform for performing soot sampling experiments. Soot sampling experiments must be performed for large droplets for which the disturbance created by the insertion of sampling probe is minimized. For small droplets (1 mm with attendant flame diameters of 5 to 8 mm), the soot containing region is of the same size as the sampling probe (with typical widths of 3.5 mm). The JAMIC work will also provide significant impacts on flight definition. Finally, it should be noted that DC-9 parabolic flight experiments already performed in support of this program have demonstrated that the available g-levels are not capable of producing spherically-symmetric droplet flames.

(4) TECHNICAL APPROACH

We plan to use an existing advanced diagnostic μg apparatus that was designed and implemented in the present work for interchangeable use in the 2.2 sec and 5.2 sec towers and the DC-9 aircraft. This rig is configured to measure soot volume fraction distribution (using light extinction-tomographic inversion), temperature distribution (two wavelength pyrometry-tomographic inversion), soot morphology (thermophoretic sampling-TEM analysis), droplet burning rate (high-speed shadow cinematography), flame radiation (broadband radiometer) and flame position/structure (OH chemiluminescence, CCD intensified imaging, **Figure 6, Figure 7**). All diagnostic packages have already been demonstrated to function reliably and accurately as part of the current effort. Thus only a small level of funding is requested as part of this proposal to modify the experimental rig for JAMIC operation, particularly to add and integrate portable data recording devices.

Soot Volume Fraction

The approach for soot volume fraction measurement is to use the full-field light extinction technique. In this method, line of sight extinction measurements are de-convoluted using tomographic inversion. This technique has been used extensively in support of the current project. This technique was developed at NASA-Lewis Research Center and is similar to the system used in the **Laminar Soot Processes** Experiment that was flown aboard STS-83 and STS-94.

In the full-field light extinction technique, the line of sight projection data, $P_{f_v}(x)$, which is related to the transmittance of light through the soot-containing region is measured,

$$P_{f_v}(x)=\int_{-\infty}^{\infty} f_v\left(\sqrt{x^2+y^2}\right)dy \tag{7}$$

where f_v is the soot volume fraction. The Abel transform allows the calculation of the field distribution with, $f_v(r)$, corresponding to this projection distribution with the underlying assumption that it is radially symmetric. The soot volume fraction distribution (based on extinction) is found from the measured transmission of each projection,

$$\tau_\lambda(x)=\frac{I_\lambda}{I_{\lambda_0}}(x)=\exp\left[-\frac{K_e}{\lambda}\int_{-\infty}^{\infty} f_v\left(\sqrt{x^2+y^2}\right)dy\right] \tag{8}$$

where l is the wavelength of the light source and Ke is the dimensionless extinction contact of soot. Equation (8) can be rearranged into the form of the projection value.

$$P_{f_v}(x)=-\frac{\lambda}{K_e}\ln\left(\frac{I_\lambda}{I_{\lambda_0}}\right)=\int_{-\infty}^{\infty} f_v\left(\sqrt{x^2+y^2}\right)dy \tag{9}$$

The radial soot volume fraction distribution is obtained by applying the Abel Transform matrix to the line of sight extinction measurements.

Temperature Measurement

A demonstrated approach for temperature measurement is to use line of sight flame emission data at two separate wavelengths with subsequent tomographic inversion. The ratio of the spectral emission intensity at each radial position will be used through the application of two-wavelength pyrometry. This technique is identical to that used successfully in **LSP** space-shuttle experiments. As in the **LSP** experiments, it is expected that due to the small soot particle sizes, the difference between the gas-temperature and the soot temperature will be only a few degrees. Recent addition of another fiber optic cable link in the 2.2 sec tower allowed measurements of emission at two wavelengths. Preliminary measurements of temperature were obtained for n-heptane droplets burning in μg as part of objectives of the present study. The emission from the flame was simultaneously directed to two separate CCD cameras (with narrow bandpass filters at 700 nm and 800 nm). The emission intensity at each central wavelength measured for a vertical plane corresponds to the projection value of the integrated emission.

$$P_{I_\lambda}(x) = \int_{-\infty}^{\infty} K_\lambda I_{b\lambda}\, dy \tag{10}$$

$I_{b\hat{o}}$ is Planck's function and K_l is the spectral extinction coefficient, E(m) are functions of the refractive index of soot. The projected emission values for 700 nm and 800 nm can be deconvoluted separately using the Abel technique to determine the corresponding product of ($K_{\hat{o}} I_{b\hat{o}}$) as a function of radial position. The ratio of the emissions is then used to determine the temperature using the two-wavelength pyrometry formula in eqn. (11).

$$\frac{K_{\lambda_1} I_{\lambda_1 b}}{K_{\lambda_2} I_{\lambda_2 b}} = \frac{E(m_1)}{E(m_2)} \left(\frac{\lambda_2}{\lambda_1}\right)^6 \frac{\exp(C_2/\lambda_2 T) - 1}{\exp(C_1/\lambda_1 T) - 1} \tag{11}$$

Soot Particle Sampling

Droplet combustion is unique in that the residence time for soot formation, growth and oxidation can be controlled by varying the initial size of the droplet. For droplet combustion, the residence times can last as long as the time required for the droplet to burn to completion. For this reason, measurements of soot morphology performed for other geometries (such as gaseous diffusion flames in μg) cannot be used to estimate the soot particle morphology formed in droplet flames.

Soot particles will be sampled using the thermophoretic technique during the initial period of burning at t = 0.05, 0.10 and 0.20 seconds to determine whether the sootshell is initially comprised of soot precursor particles. Subsequent sampling at 25%, 50%, 75% and 90% of time required for extinction is required to determine the changes in the physical morphology and chemical content as a result of the extended exposure to the high-temperature, reactive region. It is also required that the soot particles be sampled at various radial positions to determine if the soot particle size is the controlling factor that determines whether it will be transported towards the droplet (to form the sootshell) or towards the flame (to be oxidized).

Soot sampling experiments must be performed for large droplets for which the disturbance created by the insertion of sampling probe is minimized. For small droplets (1 to 1.5 mm with attendant flame diameters of 5 to 8 mm), the soot containing region is of the same size as the sampling probe (with typical widths of 3.5 mm). Furthermore, larger droplets also afford greater spatial resolution for investigating the variations of the soot morphology at different radial positions (locations where soot particles are formed as opposed to locations where soot particles are accumulated).

Only one sample will be obtained per experiment. Although, the droplet location will be stationary, the flame and sootshell location will be varying with time. The target position for the thermophoretic sampling device will be adjusted to match the location of the sootshell at each sampling time (the location of the sootshell for each time will be from preliminary experiments in which sampling is not performed). The radius of gyration measurements will be determined performed using a non-subjective image processing technique developed by the P.I. The primary particle size will be analyzed using a digital morphometer.

OH Chemiluminescence Measurement

Ultraviolet emission due to hydroxyl radical chemiluminescence (and the interference from soot emission) occurring within the flame is to be imaged using a Xybion intensified array CCD camera (#1) with a narrowband filter with central wavelength of 310 nm and a FWHM of 10 nm. Another Xybion camera (#2) with a narrowband filter with central wavelength of 330 nm and a FWHM of 10 nm will be used to determine emission from soot alone. After determining the calibration factor of the sensitivity between the two detection systems, the intensity distribution from camera #2 will be subtracted from the measured intensity distribution from camera #1. The resulting distribution of the line of sight projection data for OH^* chemiluminescence will be deconvoluted to provide a radial distribution of the chemiluminescence by applying a 3 point Abel deconvolution. The feasibility of this technique has been established from the previous experiments performed by the Co-I. This approach yields the instantaneous location of maximum OH^* emission which, in conjunction with detailed numerical modeling proposed in this study, will be used to define the transient flame structure.

(5) PROPOSED SCHEDULE

The U.S. group will ship the Single Droplet Combustion Droptower Experimental Rig to Japan two weeks prior to the beginning of planned experiments. The U.S. personnel will reside in Japan (two weeks for P.I. and Co-I. and four weeks for graduate students) and work with Japanese personnel in performing the following experiments for which the test matrix is shown below.

Fuel:

Concurrent experiments and model development will be performed for both heptane and ethanol. Heptane is chosen since it is a major component of practical fuels and a fuel for which extensive μg results already exist. Ethanol is chosen as a fuel for which the sooting propensity can be strongly varied by especially small increases in ambient pressure. No sooting of ethanol droplet combustion under μg conditions has been noted in recent FSDC-2 experiments or in 2.2 drop tower experiments, all at atmospheric pressure.

Initial Droplet Size:

It is required that the initial droplet diameter be varied from 1.0 to 5.0 mm in diameter in increments of 0.1 mm in the range of 1 to 2 mm (to be performed in ground-based facilities) and 0.25 mm in the range from 2 to 5 mm (to be performed in flight studies).

Ambient Pressure:

It is required that the ambient pressure be varied from 0.25 atm to 2.0 atm (in 0.25 atm increments). Our ground-based experiments in the 2.2 and 5.2 second droptowers indicates that sooting can be controlled by varying the ambient pressures. It is required to measure the pressure with a resolution of no more than 0.05 atm.

Ambient Oxygen Concentration

It is required that the oxygen concentration be varied from 15% to 50% in nitrogen (molar basis) to determine its effects on the magnitude of sooting. It is required that measurements of the actual concentration be resolved to within 0.01 mole fraction since the flame temperature and sooting propensity are sensitive to the ambient oxygen concentration.

Inert Gas Substitution:

Experiments will use nitrogen as the primary inert gas. The results can then be used for comparisons with previous experimental results that are available in the literature for n-heptane combustion. Inert gas substitution will be employed by replacing nitrogen with helium and/or by operating with nitrogen/helium mixtures. Inert gas substitution and variation is a useful approach for changing the sooting behavior and therefore serves as effective adjustment for providing database for ongoing improvements to our understanding of the relationship between sooting and burning behavior. Previous investigations indicate that sooting can be dramatically reduced by varying the oxygen concentrations in both helium and nitrogen.

(6) RESULTS

Ten drop tests have been performed at JAMIC during February 22 to 26, 1999. Data for large droplet combustion have been accumulated successfully. Now these data are being analyzed.

Bibliography:

1. Avedisian, C.T., Combustion Science and Technology Book Series (ed. by F.L. Dryer and R.F. Sawyer), Gordon and Breach, vol. 4, p.135, 1996.
2. Dobbins, R.A., Fletcher, R.A., and Lu, W., Combustion and Flame, 100:301, 1995.
3. Dobbins, R.A., Govatzidakis, G.J., Lu, W., Schwartzman, A.F. and Fletcher, R.A., Combustion Science and Technology, 121:103, 1996.
4. Hua, M., Manzello, S.L. and Choi, M.Y., 1998.
5. Jackson, G.S., Avedisian, C.T. and Yang, J.C., Int'l J. of Heat and Mass Transfer, 35:2017, 1992.
6. Ku, J.C., Griffin, D.W., Greenberg, P.S. and Roma, J., Combustion and Flame, 102:216, 1995.
7. Shaw, B.D., Dryer, F.L., Williams, F.A. and Gat, N., Combustion and Flame, 74:233, 1988.
8. Talbot, L., Cheng, R.K., Schefer, R.W. and Willis, D.R., J. Fluid Mechanics, 101:737, 1980.
9. Toda, A., Dobashi, R., Hirano, T. and Sakuraya, T., Transport Phenomena in Combustion (Edited by S.H. Chan), Vol.1, pp.467-473, Taylor & Francis (Washington, DC) 1995.
10. Toda, A., Ohi, Y., Dobashi, R., Hirano, T. and Sakuraya, T., J. Chemical Physics, 105(16):7083 1996.
11. Ohnishi, H., Toda, A., Dobashi, R., Hirano, T. and Sakuraya, Transport Phenomena in Thermal Science and Process Engineering (Edited by K.Suzuki), pp.737-741, Pacific Center of Thermal-Fluids Engineering (Hawaii) 1997.
12. R. Dobashi, Toda, A., Ohi, Y., Hirano, T. and Sakuraya, Nensho no Kagaku to Gijutu, 5(4):243 1998.
13. Toda, A., Ohnishi, H., Dobashi, R., Hirano, T. and Sakuraya, Int. J. Heat and Mass Transfer, 41(17):2710 1998.

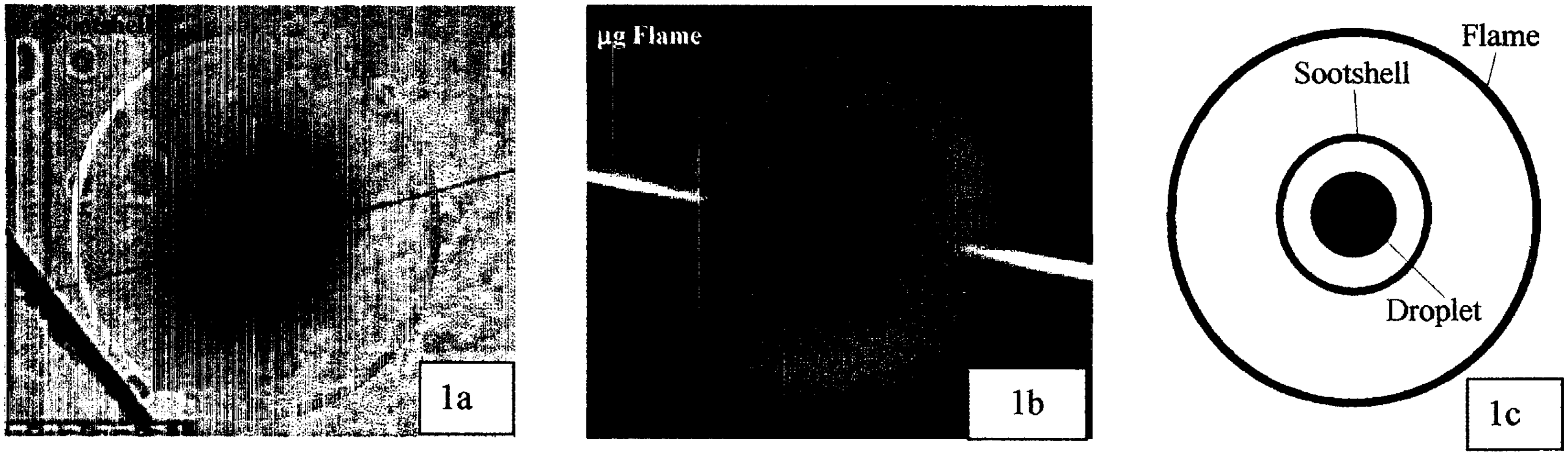

Figure 1 Images of burning droplet.

a. Sootshell and droplet
b. Flame
c. Schematic of the burning droplet

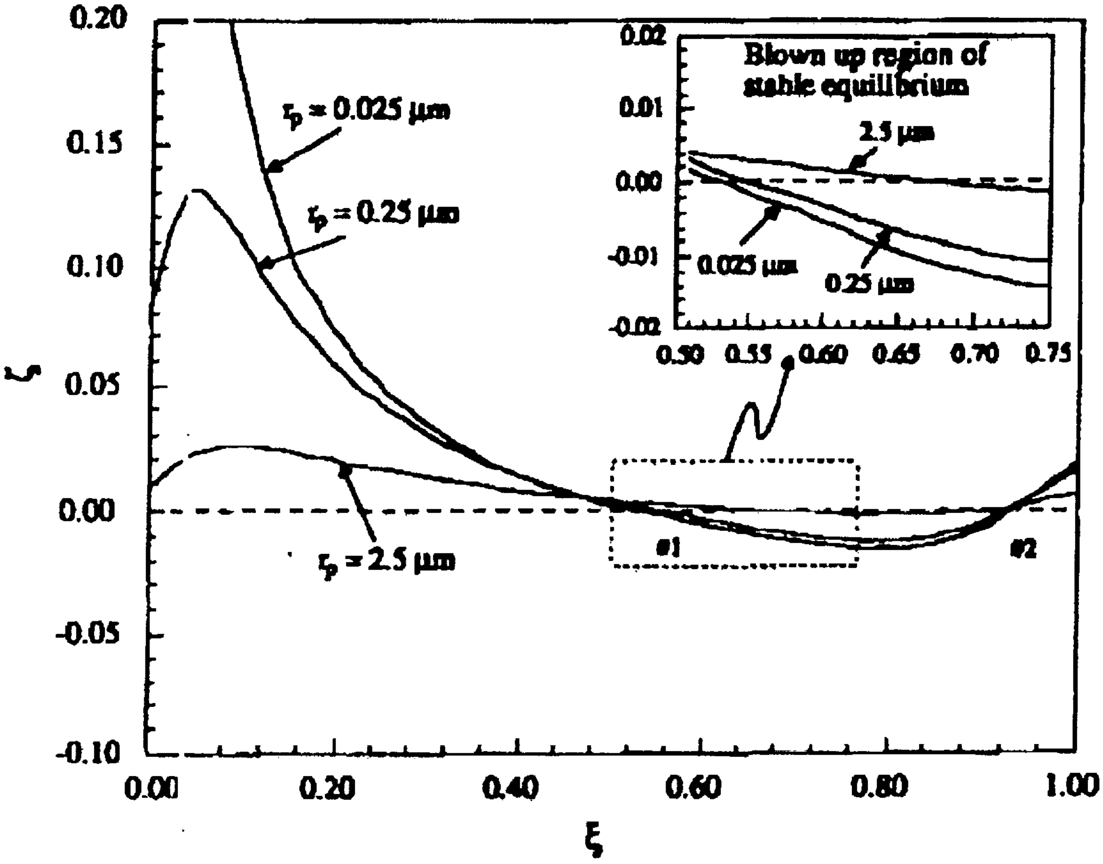

Figure 2 Variation of dimensionalized net force.

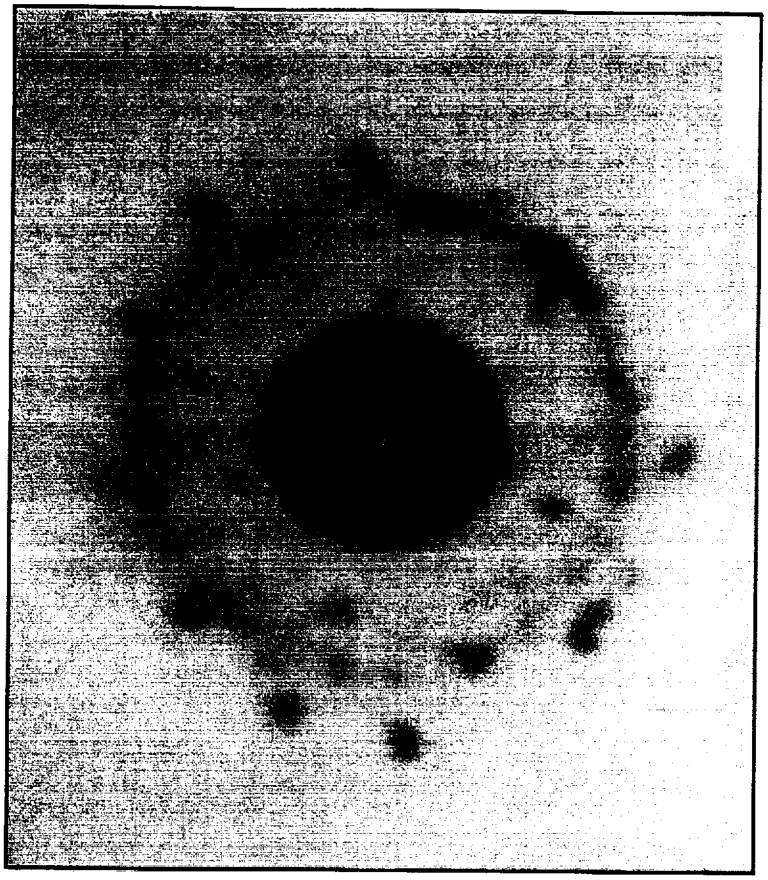

Figure 3   Sooting behavior of large-size droplet combustion.

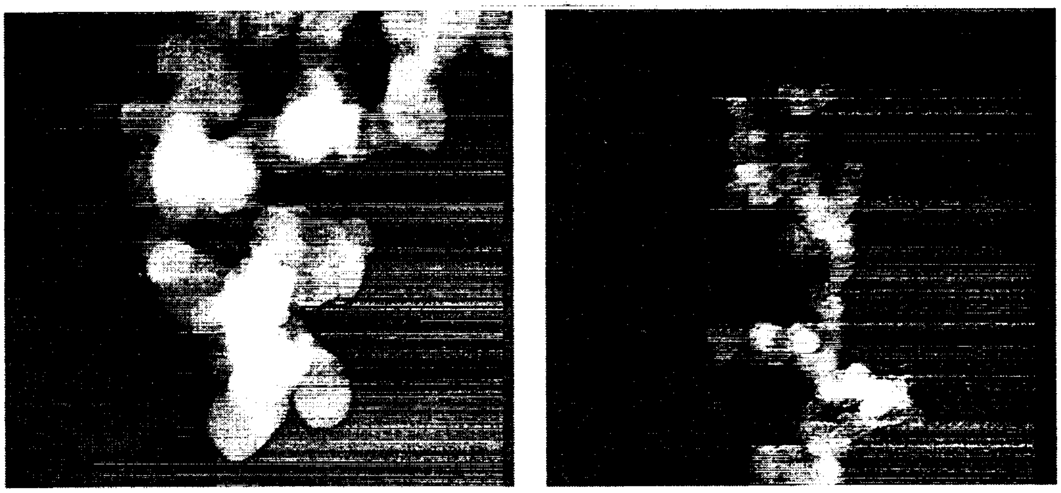

formed in microgravity

formed in normal gravity

Figure 4 Magnified photographs of collected soot particles.

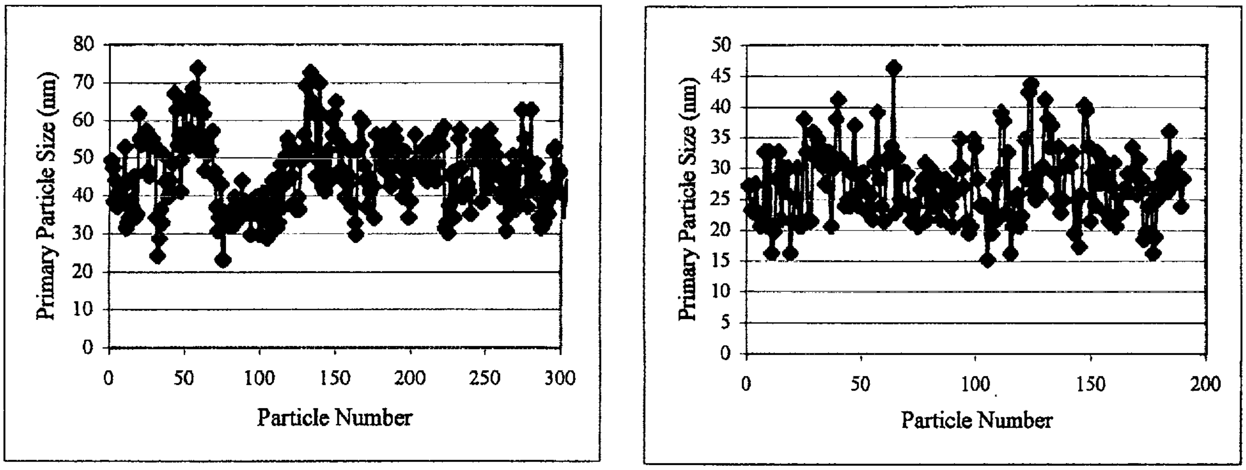

formed in microgravity

formed in normal gravity

Figure 5 Distribution of primary particle size of collected soot particles.

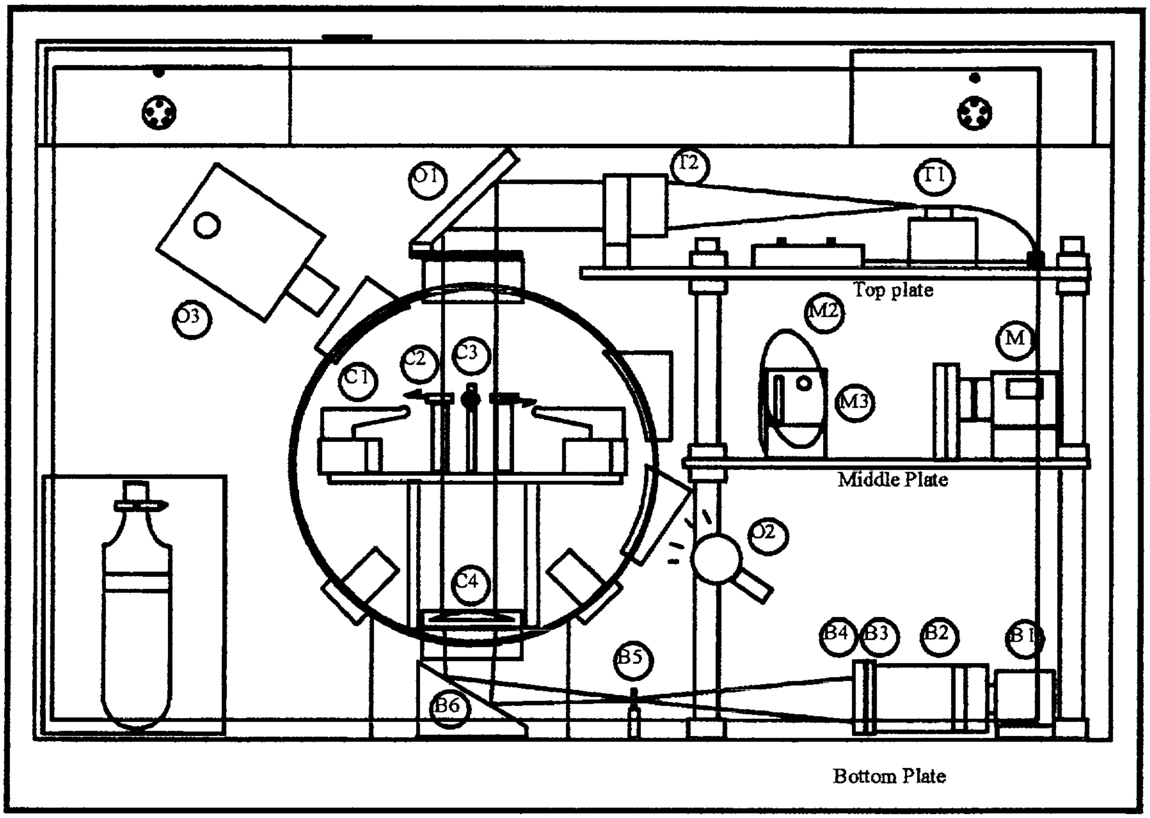

Figure 6 Schematic of experimental apparatus.

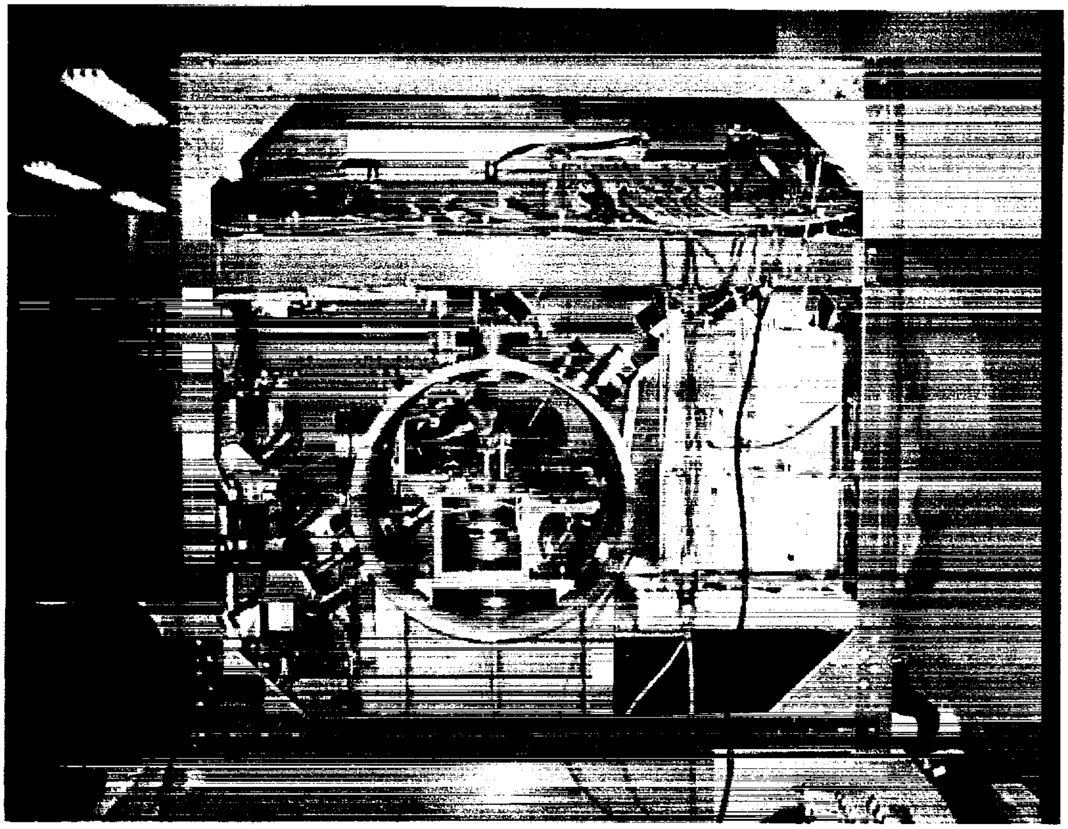

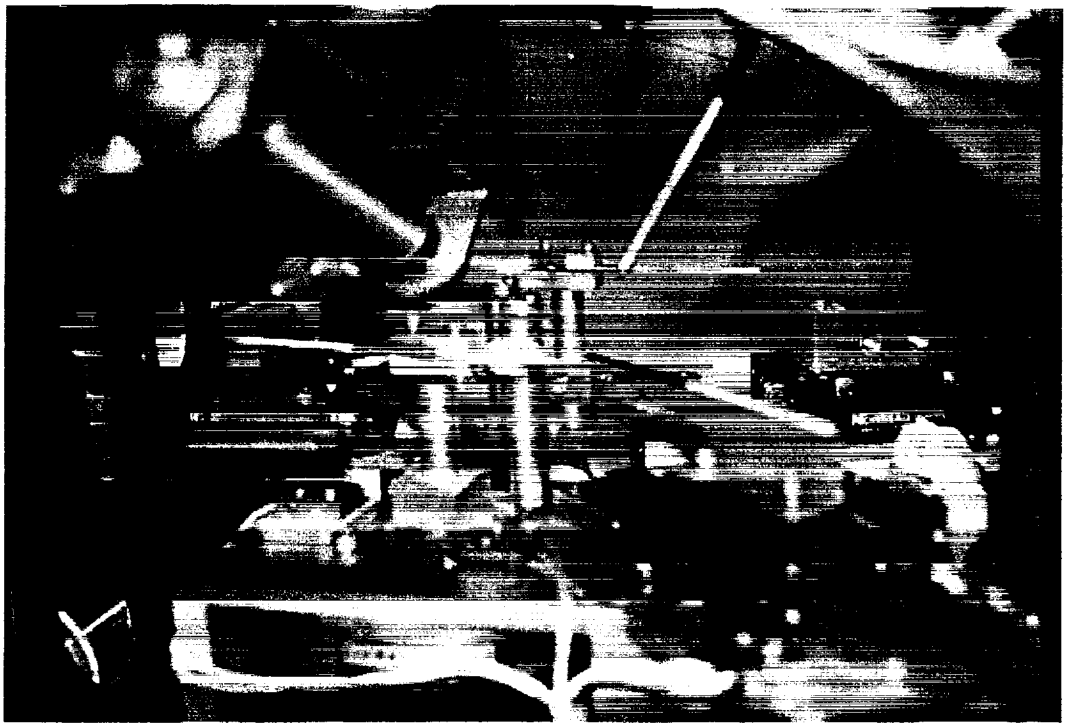

Figure 7 (1) Photographs of the experimental apparatus.

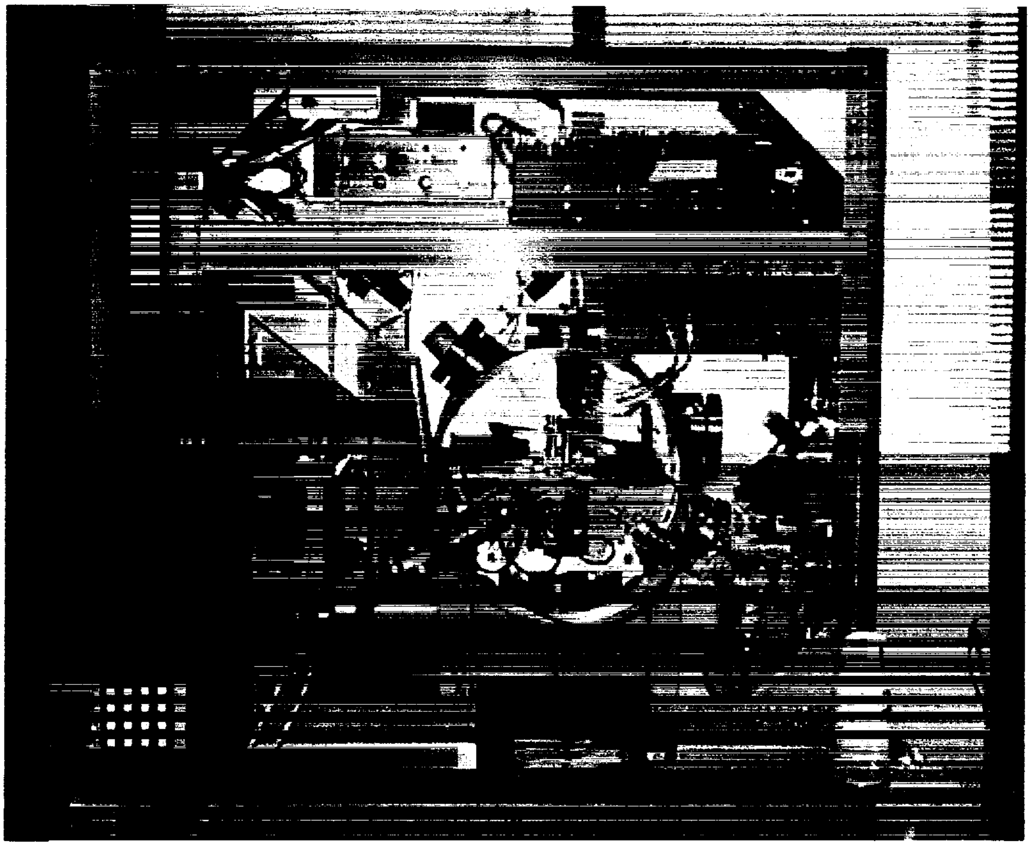

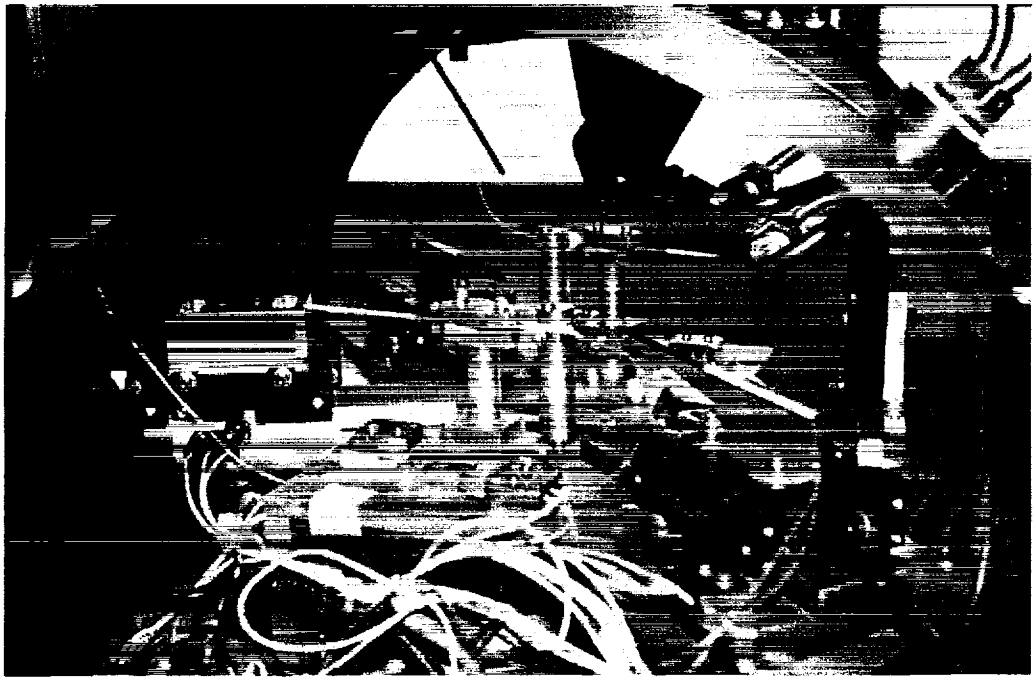

Figure 7 (2)　Photographs of the experimental apparatus.

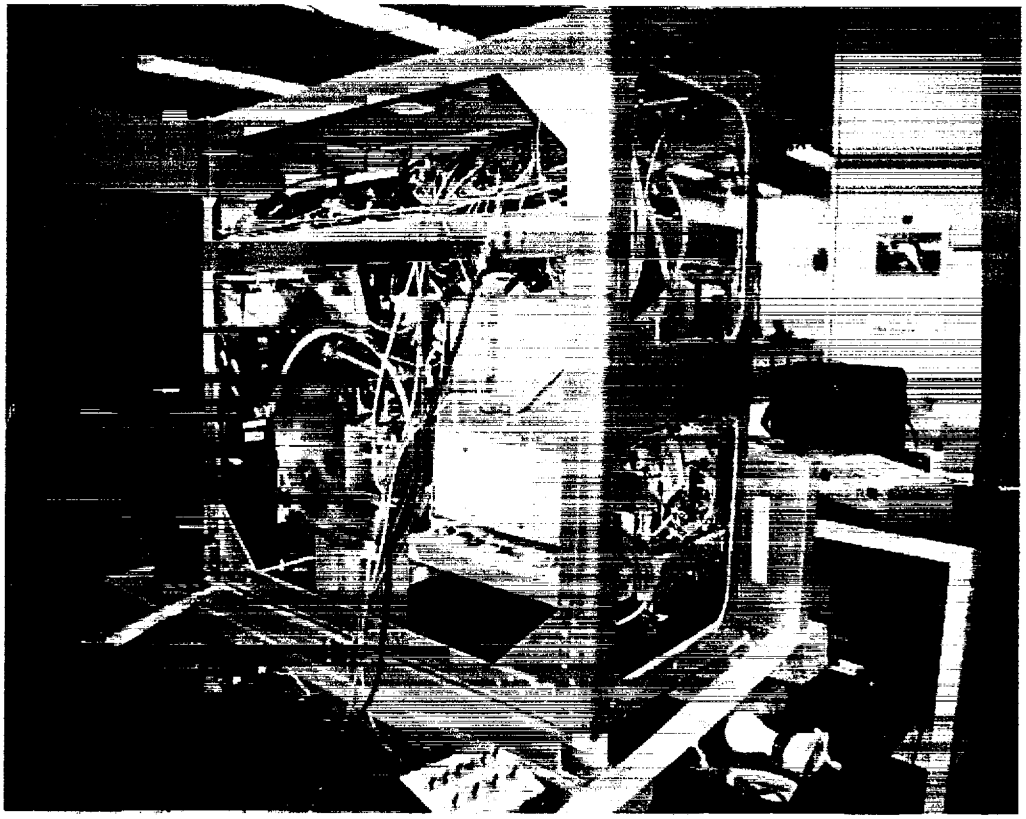

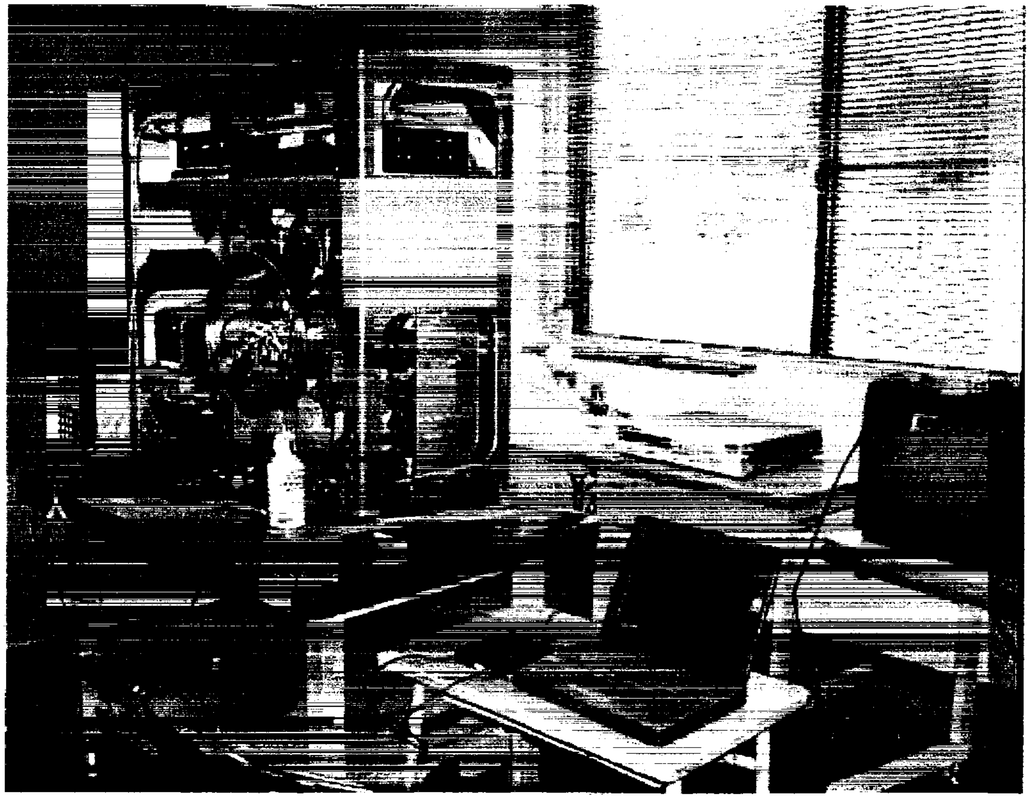

Figure 7 (3) Photographs of the experimental apparatus.

REPORT DOCUMENTATION PAGE

Form Approved
OMB No. 0704-0188

1. AGENCY USE ONLY *(Leave blank)*	**2. REPORT DATE** January 2000	**3. REPORT TYPE AND DATES COVERED** Technical Memorandum

4. TITLE AND SUBTITLE

Cooperative Research Projects in the Microgravity Combustion Science
Programs Sponsored by NASA and NEDO

5. FUNDING NUMBERS

WU-963-15-0B-00

6. AUTHOR(S)

Howard Ross, compiler

7. PERFORMING ORGANIZATION NAME(S) AND ADDRESS(ES)

National Aeronautics and Space Administration
John H. Glenn Research Center at Lewis Field
Cleveland, Ohio 44135-3191

8. PERFORMING ORGANIZATION REPORT NUMBER

E-11762

9. SPONSORING/MONITORING AGENCY NAME(S) AND ADDRESS(ES)

National Aeronautics and Space Administration
Washington, DC 20546-0001

10. SPONSORING/MONITORING AGENCY REPORT NUMBER

NASA TM—2000-209290

11. SUPPLEMENTARY NOTES

Responsible person, Howard Ross, compiler, organization code 6700, (216) 433-2562.

12a. DISTRIBUTION/AVAILABILITY STATEMENT

Unclassified - Unlimited
Subject Categories: 29 and 34 Distribution: Nonstandard

This publication is available from the NASA Center for AeroSpace Information, (301) 621-0390.

12b. DISTRIBUTION CODE

13. ABSTRACT ***(Maximum 200 words)***

This document contains the results of a collection of selected cooperative research projects between principal investigators in the microgravity combustion science programs, sponsored by NASA and NEDO. Cooperation involved the use of drop towers in Japan and the United States, and the sharing of subsequent research data and findings. The topical areas include (1) Interacting droplet arrays, (2) high pressure binary fuel sprays, (3) sooting droplet combustion, (4) flammability limits and dynamics of spherical, premixed gaseous flames and, (5) ignition and transition of flame spread across thin solid fuel samples. All of the investigators view this collaboration as a success. Novel flame behaviors were found and later published in archival journals. In some cases the experiments provided verification of the design and behavior in subsequent experiments performed on the Space Shuttle. In other cases, the experiments provided guidance to experiments that are expected to be performed on the International Space Station.

14. SUBJECT TERMS

Combustion; Microgravity; Flammability

15. NUMBER OF PAGES

211

16. PRICE CODE

A10

17. SECURITY CLASSIFICATION OF REPORT Unclassified	**18. SECURITY CLASSIFICATION OF THIS PAGE** Unclassified	**19. SECURITY CLASSIFICATION OF ABSTRACT** Unclassified	**20. LIMITATION OF ABSTRACT**

NSN 7540-01-280-5500

Standard Form 298 (Rev. 2-89)
Prescribed by ANSI Std. Z39-18
298-102